The use of a Radiotherapy Portal Imaging Device for Patient Setup Verification through Cone Beam Reconstruction

BY

FREDERIKA HENDRIKA JACOBA O'REILLY

Thesis submitted to comply with the requirements for the M.Med.Sc degree in the Faculty of Health Sciences, Medical Physics Department, at the University of the Free State.

May 2011

Promotor: Dr. F.C.P. du Plessis

Co-promotor: Prof. C.A. Willemse

Table of contents

Chapter 1

Introduction

1.1 Treatment of cancer

Cancer can be treated in a number of ways. Four standard treatment methods are surgery, chemotherapy, radiation therapy and immunotherapy. Surgery can be used for treatment, staging (determine how advanced the cancer is) and diagnosis of the disease.[14] Surgery can be performed alone or in conjunction with chemotherapy or radiation therapy. Radiotherapy (RT) is, after surgery, the most successful and most frequently used treatment modality for cancer. It is applied in more than 50% of all cancer patients.[42] Radiotherapy has developed over nearly eleven decades into an effective treatment modality which allows high-precision dose delivery.

1.2 High-precision radiotherapy

In RT a high radiation dose is delivered to the tumor volume in order to eradicate tumor cells. Unfortunately normal cells in the radiation path and radiosensitive organs close to the tumor volume are also affected and this can lead to irreparable tissue damage.[19] The objective of RT treatment is the delivery of the prescribed dose to the tumor volume while keeping the dose to normal cells and organs at risk (OARs) as low as possible.

The development of three dimensional (3D) conformal radiotherapy (CFRT) addressed this matter to a large extent. The basis of CFRT is to enhance tumor control by conforming the prescribed dose to the planning target volume (PTV), a volume that includes margins to account for treatment uncertainties. These uncertainties include the movement of organs during treatment delivery, varying shapes of different organs, set-up errors of the patient on the treatment couch

and the uncertainty in beam geometry being used. This technique allows high doses to be delivered the tumor while maintaining doses to normal tissues and OARs at acceptable levels.[19] To achieve this, more than one beam is normally used. The beams are shaped and tailored to fit (conform) the PTV.

To find an optimal beam configuration in cases where the target has a complex shape or the OAR is close to the PTV can be a difficult task and compromises have to be made. Treatment with conventional CFRT is thus limited to relatively simple planning geometries. The need for treatment techniques designed for more complex geometries lead the way for a specific CFRT technique called intensity modulated radiotherapy (IMRT).

With conventional CFRT the radiation fields are irregularly-shaped but of uniform intensity. With IMRT the radiation intensity across the irregularly-shaped fields is modulated by multileaf collimators (MLCs). The non-uniform intensity map, based on the dose prescription to the target volume and surrounding critical structures, is used to determine the optimal beam configuration and treatment parameters. This method is also known as 'inverse planning' as opposed to 'forward planning' used in conventional CFRT.[42]

With IMRT techniques steep dose gradients, such as 10% per mm, can be achieved quite easily.[20] This allows for dose escalation in the target volume and normal tissue avoidance. A 'new' method of delivering radiation with dose distributions similar to those created in IMRT is volumetric-modulated arc therapy (VMAT). Radiation is delivered while the gantry rotates in one or more arc around the patient. Several parameters such as MLC aperture shape, dose-rate, gantry rotation speed and MLC orientation can be varied during treatment delivery.[49] The advantages of this technique include highly conformal dose distributions and shorter treatment

times (entire treatment is completed with single rotation of the gantry). Shorter treatment times yield less discomfort for the patient which means a lower susceptibility to intra-fraction motion a contributor to overall treatment uncertainty.[47,49]

The use of treatment margins to account for treatment uncertainties such as target and normal tissue position at the time of treatment has placed a large constraint on the benefits of IMRT.[18] Imaging guidance of radiotherapy offers the possibility to accurately quantify and reduce these uncertainties to fully realize the potential of an IMRT treatment. The acquisition of patient images in the treatment room and the use of these images to reduce treatment uncertainties are called image guided radiotherapy (IGRT).[33]

1.3 Image-guided radiotherapy

IGRT is based on the matching/registration of two image data sets. The first being a reference set, usually images obtained during the planning stage of the treatment, and the second a set of images obtained in the treatment room just before the actual treatment. Most of the patients are planned using a 3D computed tomography (CT) dataset as a patient model. The most accurate matching would therefore be achieved if the image data set acquired in the treatment room is also in 3D. The acquisition of a 3D image data set in the treatment room can be accomplished by several imaging modalities such as: (I) In-room CT scanner systems,[30] (II) helical tomotherapy,[31] (III) kilo-voltage cone beam CT (kV CBCT),[37] and (IV) megavoltage cone beam CT (MV CBCT).[17,33]

1.3.1 In-room CT systems

The first in-room CT scanner system used a conventional CT scanner with a sliding couch top to align the CT images with the radiation treatment beams.[30] These systems were mainly used for frameless stereotactic treatments of the brain and lung, paraspinal lesions and prostate cancer treatments. A research group from the University of Yamanashi in Japan introduced a new common couch approach to these systems. Instead of using a sliding couch the treatment couch is kept fixed while the whole CT moves on horizontal rails parallel to the longitudinal axis of the treatment couch to perform the scanning. This system is called "CT-on-rails" or "self-moving gantry CT". The linear accelerator (linac) gantry and CT gantry are usually positioned at opposite ends of the treatment couch. 3D target localization can be done by rotating the couch through 180 degrees while the patient remains in an immobilized position. [30]

These systems have superior image quality due to the use of a conventional diagnostic CT scanner. Although the imaging capabilities ensure a great advantage special quality control procedures need to be implemented regarding the longitudinal movement of the gantry. Gantry movements can be accurate to within 0.5 mm and studies on an anthropomorphic Rando phantom (The Phantom Laboratory, Salem, NY) showed that the isocenter localization can be determined to within 2 mm.[16,30]

Introduction of these systems into an existing linear accelerator room will impact the room design and functionality. Although no additional shielding would be necessary, the floor and railing design, larger room and associated larger secondary barriers would increase the cost related to the installation of these systems.[16] Apart from the cost implications; excellent image quality, good geometric accuracy and availability of real-time patient geometric information

proves these systems to be of great use for image guided techniques such as patient set-up and target localization.

1.3.2 Helical tomotherapy

Helical Tomotherapy is a novel way for treatment verification, combining the features of a linear accelerator with those of a helical CT scanner. This system offers scanning technology incorporated into the treatment machine so that the patient need not move between CT scan image acquisition and treatment delivery. For both treatment and imaging modes, the couch moves into the gantry while the MV x-ray source and the detector rotate around the patient.

For systems using a MV x-ray source there will be a trade-off between dose delivered and image quality due to the physics of radiation interactions in the megavoltage energy range. The MVCT imaging on a helical tomotherapy unit is characterized in the literature and it was found that the uniformity and spatial resolution of MVCT images are comparable to that of diagnostic CT images. With respect to noise and low contrast these system do not have the same performance as conventional CT scanners, but this can be explained by the low doses (typically 1.1 cGy) that are delivered during the scanning procedure.[31]

Although the image quality obtained with these systems is inferior to that of conventional diagnostic CT scanners it still remains sufficient for patient localization as well as delineation of certain anatomical structures. These features together with the compact design of the device provide an innovative way for the delivery of image guided radiotherapy.

1.3.3 Kilovoltage cone-beam CT

Much research in IGRT has been focused on the development of linac-integrated imaging modalities. Kilo-voltage CBCT is an example of such a system. The general idea behind these systems is the detection of high energy photons with a flat panel imager attached to the linac. The source of photons is a kilovoltage x-ray source mounted on the gantry at 90 degrees from the megavoltage source opposite an onboard imaging device. The gantry is rotated around the patient to acquire a series of 2D portal images which are then used for the reconstruction of a 3D volume data set.[37]

With the necessary quality control and calibration procedures in place, the image quality obtained with these systems can be compared with those of conventional diagnostic CT scanners.[18] Due to the photons being in the kV energy range the system offers improved soft-tissue visualization which is a major advantage for image guidance procedures. Some factors that will influence the imaging performance of these systems include: (I) patient motion due to image acquisition times of typically 60 to 120 s, (II) misalignment of imaging-to-treatment isocenter, and (III) image artifacts such as ring artifacts and CBCT artifacts.[18,29]

RapidArc™, the Varian implementation of volumetric-modulated arc therapy, delivers image-guided, intensity modulated radiation therapy (IG-IMRT) by using a Varian accelerator equipped with an On-Board Imager® kV imaging system. Cone-beam CT images are used to guide patient positioning and treatment delivery. The treatment beam is shaped and reshaped as it is continuously delivered in an arc around the patient. Image guidance improves tumor targeting while IMRT conforms the dose distribution closely to the target. The tumor is therefore treated with pinpoint accuracy while normal tissue is spared.[47]

Except for additional hardware integrated onto the gantry these systems are minimally invasive, offering good geometric precision and superior image quality which are some of the basic requirements for an optimal image guidance modality.[29]

1.3.4 Megavoltage cone beam CT

Another approach to a linac-integrated imaging modality is MV CBCT where the treatment beam is used as the source and the electronic portal imaging device (EPID), attached to the treatment machine, as the detector. As in the case of kV CBCT the gantry is rotated around the patient while acquiring planar images at a series of gantry angles. These images are then used to reconstruct a 3D volume data set of the patient in the treatment position. Unlike Tomotherapy where one-dimensional ring detectors are used and one slice is reconstructed at a time, MV CBCT use 2D detectors (EPID) and reconstructs the entire volume simultaneously.

Using the treatment beam for imaging purposes is a departure from the conventional way of imaging with kV beams and will cause some challenges due to the basic physics of megavoltage photon interactions with matter. There will be a reduction in the visualization of soft-tissue structures due to the small energy dependence of the dominating Compton interaction for a large range of the MV energies. Despite this fact research has shown that the prostate, which is a large low-contrast object, can be visualized with approximately 9 monitor units (MUs).[33] A major advantage of MV imaging is the absence of ‘streak’ artifacts around high atomic number materials such as metal prostheses and tooth fillings.

Due to Compton scattering being linearly dependant on electron density alone, a higher number of photons or a higher dose, is necessary to obtain the same contrast compared to kV imaging.[33] This causes a trade-off between image quality and acceptable dose to the patient. It is shown in

the literature that acceptable image quality was obtained with 5 - 12 cGy depending on the size of volume being irradiated and level of contrast desired.[17] For localization based on bony structures lower doses such as 2 - 3 cGy were used, but doses in the range of 8 - 12 cGy were necessary for sufficient soft tissue contrast. These doses may seem small compared to the therapy doses received, but this extra dose can be taken into account during treatment planning of these patients.

Several factors contribute to making these systems an appealing alternative for image guidance in radiation therapy. These factors include, no additional hardware necessary due to use of the treatment beam, images are obtained in exact geometric coincidence with the treatment eliminating the need for cross calibration of the imaging-to-treatment isocenter geometry and satisfactory image quality with acceptable dose levels.

1.4 Aim of the study

The aim of this study is to evaluate an existing portal imaging device on an Elekta Precise linac for patient setup verification through megavoltage cone beam computed tomography. The objectives are to:

(I) Develop an optimal technique for acquisition of images with the IViewGT EPID for subsequent CBCT reconstruction i.e. number of gantry angles, (II) determine posing parameters of the imaging system for subsequent geometric calibration, (III) quantify the accuracy and precision of the method in terms of image quality and patient setup error determination, and (IV) determine the imparted dose to the patient.

Chapter 2

Theory

2.1 Portal imaging

2.1.1 Development of portal imaging

Images taken at the time of treatment using the therapeutic beam as a source are referred to as portal imaging. Traditionally radiographic film was used as imaging medium to verify treatment delivery. Various reasons such as processing time, fixed dynamic range and the need to first digitize films in order to enhance or manipulate images makes film impractical for on-line imaging.[27] The limitations of film served as a motivation for the development of an imaging medium that offers real-time digital read-out.

The first EPIDs were camera based systems using a metal plate (1-2 mm copper, steel or brass thickness) and phosphor (usually gadolinium oxysulphide) for x-ray conversion. X-rays hitting the metal plate produce high energy electrons of which some of the energy is converted into light by the phosphor. The light is reflected off a series of mirrors into a lens and camera which converts the image into a video signal that is processed and displayed on a computer screen. The system offers fast high resolution imaging and the maintenance and service is relatively economical. Only a small portion (10-20%) of the light is captured by the camera and the lens. The above mentioned together with electronic noise in the camera chain limits the efficiency of these systems.[27]

In the 1980s the Netherlands Cancer Institute (NKI) designed the liquid ionization chamber matrix EPID. The device consists of two electrodes separated by a gap (± 1 mm) filled with an

organic fluid (iso-octane or trimethylpentane) which acts as the ionization medium during exposure. Each electrode forms part of a 256 x 256 matrix. The electrodes are spaced 1.27 mm from each other yielding a 32.5 cm x 32.5 cm detector area. A stainless steel plate (1 mm thick) placed on the front surface acts as build-up and converts the incident x-rays to high energy electrons that ionize the liquid. The electrodes are individually connected to a high voltage supply and collect the ions to readout the image row upon row.[27,28] The system has a compact and practical design which makes it easy to use. The main disadvantages of these systems are the sensitivity of the electronics surrounding the detection area and the small fraction (1.5%) of incident x-rays that are used for image formation.[27]

At present most of the commercially available EPIDs work on the basis of an active matrix flat panel imager. Although there are various designs, the most widely used is a metal sheet (usually 1 mm copper) and a gadolinium oxysulphide phosphor screen combination to convert x-rays to light. A two-dimensional array of hydrogenated amorphous silicon diodes (a-Si:H) (see Figure 2.1), controlled by a-Si:H thin film transistors (TFT), detects the light. Each photodiode represents a pixel in the image and are electronically read. The pulsing of the linac output may cause image artifacts; readout is therefore done between pulses. Although image acquisition can be fast data transmission and image display processing may take 3-4 s which slows down the image display rate.[28] Due to close contact between the phosphor and the photodiodes light collection is optimal offering good image quality. Conversion of light photons and readout of signals are highly efficient.[27,28] The a-Si flat panel imager used in this study was the iViewGT from Elekta.

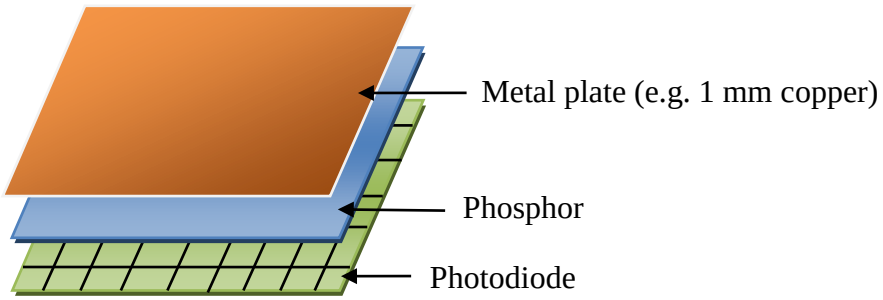

Figure 2.1: Illustration of an a-Si:H flat panel imaging device. The device consists of a front metal plate (usually 1mm copper) layered onto a phosphor to convert x-rays to light. The light is detected by an array of a-Si:H photodiodes which is controlled by a-Si:H thin film transistors. The photodiodes are electronically read and form the pixels of the image.

2.1.2 Characteristics of the modern iViewGT

The device is mounted on the gantry of the linear accelerator (linac) and is fully retractable when not in use. Image acquisition is controlled by a remote computer processing unit. Single, double or movie exposures can be taken during a procedure/treatment. iViewGT requires typically two to four monitor units (MUs) for a 16-bit portal image. To ensure consistent and repeatable image quality the EPID waits for the linac to reach optimum dose rate before triggering image capture. Algorithms automatically process the raw data before it is displayed on the monitor. Manual manipulation of images can thereafter be done and the final images can then be stored on the system.[12] Important technical specifications concerning this study are summarized in Table 2.1.

Table 2.1: Technical specifications of the iViewGT a-Si detector.[12]

iViewGT detector specifications	
Retractable system	Fixed SSD, 60cm from isocenter
Isocentric stability	2 mm at isocenter
Panel dimensions	length x width: 410 mm x 410 mm
Field of view	Image size referred to isocenter:
	26cm x 26cm (head at 0°)
Image resolution	1024 x 1024
	16 bit grey scale
	Pixel size at isocenter: 0.25 mm
	Pixel size at detector: 0.4 mm
Image acquisition rate	3 frames per second
Spatial resolution	Isocenter – measured limiting resolution 0.9 lp/mm
	Detector – measures limiting resolution 1.31 lp/mm

2.1.3 Clinical use of an electronic portal imaging device

EPIDs are primarily used for verification of treatment delivery and more specifically the quantification and correction of set-up errors. Correction of set-up errors yields improved treatment accuracy and evaluation of these errors are used to quantify margins necessary to account for uncertainties in treatment delivery.[28]

Portal images have intrinsically poor subject contrast due to the attenuation characteristics of megavoltage beams used for image acquisition. Bony landmarks or implanted fiducial markers

have to be used as surrogates for visualization of soft tissue volumes. To overcome this weakness some linacs are equipped with a kilovoltage tube and an additional detector [37] to yield diagnostic quality images and others are modified to produce beams in the kilovoltage range.[33]

In some centres EPIDs are used to acquire patient dose information. EPIDs can therefore yield both geometrical and dosimetric information and thus provide a powerful verification tool for advanced techniques such as conformal and intensity modulated radiotherapy.[28]

2.2 Computed tomography

2.2.1 General principles of computed tomography (CT)

The basic principle of CT is the reconstruction of an object from its intensity profiles or projections acquired over a set of angles. X-rays traverse the object and are attenuated to various extents depending on their path through the object. A profile with varying intensities is then measured with the detector array. To reconstruct the spatial distribution of a three-dimensional object, projections from various angles around the object need to be acquired.[7]

The acquisition of data depends on the geometry of the scanner and detector. Parallel projections are taken by measuring a set of parallel rays for a number of different angles. This is known as parallel-beam reconstruction and could be measured, for example, by moving a x-ray source and detector along parallel lines on opposite sides of the object. In fan-beam reconstruction, a x-ray point source emanates a fan-shaped beam that penetrates an object and is measured with a one-dimensional (1D) detector array. The source and the detector array are rotated about the object to collect sufficient fan-beam projections. When a x-ray point source and a 2D detector array are used, cone-beam reconstruction is required. By using a cone-beam, data collection time can be reduced because ray integrals are measured through every point in the object in the same time it

takes a single slice in a 1D detector array scanner.[24] In this study cone beam data is reconstructed from a megavoltage x-ray source and the EPID forms the 2D detector.

2.2.2 Reconstruction Algorithms

Reconstruction methods used to construct single and multiple (3D volume) images can generally be separated into two main groups. Direct methods which are based on (I) the Fourier slice theorem and, (II) iterative methods that try to solve the reconstruction problem by solving a system of simultaneous equations. The Filtered Backprojection (FBP) algorithm is the most prominent member of the former group. This algorithm uses the ramp filter in frequency space to do filtering on the projection images. The filtered images are then backprojected onto a reconstruction grid. The Algebraic Reconstruction Technique (ART) is the first and most established algorithm used in iterative methods. This method uses a reconstruction grid which is iteratively updated by a projection-backprojection procedure until a convergence criterion is satisfied.[35]

The basic idea of backprojection is as the name implies; projections are smeared back onto a reconstruction grid. The projections will interact constructively in areas corresponding to the position of the object and generate a rough approximation to the original object. A problem that arises in this process is the blurring of images due to the smearing of projections onto the grid. This problem is solved by filtering the projections before it is back projected. The combination of back projection and filtering is known as Filtered Backprojection.

Different filters or combinations of filters can be used (Figure 2.2). A high-pass filter (e.g. ramp filter) is used to eliminate blurring effects. These filters will unfortunately also lead to amplification of high-frequency noise. To reduce noise a low-pass filter (e.g. low pass cosine,

Hamming or Shepp-Logan) can be applied in succession. These filters will smooth the image so that there are no sharp edges but will cause a decrease in resolution. Thus, there is a trade-off between a good high-pass filter to obtain sharp images and a low-pass filter to suppress noise.

Window functions can also be used to reduce noise. These are mathematical functions that are used in filter design to create a 'zero-value' outside a defined interval. When another function is multiplied by the window function, the product will also be 'zero-valued' outside the interval and all that is left is the area where they overlap. Redundant data, representing noise, will therefore not be backprojected. No window function was defined in this study.

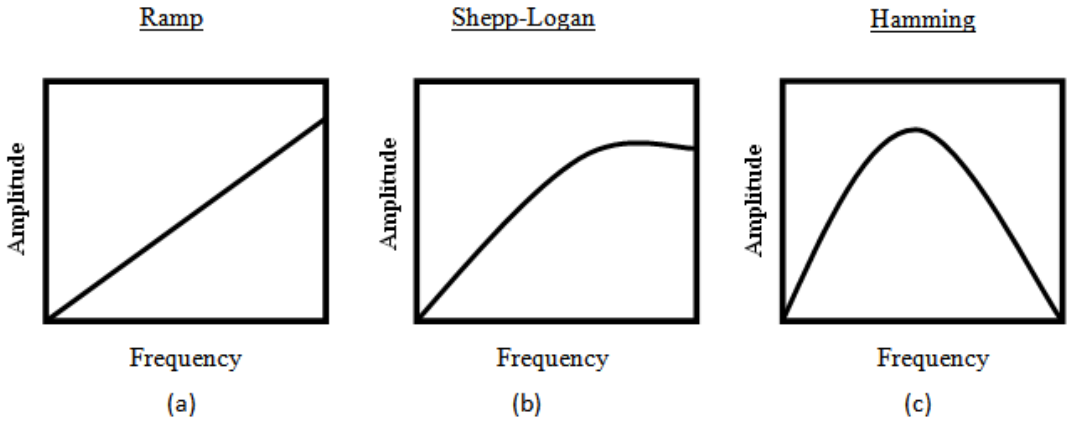

Figure 2.2: Three CT reconstruction filters in the frequency domain. The ramp filter (a) is a high-pass filter and ideal for noise free images. Noise is unavoidable in x-ray imaging. The ramp filter will therefore cause amplification of high frequency noise. The Shepp-Logan filter (b) will cut off some of the high frequencies and offers a good compromise between noise reduction and resolution. The Hamming filter (c) will cut off almost all high- frequencies and will result in images with little detail and no sharp edges.

Filtering mathematically reduces blurring and yields accurate representations of original object geometries. Filtering is done by convolving the raw projection data with a convolution kernel. The kernel refers to the shape of the filter function in the spatial domain (projection space). A

common practice is to perform filtering in the frequency domain. This involves Fourier transformation (FT) of the data from the spatial domain to the frequency domain; filtering by multiplying the FT data with the frequency domain kernel and then by performing an inverse FT of the product, the filtered data is ready to be back projected onto the reconstruction grid.[6]

The filtered data, $p'(x)$, can be calculated by the following equation:

$$p'(x) = FT^{-1}\{FT[p(x)] \times K(f)\} \quad (2.1)$$

where $p(x)$ is the raw projection data, $K(f) = FT[k(x)]$ is the kernel in the frequency domain. Filtering in the spatial domain is represented by:

$$p'(x) = p(x) \otimes k(x) \quad (2.2)$$

where convolution, an integral calculus operation, is indicated by $\otimes$.

With the iterative reconstruction technique an assumption of the 3D spatial distribution of the object is made. Projections are calculated from the assumed distribution and compared with the actual projections. The calculated projections are adjusted to correspond with the actual projections. This process is repeated a few times until the calculated and actual projections are the same or within preset limits.[11] This technique is more amenable in situations where it is not possible to measure a large number of projections or when projections are not uniformly distributed over 180 or 360°, both these conditions being necessary requirements for transformed based techniques (e.g. FBP) to achieve results with accuracy desired in medical imaging. Iterative methods are computationally less efficient than the FBP algorithm. However, with fast computer speed and small imaging matrices this method can be feasible for some cases.

The Feldkamp-type (FDK) algorithm is most widely used for cone-beam image reconstruction. The algorithm uses an approximation of the FBP process through a weighting factor. The weighting factor compensates for the longer paths the photons have to travel at larger cone angles (width of beam in longitudinal direction). Advantages of this algorithm include its simplicity, computational effectiveness and the ability to handle truncated data.[39]

Figure 2.3: Key parts of the FDK algorithm. Projections are weighted to compensate for longer paths photons will travel at larger cone angles. Filtering is done in the frequency domain by multiplication of the filter function and the weighted projection. The filtered projections are backprojected onto a 3D reconstruction grid to yield the scanned object.

2.2.3 Three dimensional reconstruction

The reconstruction algorithm used in this work is a filtered backprojection based on analyses from the literature.[24] The approach taken for the 3D reconstruction is to use a generalization of the 2D fan beam algorithm.[15,24] The reconstructions for both fan- and cone-beam types are based on finding the corresponding parallel projections of measured data, but instead of simple backprojection of parallel beam tomography the backprojection becomes a weighted backprojection (see subsequent discussion).

The basis of the 3D reconstruction is the filtering and backprojection of a single plane within the cone. Think of a cone-beam consisting of several fan beams tilted from the midplane. In other

words each tilted fan beam is considered separately and at the end the contribution from all the tilted fans are summed to yield the reconstructed object.

Cone beam projection data, $R_\beta(x, y)$, are a function of the source angle, β, and the horizontal and vertical positions, x and y, on the detector plane.

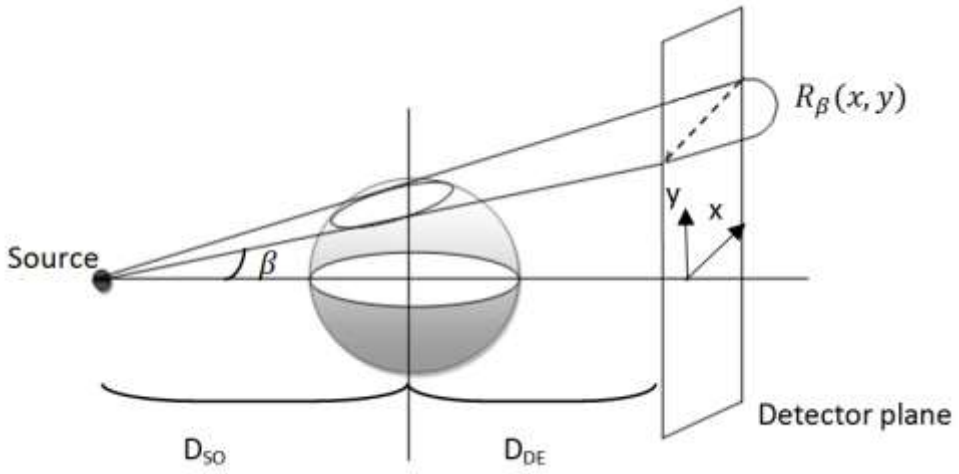

Figure 2.4: In cone beam CT all the data necessary for 3D reconstruction is obtained by rotating the source and detector plane around the object. The projection data is a measurement of the x-ray flux over a plane and a function of source angle β and the (x, y) position on the detector plane.[24] D_{SO} is the distance from the center of rotation to the source and D_{DE} is the distance from the center of rotation to the detector.

To describe a ray in a 3D projection a new coordinate system (t, s, r) has to be introduced. This is obtained by two rotations of the (x, y, z) axis. The first rotation is by θ degrees around the z-axis to give the (t, s, z)axes. The second rotation is done out of the (t, s) plane around the t-axis by an angle of γ.

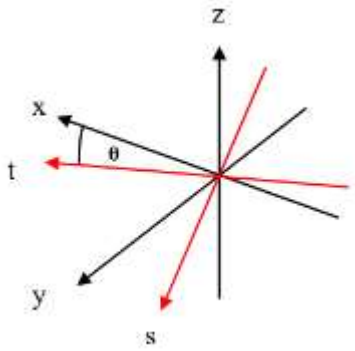

Figure 2.5: A new coordinate system is introduced to simplify the discussion of cone-beam reconstruction. The source rotates around the z-axis with angle θ to yield the new rotated (t, s, r) coordinate system. The r-axis is not shown but is perpendicular to the t- and s-axes.[24]

A three dimensional parallel projection of the object, *f*, is given by:

$$P_{\theta,\gamma}(t,r) = \int_{-S_m}^{S_m} f(t,s,r)ds \qquad (2.3)$$

Four variables are used to specify a particular ray in the cone beam: (t, θ) specify the distance and angle in the x-y plane and (r, γ)in the s-z plane. As mentioned earlier the source is rotated by β and the ray integrals (integral of measured data along specified line) are measured on a detector plane by $R_\beta(p', \zeta')$.

To find the equivalent parallel projection ray we first define, p and ζ:

$$p = \frac{p' D_{SO}}{D_{SO}+D_{DE}} \qquad \zeta = \frac{\zeta' D_{SO}}{D_{SO}+D_{DE}} \qquad (2.4)$$

where D_{SO} is the distance from the center of rotation to the source and D_{DE} is the distance from the center of rotation to the detector (Figure 2.4).

The parallel projection ray for a given cone beam ray, $R_\beta(p, \zeta)$, is given by:

$$t = p\frac{D_{SO}}{\sqrt{D_{SO}^2+p^2}} \quad , \quad \theta = \beta + tan^{-1}(p/D_{SO}) \qquad (2.5)$$

where t and θ locate a ray in a given tilted fan, and similarly

$$r = \zeta \frac{D_{SO}}{\sqrt{D_{SO}^2+\zeta^2}} \quad , \quad \gamma = tan^{-1}(\zeta/D_{SO}) \tag{2.6}$$

where r and γ specify the location of the tilted fan itself.

The cone beam reconstruction algorithm can be broken into three steps.[24] Firstly the projection data, $R_\beta(p,\zeta)$, is multiplied by the weighting function, $\frac{D_{SO}}{\sqrt{D_{SO}^2+\zeta^2+p^2}}$ to obtain the weighted projection:

$$R'_\beta(p,\zeta) = \frac{D_{SO}}{\sqrt{D_{SO}^2+\zeta^2+p^2}} R_\beta(p,\zeta) \tag{2.7}$$

Secondly the weighted projection is filtered either by multiplication in the frequency domain or convolution in the spatial domain. The filtered projection, $Q_\beta(p,\zeta)$, is thus given by:

$$Q_\beta(p,\zeta) = R'_\beta(p,\zeta) \times h(p) \tag{2.8}$$

where $h(p)$ is the filter function in the frequency domain. The third and final step is to backproject each filtered projection onto a 3D reconstruction grid.

$$g(t,s,z) = \int_0^{2\pi} \frac{D_{SO}^2}{(D_{SO}-s)^2} Q_\beta(p,\zeta) d\beta \tag{2.9}$$

2.2.4 Megavoltage cone-beam computed tomography (MV CBCT)

In order to acquire a large volume scan using a fan beam as in a single slice CT system, the treatment couch or imaging system needs to be moved in the longitudinal direction while the beam is rotated around the patient. This is due to the fact that a fan beam will only cover a slice across the patient. With a cone-beam scan (wider in the longitudinal direction) the possibility to

acquire a whole volume scan in a single rotation becomes possible. Considering the practical and mechanical implications of a linac based system, it would be unfeasible to use a fan beam system. Cone beam imaging is therefore required.[39]

With advanced technology making EPIDs more efficient in detecting MV photons the use of an EPID for cone-beam imaging has become evident. By using a linac as source and EPID (2D detector array) as detector we have a workable cone beam system in the treatment room. The cone beam images can be used to reconstruct a volume data set of the patient just before treatment delivery. This contributes to more accurate patient set up and improved treatment outcome.

2.3 Geometric calibration of cone-beam systems

The geometrical calibration of a cone-beam computed tomography (CBCT) system is an essential step to ensure accurate reconstruction of images. The calibration process involves the estimation of a set of posing parameters (parameters describing the system pose at each projection angle) that fully describes the geometry of the CBCT system. These posing parameters include source and detector position, detector tilt and rotation, piercing point and gantry angle. Inaccurate estimation of these parameters can result in severe artefacts.[25,36,44] Even small errors can have visibly detrimental effects on the reconstructed image eg. double contours and flattened images.

Throughout the literature [10,25,36] different techniques have been investigated to perform geometric calibration of a misaligned scanner system. It varies from imaging a single object or point source at two projection angles or multiple objects at known positions for a set of projections. All these methods have some characteristics in common and can be summarized in three steps: (a)

assumptions are made that some conditions are ideal or negligible; (b) projections are acquired at multi-angles and, (c) a set of equations containing the parameters are solved.

A method proposed in the literature was used in this study.[10] A cylindrical calibration phantom consisting of two rings of ball bearings (BBs) equally spaced and equidistant from the center of the phantom was used (Figure 2.6). The two circular patterns of BBs form two elliptical shaped projections on the detector plane. By fitting mathematical ellipses through the projection data a complete and thorough description of the position and rotation of the source and detector can be derived.

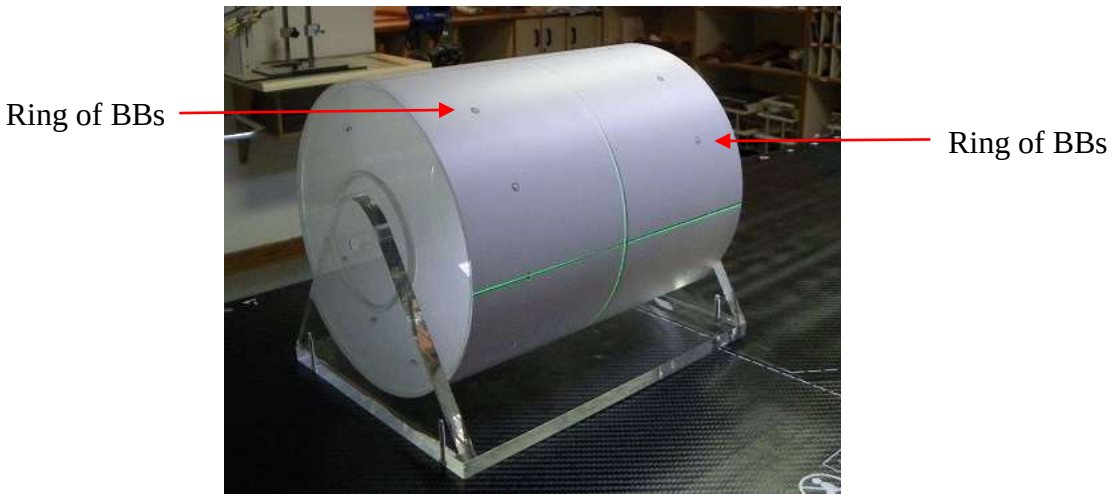

Figure 2.6: A dedicated phantom manufactured for geometric calibration of the imaging system. The phantom consists of a perspex cylinder containing two circular patterns of BBs equidistant from the center of the phantom.

2.3.1 System geometry

To describe the geometry of the system three right-handed Cartesian coordinate systems are used. The world (*w*), virtual detector (*v*) and real detector (*r*) coordinate systems. The real imaging object (phantom or patient) and CT reconstruction is based in the world coordinate

system and is fixed in space for a linac with rotating gantry. The z axis is along the rotation axis of the gantry for the linear accelerator (linac). The x axis is pointing towards the source at a gantry angle of zero and is perpendicular to z. The y axis is pointing to the source at a gantry angle of ninety degrees (Figure 2.7).

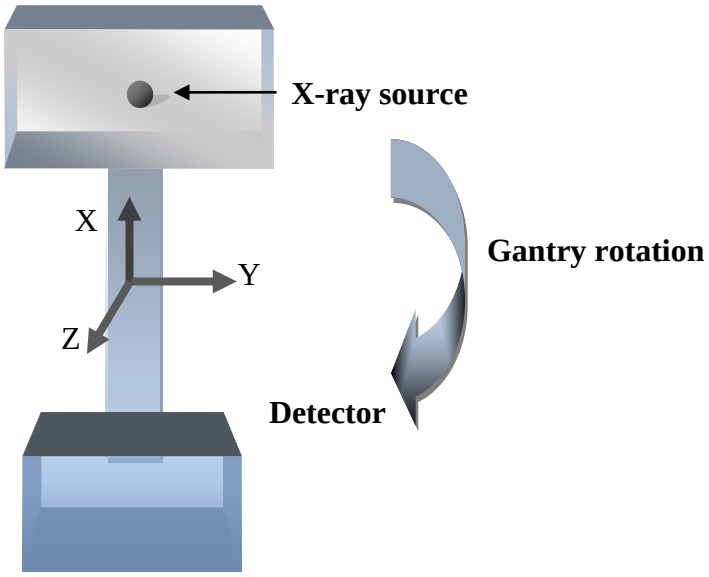

Figure 2.7: Illustrated here is the world coordinate system (*w*) fixed in space for a linac with a rotating gantry. The z axis is along the rotational axis of the gantry. The x axis is pointing towards the x-ray source at a gantry angle of zero. The y axis forms a vector which is the cross-product of vectors x and z.

To describe the geometry of a perfectly aligned detector the virtual detector coordinate system (*v*) is introduced. The projection point of the world coordinate system on the detector plane indicates the origin of the virtual detector system as shown in Figure 2.8. This point is also referred to as the piercing point. The z-axis is the normal of the detector and coincident with the line connecting the source and piercing point. The y-axis is anti-parallel to the z-axis of the world coordinate system ($y^v = -z^w$) and the x-axis is perpendicular to the vector from the piercing point to the source (Figure 2.8).

The detector can tilt around the central detector row by an angle of θ degrees and around the central detector column by an angle of ϕ degrees. Rotation around the central ray (z-axis of virtual detector) is indicated by η degrees. The real detector coordinate system (R) is therefore introduced to model possible tilting (ϕ, θ) and rotation (η) of the detector from the virtual detector plane (see Figures 2.10 and 2.12).

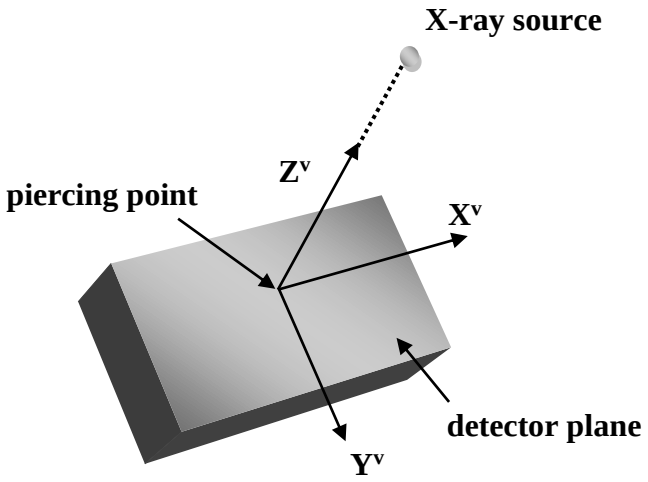

Figure 2.8: The coordinate systems of a perfectly aligned (virtual) detector. The real detector coordinate system is introduced to represent possible tilting or rotation of the virtual detector.

Once the coordinate systems are defined, objects in one coordinate system can be referenced to another. The following equations can be used for transformation of a position vector (P^w) in the world coordinate system to one (P^v) in the virtual detector coordinate system.[10] Basically each point (P) in (w) can be translated (T) and rotated (R) to its location in (v).

$$P^v = R_w^v P^w + T_w^v \qquad (2.10)$$

where

$$P^w = [X^w \;\; Y^w \;\; Z^w] \tag{2.11}$$

The rotation matrix R_w^v and translation vector T_w^v can be written as follows:

$$R_w^v = \begin{bmatrix} St & Ct & 0 \\ 0 & 0 & -1 \\ -Ct & St & 0 \end{bmatrix} \tag{2.12}$$

and

$$T_w^v = [X_d \quad Y_d \quad Z_d] \tag{2.13}$$

where St and Ct are sine and cosine of the nominal gantry angle t. The position vector from the origin of the virtual detector system to the origin of the world system is represented by the translation vector. The subscript *d* indicates the position of the detector.[10]

Rotation and tilting information are considered by the rotation matrix R_v^r from the virtual detector (v) system to the real detector (r) system as shown by the following equation:[10]

$$P^r = R_v^r P^v \tag{2.14}$$

where $P^r = [X^r Y^r Z^r]^T$ and $P^v = [X^v Y^v Z^v]^T$ are position vectors in the real detector and virtual detector systems, respectively.

R_v^r can be written as follows using the detector tilt (ϕ and θ) and rotation (η) angles:[10]

$$R_v^r = \begin{bmatrix} C\emptyset C\eta - S\theta S\phi S\eta & C\theta S\eta & -S\phi C\eta - S\theta C\phi S\eta \\ -C\phi S\eta - S\theta S\phi C\eta & C\theta C\eta & S\phi S\eta - S\theta C\phi C\eta \\ C\theta S\phi & S\theta & C\theta C\phi \end{bmatrix} \tag{2.15}$$

2.3.2 Calculation of ellipse parameters

The projection of BBs arranged in a circular pattern will yield an ellipse on the projected plane.[36] To fit and describe each of these two ellipses a method from the literature was used.[10,36]

$$a(u-u_0)^2 + b(v-v_0)^2 + 2c(u-u_0)(v-v_0) = 1 \qquad (2.16)$$

where (u_0, v_0) is the center of the ellipse. The parameters a, b, c, u_0 and v_0 can be found using a linear least-square method from projection points (u, v) of the BBs. The detector angle tilt (ϕ), can now be calculated by using the calculated ellipse parameters and the following equations:[10,36]

$$\sin \emptyset = \frac{-c_1\zeta_1}{(2a_1)} - \frac{c_2\zeta_2}{(2a_2)}, \qquad (2.17)$$

$$\zeta_k = Z_s^r a_k \sqrt{a_k} \Big/ \sqrt{a_k b_k + a_k^2 b_k (z_s^r)^2 - c_k^2}\ , \quad k = 1,2 \qquad (2.18)$$

where Z_s^r is the Z axis component of the source position in the real detector coordinate system and ζ_k is the intermediate parameter used in ellipse parameter calculation. The subscript k indicates one of two sets of BBs, each configured at equal intervals around the perimeter and equidistant from the center of the cylindrical phantom.

The ellipse parameters and the positions of the projected BBs are used to estimate the geometric parameters of the cone-beam imaging system. The parameters used to characterize the system are: (I) piercing point (projection of the origin of the world coordinate system on the detector), (II) detector rotation angle, η, (III) detector tilt angles, theta (θ) and phi (ϕ).

2.3.3 Piercing point

If the megavoltage CBCT system were to follow a perfectly circular trajectory during rotation of the gantry the piercing point which is the projection of the origin of the world coordinate system would be a fixed point at the center of the detector. In practice the piercing point will vary with gantry angle due to mechanical flexing of gantry components during rotation of the system. This drifting of the piercing point is responsible for double contours in reconstructed images.[25] In order to produce accurate and high quality reconstructed images it is therefore necessary to compensate for the variations in the piercing point location from projection to projection.

2.3.4 The concept of a converging point

To determine the detector rotation (η) and tilt angles (θ, ϕ) the concept of a converging point is introduced to simplify the rather complex geometry. One source and two point objects (BB1 and BB2) define a plane, called a divergent plane (see Figure 2.9). The intersection of the divergent plane and the detector plane is the line that connects the projected BB locations. Another pair of BBs forms another divergent plane in the same way. The converging point P_c, which is due to the detector tilt angle, is the point where all these lines (L_i) intersect.[10]

If all the lines connecting projected pairs of point objects are in one plane, the intersection of the divergent planes (D1, D2) forms one line. This line is the axis of the divergent planes. The divergent planes and the axis of the divergent planes are analogous to sheets of paper and the spine of a book. [10]

The converging point always exists on the (extended) detector plane, except in the case where the axis of the divergent planes is parallel to the detector plane (perfectly aligned (virtual)

detector). With the cylindrical phantom we have more than two pairs of objects and the lines connecting a pair of objects in the space are parallel. The converging point can therefore be found by determining the intersection of the axis of the divergent plane and the detector plane.[10]

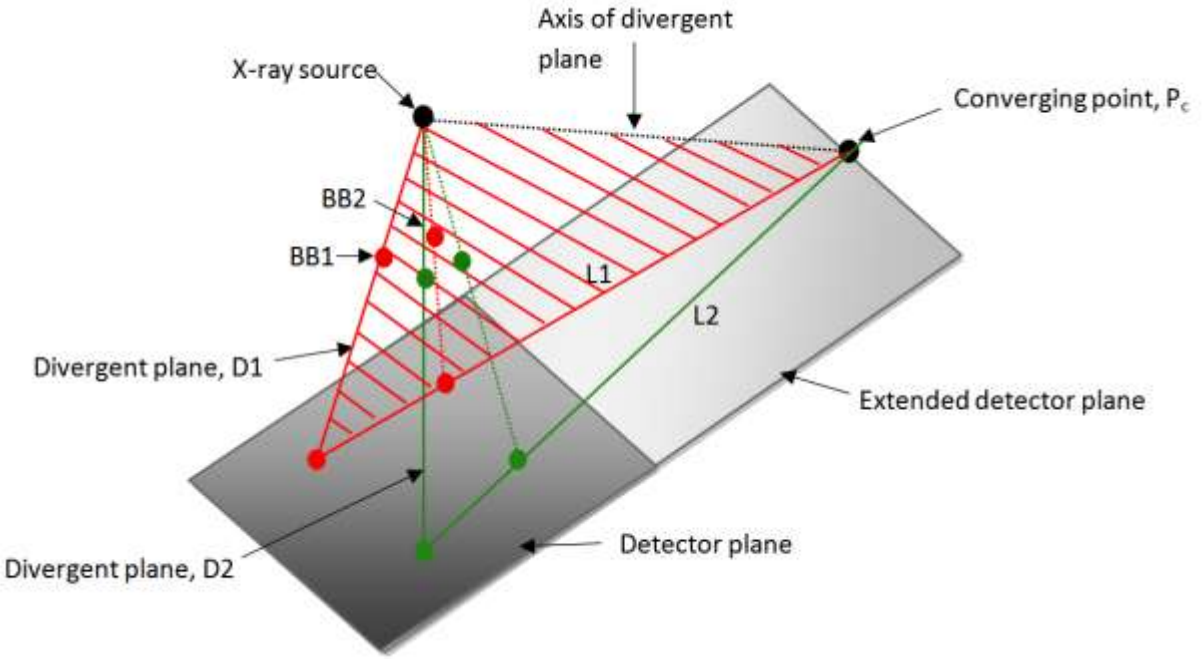

Figure 2.9: A source and two point objects (BB1 and BB2) define a plane, called a divergent plane. The intersection of the divergent plane and detector plane forms a line (L_i) connecting the projected BBs. The intersection of all these lines (L_i) is indicated by the converging point (P_c). The converging point will always exist on the extended detector plane, except in the special case when the axis of the divergent planes is parallel to the detector plane.

2.3.5 Detector rotation angle, η

The rotation of the detector around its normal axis is referred to as the detector rotation angle (η) or skew. This parameter has the most severe impact on image quality. Due to the nature of the reconstruction algorithm where projection pixels are independently weighted and then filtered, rotation of the detector would yield incorrect filtering and the use of skewed detector rows

instead of rows perpendicular to the axis of rotation.[25] This will cause cross talk between slices and the backprojected image would be blurred and flattened.[44]

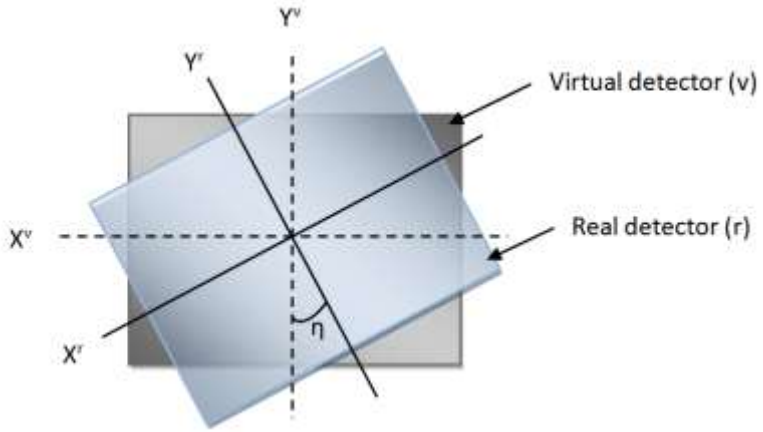

Figure 2.10: The angle η specifies the rotation of the detector around its normal axis, Z^r.

To determine the detector rotation angle two points on the extreme X^v dimensions of the two fitted ellipses on the projected image is chosen. These two points must be determined with a numerical model and not by the position of the set number of the BBs.[10] Lines connecting these two extreme points are generated and indicated by L_1 and L_2 in Figure 2.11. When the detector is tilted by ϕ around its Y^v axis these two lines will converge to one point, $P_{\emptyset}$.

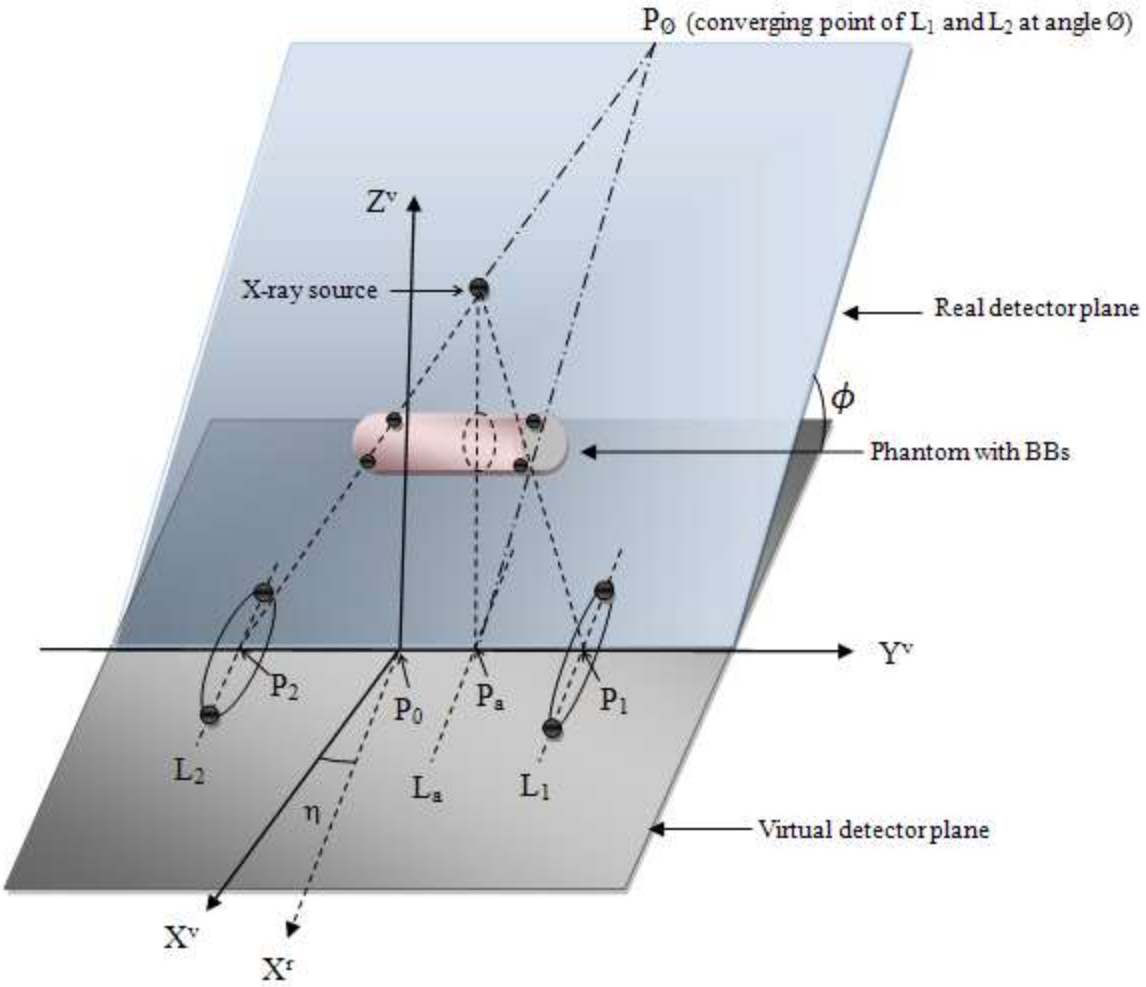

Figure 2.11: The shape of ellipses around points P_1 and P_2 and converging point, $P_{\emptyset}$, due to detector tilt angle, ϕ, is illustrated. The projection of BBs coinciding with the central ray of the beam (shown as broken circle) will generate a line, L_a, passing through point P_a on the detector plane. Line L_a is parallel to the lines L_1 and L_2 when ϕ is zero (virtual detector plane) and to the X^r axis when ϕ is nonzero (real detector plane). Therefore, the angle between line L_a and the X^v axis will be the same as detector rotation, η.

If there were BBs in the phantom coinciding with the central ray the projected image would be a line, L_a, passing through point P_a on the virtual detector plane. This line will be parallel to line L_1 and L_2 if there were no tilt around the Y^v axis. If however there is a tilt around the Y^v axis, line L_a will pass through point $P_{\emptyset}$ and be parallel to the X^r axis.

The ratio of the short axis (a_k) to long axis (b_k) of the ellipse, $\sqrt{a_k/b_k}$ $(k = 1,2)$, is proportional to the distance from point P_a to the center of each ellipse P_1 and P_2. Point P_a can therefore be found by using the following equation:[10]

$$\frac{(P_0^a - P_0^2)}{(P_0^1 - P_0^a)} = \frac{\sqrt{a_2/b_2}}{\sqrt{a_1/b_1}}, \quad \text{or}$$

$$P_0^a = \frac{\left(P_0^1\sqrt{a_2/b_2} + P_0^2\sqrt{a_1/b_1}\right)}{\left(\sqrt{a_1/b_1} + \sqrt{a_2/b_2}\right)} \tag{2.19}$$

where P_m^n is a position vector from point m to point n.

The distance from point P_a to the center of each ellipse is proportional to the angles of lines L_1 and L_2 with respect to the line L_a. The angle between line L_a and X^v, or X^r (α) and X^v is the detector angle, η, since L_a is parallel to X^r when the detector tilt angle, ϕ, is nonzero. When the detector rotation angle is not zero, the angles of the lines in the real detector coordinate system are different by the detector rotation angle, η, as follows:[10]

$$P_2^a/P_a^1 = \frac{A(\alpha,L_2)}{A(\alpha,L_1)} = [A(X^r, L_2) - \eta]/[A(X^r, L_1) - \eta], \quad \text{or}$$

$$\eta = \frac{[P_a^1 A(X^r,L_1) + P_2^a A(X^r,L_1)]}{P_1^2} \tag{2.20}$$

Where $A(p, q)$ is an angle between lines p and q.

2.3.6 Detector tilt angles, θ and ϕ

The detector can be tilted around the central detector row by an angle, θ or twisted around the central detector column by an angle, ϕ (Figure 2.12).

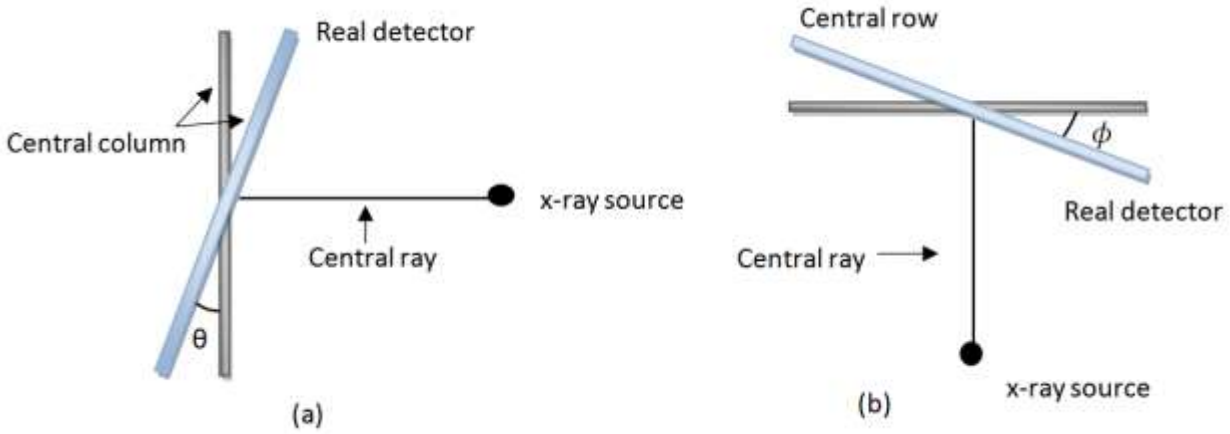

Figure 2.12: The detector angles θ and ϕ specify the tilt of the virtual detector around its (a) x-axis (X^v) or central row and (b) y-axis (Y^v) or central column respectively.

When the detector is tilted around the central detector row different slices are projected onto the same position of the detector. The accuracy of the reconstruction process will be reduced when this data is used for reconstruction of CT images.[44]

When the detector is tilted around the central detector column the width of the detector becomes 'smaller' as seen from the x-ray source. Although the reconstructed images will be smaller than the ideal situation and the resolution will be lower, the structure of the image will not change. [44]

Looking at Figure 2.13 it can be seen that the axis of the divergent plane is parallel to the Y^v axis which is parallel to the Z^w axis of the world coordinate system. Regardless of the detector tilt angle (ϕ), the divergent plane will intersect the detector plane unless θ is zero.

The converging point, P_θ, has the following relationship:

$$\alpha_\theta = Y_\theta^v \tan(\theta) \tan(\emptyset),$$

$$\beta_\theta = \frac{Y_\theta^v}{\cos(\theta)} = Z_s^v \cos(\emptyset) / \sin(\theta) \quad \text{and}$$

$$\tan \emptyset \sin \theta = \alpha_\theta / \beta_\theta \tag{2.21}$$

The position of the converging point $P_\theta = (\alpha_\theta / \beta_\theta)$, can be found from the point of intersection of all the lines connecting opposing pairs of BBs projected on the detector plane.

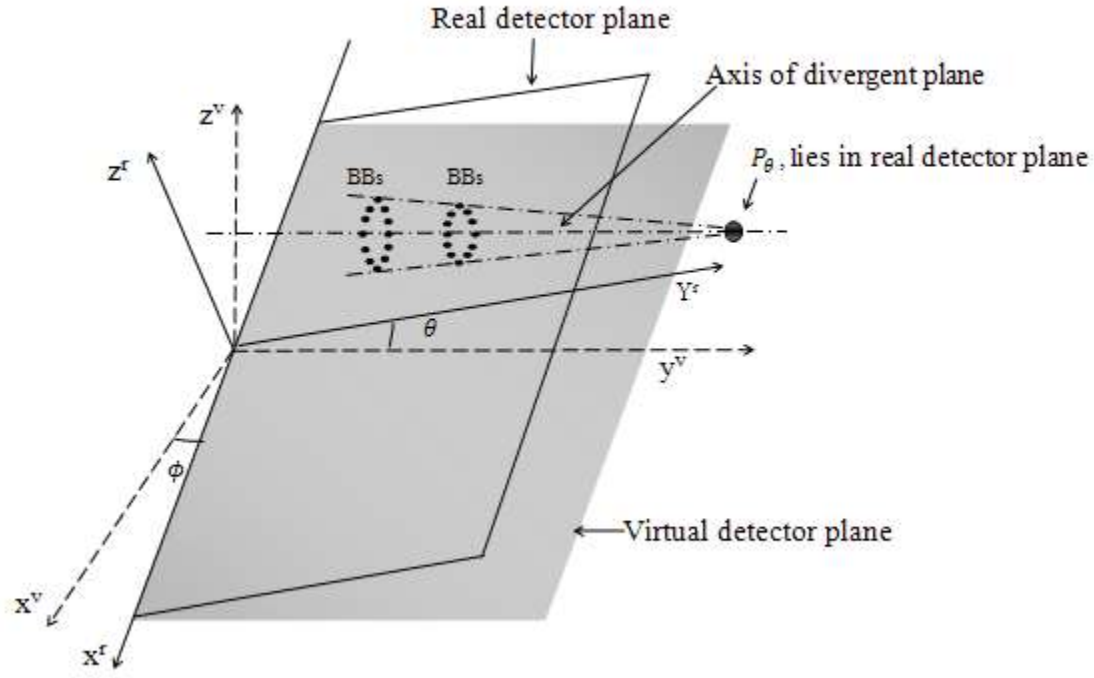

Figure 2.13: The converging point, P_θ, due to detector tilt angle, θ, is shown (see section 2.3.3.). The axis of the divergent plane can be found by connecting opposing pairs of BBs. This axis is parallel to the Y^v axis and will intersect the detector plane unless θ is zero (regardless of ϕ). The intersection of the axis of the divergent plane and the detector plane represents the converging point, P_θ.

The x-axis component of the source position in the virtual detector system is zero. The z axis component of the source position in the real detector coordinate system (z_s^r) can be found by using rotation matrices:[10]

$$z_s^r = Z_s^v \cos\theta \cos\emptyset + Y_s^v \sin\theta$$
$$= \sin\theta \cos\theta \left[\beta_\theta + Y_s^v/\cos\theta\right] \quad (2.22)$$

β_θ and $Y_s^v/\cos\theta$ can be determined from the converging point, $P_\emptyset$. The z axis component of the source in the real coordinate system is therefore simply a function of the detector angle, θ.

2.4 Image quality

Patient set up verification involves the registration of reconstructed CBCT images (acquired in the treatment room) with reference images from treatment planning. Reconstructed images need to be of high quality to ensure accurate registration of these two data sets. The measurement of image quality describes the visibility of clinically important information on an image (soft tissue or bony landmarks). By quantifying the imaging performance of a system we can decide whether or not the system will be adequate for the purpose needed eg. patient set up verification. Parameters such as uniformity and noise, contrast resolution and spatial resolution can be used to quantify image quality.

2.4.1 Uniformity and noise

Uniformity is a way to measure image noise by comparing pixel values in a homogenous material.[11] If a perfectly homogenous phantom is scanned we would expect all pixel values to be the same. Deviations from uniformity are due to the statistical emissions of photons from the source and are called noise. The standard deviation of the pixel values is a measure of the noise.

The noise in a specified region of interest (ROI) would be:[11]

$$\sigma = \sqrt{N} \tag{2.23}$$

where N is the number of photons recorded in the ROI. Uniformity is represented by the mean value of the ROI.

Relative noise or coefficient of variation (COV) is the image noise as perceived by a human observer.[6]

$$Relative\ noise = COV = \frac{\sigma}{N} \tag{2.24}$$

As the number of photons increase the relative noise will decrease. The inverse of the relative noise is the signal to noise ratio (SNR),[6]

$$SNR = \frac{N}{\sigma} = \frac{N}{\sqrt{N}} = \sqrt{N} \tag{2.25}$$

Image quality is largely dependent on the SNR. An increase in the number of photons will result in an increased SNR and therefore improved image quality. This improved image quality comes at a cost. To double the SNR the number of photons needs to be increased by a factor of four which means the dose to the patient will increase with a factor of four. The aim is to obtain good quality images with minimum dose to the patient. There is thus a trade-off between SNR and dose to patient.

2.4.2 Spatial and Contrast resolution

Resolution can be divided into two components, spatial resolution or resolving power and contrast resolution. Spatial resolution is an indication of the sharpness of the image and is generally described by the amount of line pairs per millimeter (lp/mm) visible. Typically high

contrast objects, such as lead wires, are arranged in groups so that each group has a different resolution (associated lp/mm value). The term line pair refers to the line and the space between the lead wires. For example, 4 line pairs per mm means there are 4 lead wires per mm, with each lead wire 1/8 mm wide and each space 1/8 mm wide, so that each line pair is 1/4 mm wide. A visual inspection of the image determines the group in which the line pairs can still be seen separately. This represents the spatial resolution of the image.

Contrast resolution is the ability to display objects with small density differences as distinct objects. Low contrast objects would be more visible if the background of the image is uniform. As mentioned earlier the uniformity is a function of noise. Thus, to improve contrast the noise should be reduced by increasing the number of photons reaching the detector. This would ensure a more uniform background and enhanced contrast resolution.[11]

The level of contrast is generally quantified by the contrast-to-noise ratio (CNR) which calculates the mean and standard deviation of the pixel values of an object and the homogenous background surrounding the object.[16,17]

$$CNR = \frac{|S - S_{BG}|}{\sigma} \qquad (2.26)$$

where S and S_{BG} are the mean pixel values in the insert and background region respectively, and σ is the average standard deviation of the pixel value in the insert and the background.

Spatial resolution, contrast resolution, image noise and radiation dose are all related to each other. Spatial resolution can be improved by increasing the amount of radiation absorbed by the detector, but this will result in (I) higher noise levels which will decrease contrast resolution and

(II) larger dose to the patient. Increasing scan times (larger dose) will improve contrast resolution but spatial resolution may be decreased due to the possibility of patient movement during the longer scan.[11]

2.4.3 Image artifacts

During image reconstruction of an object the ideal situation would be an image which is a 'true' representation of the object. This is rarely the case due to several sources that will degrade the image. Stochastic noise (also called random noise) is the most common source of image degradation. Quantum noise is an example of such a random process and is governed by the number of x-ray photons absorbed in the detector.[6] Non-stochastic deviations from the 'true' image are referred to as image artifacts. According to their origin artifacts can be grouped into the following categories: (a) physics-based, resulting from the physical process of the acquisition of data; (b) patient-based, caused by movement of the patient during image acquisition; (c) scanner-based, resulting from imperfections or defective pixels in the imaging system; and (d) helical and multi-section due to the reconstruction technique.[3] Usually image artifacts are reproducible for repeated scans. Some of the most common artifacts relevant to CBCT will be discussed in the following section.

2.4.3.1 Beam hardening

Photon beams used for image acquisition in MV CBCT are poly-energetic. Low energy photons will therefore be absorbed more rapidly than high energy photons and the beam will become hardened e.g. the mean energy increases. Two artifacts called cupping- and streak artifacts can arise due to this phenomenon. *Cupping artifacts* occur when the beam passes through a relatively uniform object such as the brain. The beam reaching the central portion of the object will be

hardened compared to the entrance beam on the periphery of the object. As the beam becomes hardened the rate of attenuation decreases resulting in image intensity decrease which is not representative of the object.[3,6] *Streak artifacts* occur when the beam passes through a heterogeneous material with objects of varying densities. Hardening of the beam will vary with detector position (gantry angle) causing dark bands or streaks that appear between dense objects.[3,11] Beam hardening artifacts can be rectified by using filtration, calibration corrections, and beam hardening correction software.[3]

2.4.3.2 Patient movement

The problem of patient movement arises in all imaging systems. This is also the motivation for the development of imaging systems with short scanning times. The scanning system assumes a stationary object, but when movement occurs some of the projection data will be backprojected in one orientation and other projection data in another orientation.[6] The reconstructed image will display movement as a streak in the direction of movement. Due to movements being random and unpredictable, no corrections can be applied. The best way to avoid these artifacts is to immobilize patients by means of appropriate restraints or devices. In paediatric cases sedation may be necessary. Respiratory motion can be minimized by breath hold techniques.[3,11]

2.4.3.3 Ring artifacts

Ring artifacts appear as dark or light circular bands on reconstructed axial slices. These bands are caused by the miscalibration of one of the detectors in the imaging system. The defective or dead pixel causes an erroneous reading for every angular measurement resulting in a ring artifact.[3] The radius of these rings is determined by the position of the defective pixel in the detector array.[11] These rings may not be visible on clinical images and would rarely be confused with

disease, but it will definitely reduce the image quality and therefore need to be corrected for. The detector should be calibrated by applying gain corrections to account for the variation in detector response under uniform x-ray irradiation conditions.[3]

2.4.3.4 The “cone-beam” artifact

The cone beam artifact is associated with a simple circular source-detector geometry. According to the condition by Kirillov and formulated by Tuy and Smith [46] for exact reconstruction it is required that every plane passing through a voxel in the reconstruction intersects the source-detector plane. If the source trajectory does not fulfill this condition no exact reconstruction can be expected due to an incomplete data set.[46]

As the source-detector system rotates around the object each detector collects data along a specific projection angle as the arc is completed. The data collected corresponds to the volume contained in the specific projection angle. Due to the cone-shaped beam being used the data collected for peripheral structures is reduced because the outer detectors record less attenuation than detectors in the central part of the detector.[3,41] This leads to increased noise, reduced contrast and artifacts similar to those caused by partial volume around off-axis objects.[3]

2.5 MV CBCT dose

A big concern regarding MV CBCT is the dose received by the patient during image acquisition. This is mainly due to relatively large doses necessary to obtain images with acceptable image quality. In 3D MV imaging the development of more advanced technologies such as increased sensitivity of the detectors and restriction of the imaging volume to the treatment volume have reduced the doses to clinically acceptable levels (low compared to therapy doses, ± 12 cGy). The dose received can easily be incorporated into the patient’s treatment plan.[17,33]

Chapter 3

Materials and methods

3.1 Image reconstruction

The Interactive Data Language (IDL) software package [13] was used to develop tools for reconstruction of transversal images from a set of planar cone-beam projections (see Appendix A & B). The reconstruction was performed by a filtered backprojection (FBP) algorithm based on analyses presented in literature (Feldkamp-type algorithm).[15,24] The Feldkamp-type algorithm uses an approximation of the FBP through a weighting function. The weighting factor compensates for longer paths the photons have to travel at larger cone angles (width of beam in patient direction). The steps followed in the main algorithm are explained in the following chart:

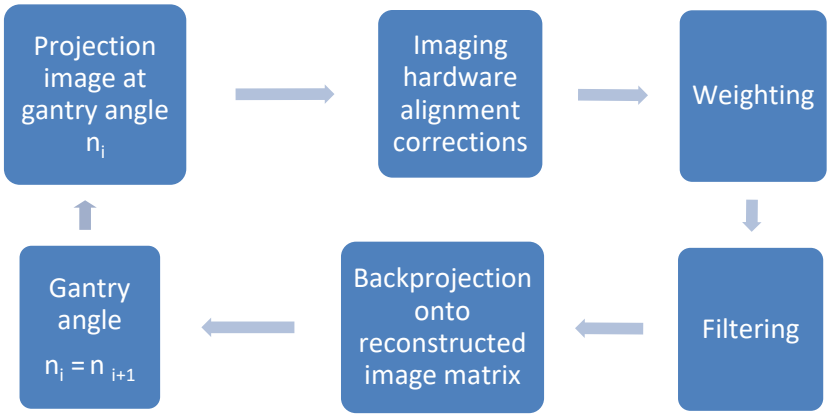

Figure 3.1: Steps followed in the main algorithm to reconstruct 2D transversal images from projection images acquired at a series of gantry angles.

3.1.1 Angular range

For a complete 3D reconstruction of an object planar images should be acquired over an angular range of at least 180º plus the fan angle.[24] For the system used in this study the fan angle was calculated using the following equation:

$$\emptyset_{fan} = 2\tan^{-1}\left[\frac{detector\ width}{2\ SDD}\right] = 2\tan^{-1}\left[\frac{40\ cm}{2\times160\ cm}\right] = 14.25° \qquad (3.1)$$

where SDD is the source-to-detector distance. The minimum arc requirement for a complete 3D reconstruction is therefore ~195°. An arc of 200º was used in this study.

3.1.2 Phantom setup

An anthropomorphic head phantom (Rando head phantom) was setup (Figure 3.2) at the isocenter of the treatment machine (Elekta Precise linac). Projection (cone-beam) images were acquired using a 200º arc with one degree angular intervals (from -100° to 100° gantry angle). One monitor unit (MU) per image was delivered using an 8 MV x-ray beam. The field size was set at 25 x 25 cm^2 at the isocenter, corresponding to a 40 x 40 cm^2 field at the detector plane. Image size is 1024 x 1024 pixels with a pixel size of 0.025 cm/pixel at the isocenter and 0.04 cm/pixel at the detector plane. The source-to-axis distance (SAD) and SDD is 100 cm and 160 cm respectively.

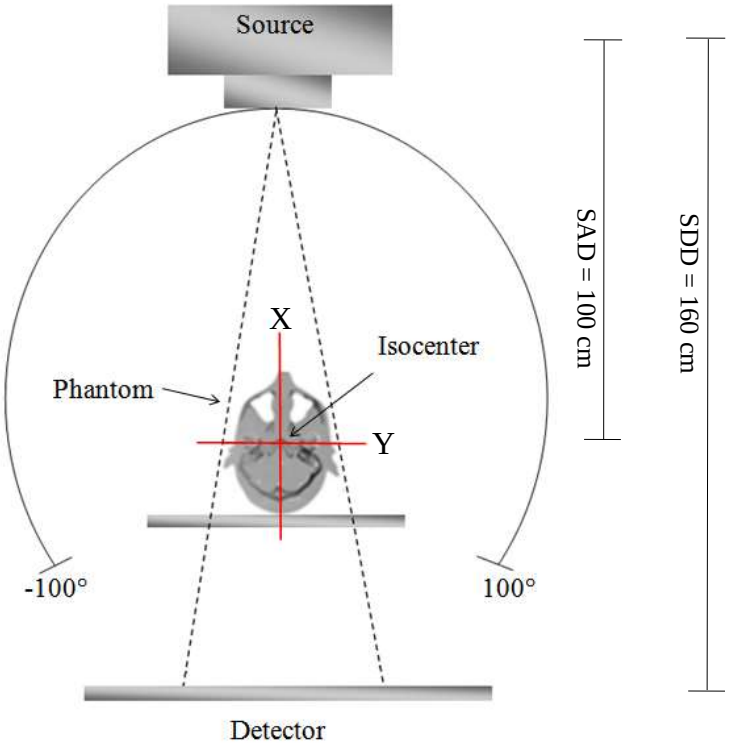

Figure 3.2: The Rando head phantom was setup at the treatment isocenter and projection images were acquired in angular intervals of one degree from gantry angle -100° to 100°.

Reconstruction is done by filtering and backprojecting a single plane (slice) within the cone. In other words, reconstruction is done separately for each elevation (z-position) in the cone. By summing the contributions from each tilted fan beam (slice) a 3D volume data set of the object can be obtained.

Prior to slice reconstruction, image row profile data is corrected for (I) detector offset, (II) detector rotation and, (III) gantry angle variation using look-up tables compiled for each parameter (I-III). These corrections were determined for each gantry angle. Detector offset and rotation was determined by performing geometric calibration (see section 3.2) of the imaging system. Gantry angle correction was made using the readout from the Elekta desktop instead of

the nominal gantry angle (90.3° instead of exactly 90°) since it presents a more accurate reflection of the true gantry angle.

The corrected profile data is multiplied by the weighting factor to compensate for longer path lengths of photons at large cone angles. The weighted data is filtered by convolving the projection profile with a sinc filter function in the spatial domain (see section 2.2.2). The filtered profile is then backprojected onto a reconstruction grid/matrix.

After backprojection of the row profile data of one gantry angle the procedure is repeated for the next gantry angle, this continues until all 200 angles are backprojected onto the reconstruction grid. The backprojection data at each gantry angle is summed to yield the 2D transversal images at the specific z-position of the phantom.

3.2 Geometric calibration

Geometric calibration was performed by using an in-house developed phantom containing two circular patterns of BBs (see Figure 2.6). The phantom was setup at the treatment isocenter as indicated by the in-room laser system (Figure 3.3). Since all measurements are referenced to the phantom, it is not necessary to position the phantom with great accuracy in the world coordinate system. Projection images for a range of gantry angles (from -100° to 100° with 1° intervals) were acquired. The posing parameters (see section 2.3), describing the geometry of the imaging system, were then determined by analyzing the elliptic pattern of the BBs when projected onto the detector plane.

Figure 3.3: Geometric calibration was performed using an in-house developed phantom containing two circular patterns of BBs setup at the nominal treatment isocenter. The central axis of the phantom was set up coincident with the linac axis of rotation. Projection images for a range of gantry angles were acquired. These images were analyzed to determine the posing parameters describing the geometric stability of the system.

3.2.1 Determination of projected isocenter (piercing point)

The projected isocenter (sometimes referred to as piercing point) is the projection of the central axis of the linac on the detector plane. Two methods were used and compared to determine the piercing point. In the first method a single BB was placed at the nominal treatment isocenter [21] and in the second method two rings of BBs (calibration phantom) were used.[10]

Method 1:

A small ball bearing (diameter 4 mm) attached to a perspex rod was setup at the nominal treatment isocenter as indicated by the in-room laser system (Figure 3.4). A field size of 2 x 2

cm^2 was used. EPID images of the BB were acquired at 30° gantry angle intervals as the gantry was rotated through 360°. Analysis tools were built using the IDL development package to determine the maximum pixel value in a defined region of interest (ROI) on the EPID image for each gantry angle (Figure 3.5). This value was taken as the centroid position which represents the position of the central axis on the detector plane. A calibration curve of centroid position vs. gantry angle was generated.

Figure 3.4: The setup used for determination of the piercing point using a single BB attached to a perspex rod is illustrated. The BB is setup at the isocenter as indicated by the in-room laser system. Projection images are acquired and analyzed at 30º angular intervals for a 360º rotation.

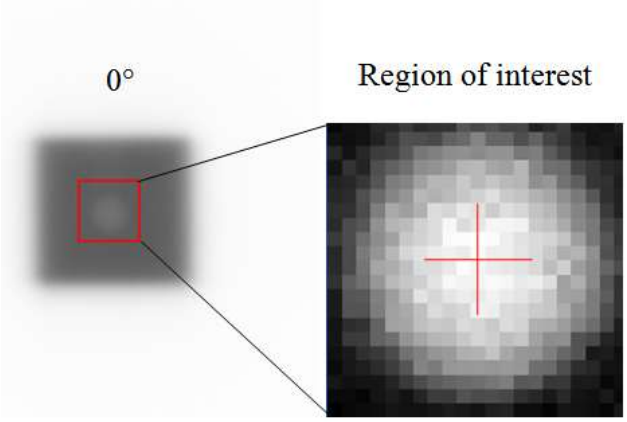

Figure 3.5: Illustration of a ROI drawn in around the single BB on the EPID image for gantry angle 0°. The centroid or position of the central axis on the detector plane is found by determining the maximum pixel value in the ROI.

Method 2:

The calibration phantom was setup and imaged as described in section 3.2. The projection images of the elliptical BB patterns were analyzed to determine the piercing point. Firstly, the center of each BB was obtained by drawing a region of interest around each BB on the projection image and determining the maximum pixel value in that region (Figure 3.6). This was done for each gantry angle from which a planar image was taken with the EPID, thus for 200 projections images.

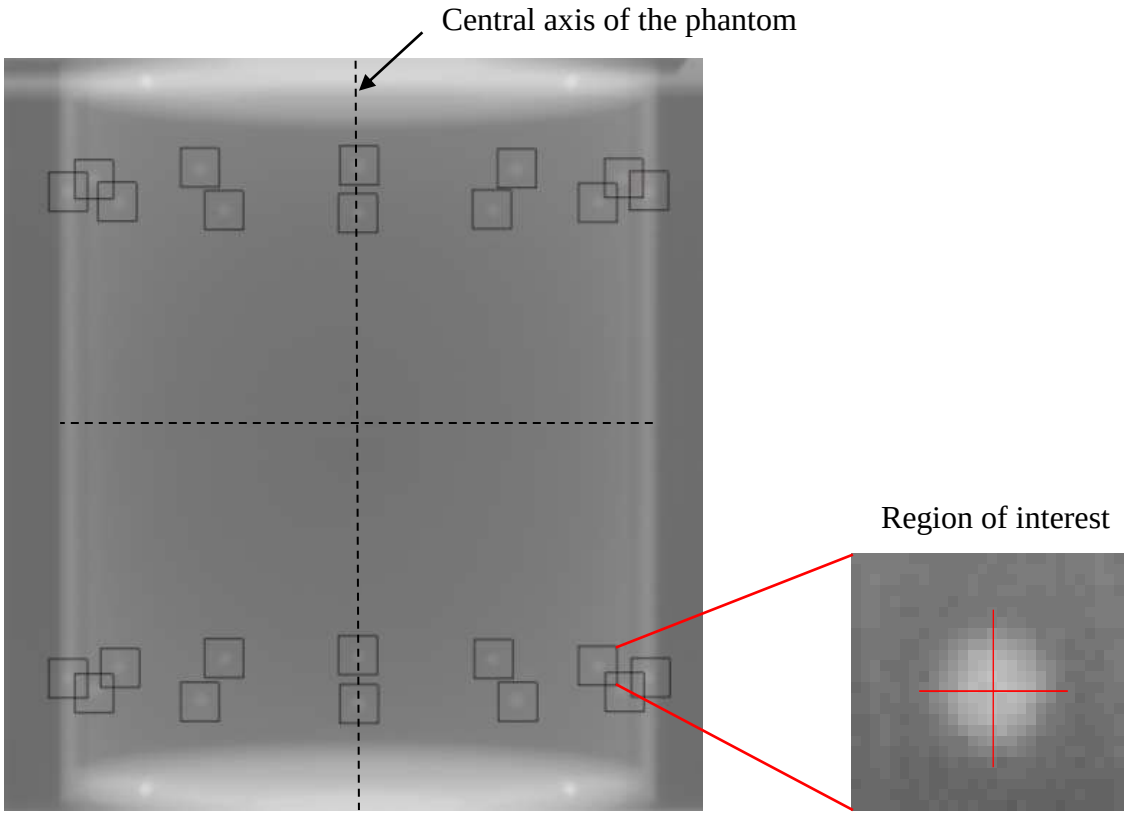

Figure 3.6: A projection image of the cylindrical phantom for gantry angle = 0° can be seen on the left. To determine the piercing point, the center of each BB should be obtained. This is done by drawing a region of interest around each BB and determining the maximum pixel value in that region (see inset).

Lines are then generated to connect opposing pairs of BBs (contra laterally) of the two ellipses traced out by the two sets of BBs (see Figure 3.7). These lines are drawn from the center of each BB as determined previously. The intersection of all these lines on the detector plane yields the piercing point for the specific gantry angle.

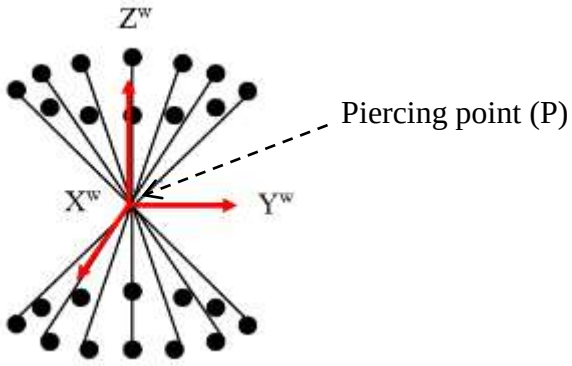

Figure 3.7: Lines are generated connecting opposing pairs of BBs (contra laterally) from the projected ellipses. The intersection of all these lines represents the piercing point (P). The world coordinate system is indicated.

3.2.2 Detector rotation angle, η

The shape of the ellipse on the virtual detector plane is dependent on the position of the source relative to the phantom (Figure 2.11). By analyzing the characteristics in the circular pattern of the BBs and the resulting projected elliptical pattern the detector rotation angle, η, can be determined. Figure 2.11 and equations 2.18 & 2.19 were used to determine the rotation of the detector around its normal axis.

3.2.3 Detector tilt angles, θ and ϕ

The converging point (P_θ), which is due to the detector tilt angle θ, can be found by connecting pairs of BBs as shown in Figure 3.8.[10] The intersection of all these lines yields the position of the converging point (P_θ).

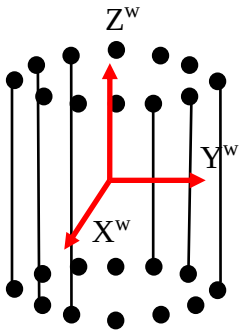

Figure 3.8: Lines are generated connecting pairs of BBs that are parallel to the Z^w axis. The intersection of all these lines represents the converging point, P_θ, due to detector tilt angle, θ. The world coordinate system is indicated.

By determining the intersection of two lines (see Figure 3.10), one from equation (2.21), the converging point, and the other from the ellipse model using equations (2.17),(2.18) and (2.22) the solution of θ and ϕ can be determined.

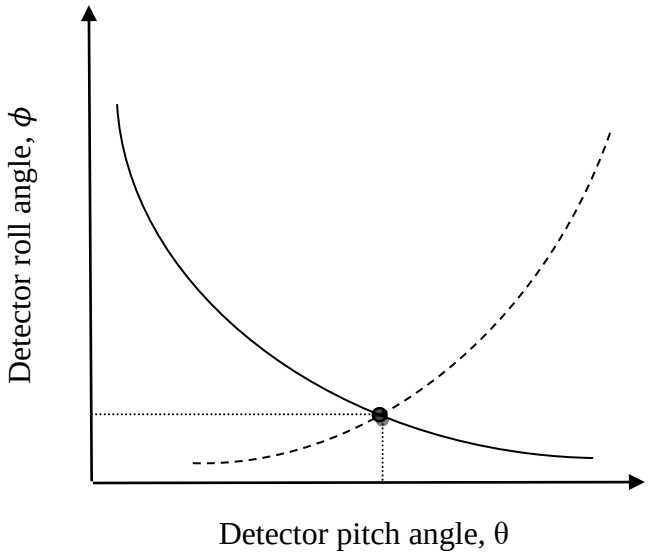

Figure 3.9: The detector tilt angles ϕ and θ can be determined by the intersection of two curves. One from equation (2.21) and the other from the ellipse model, Eqs. (2.17), (2.18) and (2.22).

3.3 Image quality

A commercially available CT image quality phantom (Catphan 500, The Phantom Laboratory, Salem, NY) was used to evaluate the image quality of the reconstructed images. The phantom consists of several modules representing test objects for various image quality parameters eg. uniformity and noise (CTP486 module), low contrast resolution (CTP515 module) and spatial resolution (CTP528 module).

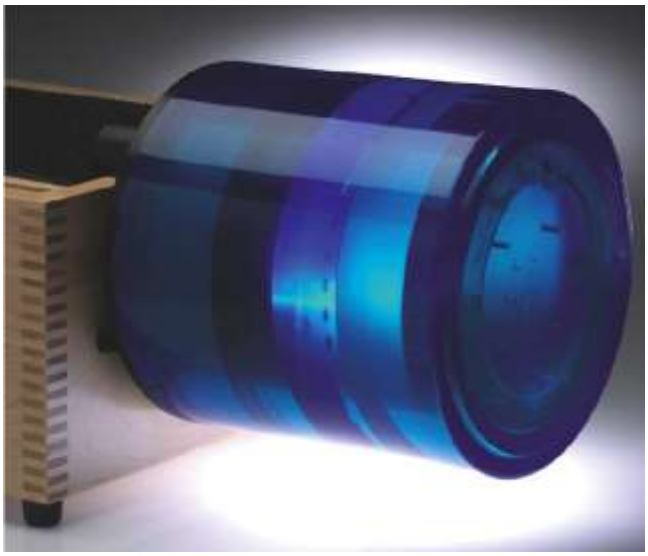

Figure 3.10: The Catphan® 500 phantom used for evaluation of image quality of the reconstructed images.[1]

The center of the phantom was set-up at the treatment isocenter as indicated by the in-room laser system (long axis in line with rotation axis of linac). Projection images at gantry angles ranging from -100° to 100° (at 1° intervals) were acquired. Transversal images were reconstructed to evaluate image quality. The same imaging protocol as described in section 3.1 was used to replicate the conditions of image acquisition and reconstruction used in this study.

3.3.1 Uniformity and noise

The uniformity module in the phantom is a volume containing a homogeneous material. For this section five rectangular regions of interest (ROIs) were drawn in on the reconstructed image. One region was drawn in the center and four at the periphery at 0, 90, 180 and 270 degrees (Figure 3.11). Noise was determined by using the standard deviation of the pixel values in the ROIs and the uniformity by using the maximum range of mean values over the five ROIs.[16]

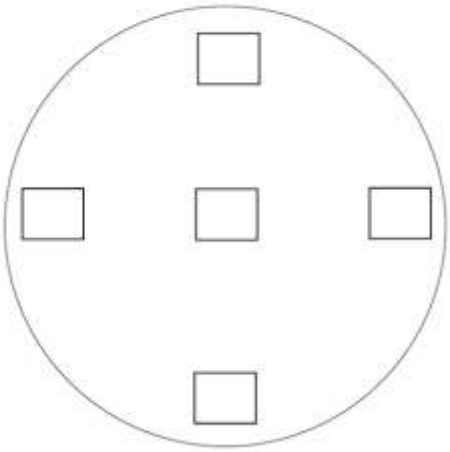

Figure 3.11: Five regions of interest (ROIs) are drawn in on the axial image of the uniformity module of the Catphan® 500 phantom to determine uniformity and noise. The uniformity and noise is represented by the range of mean values and standard deviation of the pixels in the ROIs respectively.

Uniformity is expressed as the integral non-uniformity by using the following equation:

$$Integral\ nonuniformity = \frac{mean_{max} - mean_{min}}{mean_{max} + mean_{min}} \qquad (3.2)$$

Noise in the reconstructed image is expressed as the SNR (signal-to-noise ratio) as explained in section 2.4.1.

Therefore, the level of noise in the reconstructed image is determined by:

$$SNR = \frac{\overline{mean}}{\bar{\sigma}} \tag{3.3}$$

where $\overline{mean}$ and $\bar{\sigma}$ is average of the mean pixel values and standard deviation in all the ROIs respectively.

3.3.2 Spatial resolution

The spatial resolution module consists of groups containing varying line pairs per centimeter. Resolution between 1 and 21 line pairs/cm can be tested. The gauge is cut from 2 mm thick aluminum sheets and cast into epoxy. In the gauge each group represents a certain gap size indicating the spatial resolution of the imaging system. The reconstructed image is visually inspected to determine the group of line pairs that can still be seen as separate lines which indicates the spatial resolution of the system.

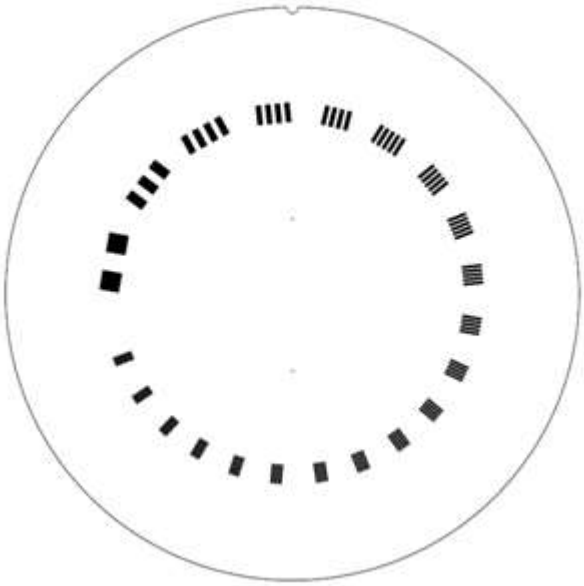

Line Pair/cm	Gap Size
1	0.500 cm
2	0.250 cm
3	0.167 cm
4	0.125 cm
5	0.100 cm
6	0.083 cm
7	0.071 cm
8	0.063 cm
9	0.056 cm
10	0.050 cm

Line Pair/cm	Gap Size
11	0.045 cm
12	0.042 cm
13	0.038 cm
14	0.036 cm
15	0.033 cm
16	0.031 cm
17	0.029 cm
18	0.028 cm
19	0.026 cm
20	0.025 cm
21	0.024 cm

Figure 3.12: The spatial resolution gauge of the image quality phantom consists of 21 line pair groups.[1] The spatial resolution of the imaging system is represented by the group of line pairs in which the lines can still be seen seperately. This is done through visual inspection of the reconstructed image.

3.3.3 Contrast resolution

Due to the reduced levels of contrast obtainable in megavoltage imaging, contrast resolution was evaluated by visual inspection of the sensitometry module in the imaging phantom. This module consists of four sensitometric samples with different electron densities ranging from +1000H to -1000H. The samples are Teflon, acrylic, low density polyethylene and air. The reconstructed megavoltage image was compared to the kilovoltage CT image to quantify contrast resolution.

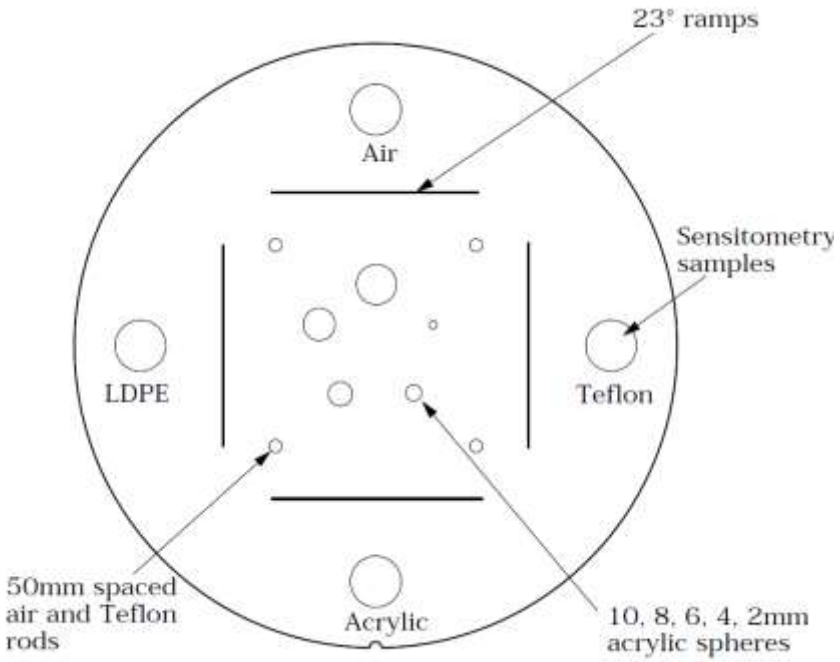

Figure 3.13: The sensitometry module of the Catphan consist sensitometric samples representing different electron densities.[1] The contrast resolution of the imaging system was quantified by noting the samples that can be distinguished through visual inspection.

3.4 Dose measurement

The image acquisition process delivers an arc of radiation from -100° to 100° gantry angle range in 1° intervals with 1 MU per angle adding up to a total of 200 MUs per image acquisition. The dose received by the patient during image acquisition was determined with three different methods; (I) ion chamber measurements, (II) film measurements and (III) the treatment planning system.

All measurements were performed using two cylindrical perspex phantoms each with a diameter and length of 30 cm and 15 cm respectively. The phantoms were attached to each other to yield a total phantom length of 30 cm which is a good approximation of the diameter of an average

patient. The center of the phantom was setup to coincide with the isocenter as represented by the in-room laser system (see Figure 3.15 for setup).

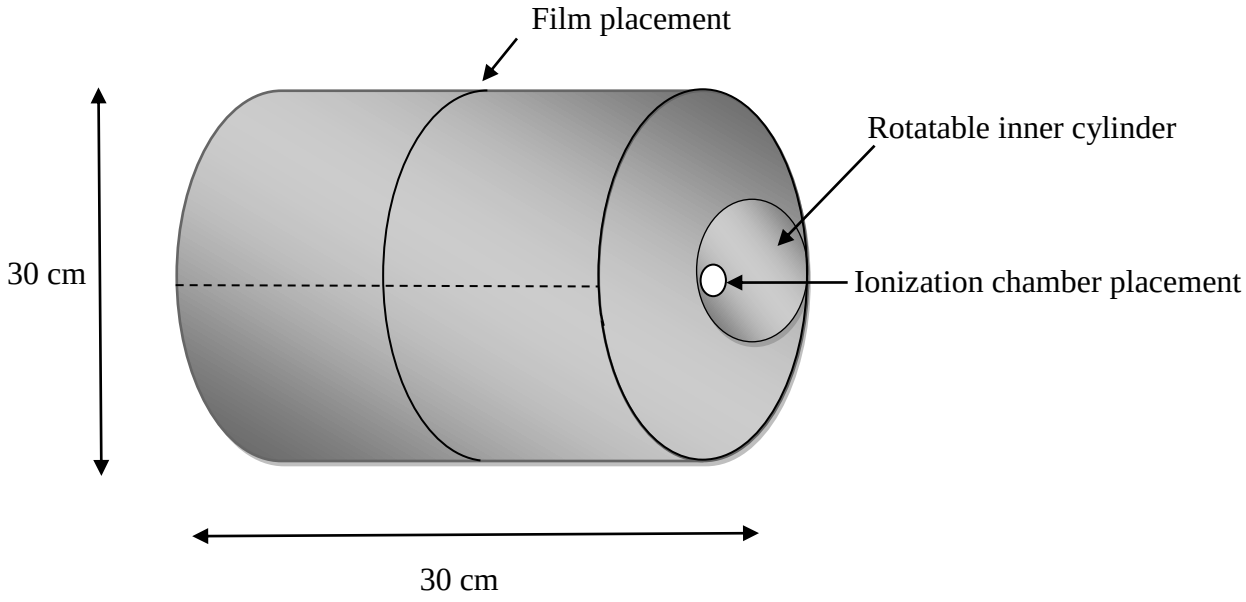

Figure 3.14: A cylindrical perspex phantom was used for dose measurements during image acquisition. The phantom has a rotatable inner cylinder inserted into an off center cavity with a hole to make provision for the placement of an ionization chamber. Film measurements were performed by sandwiching the film vertically between the two cylinders.

3.4.1 Ionization chamber measurements

The absolute dose was measured by placing a Farmer type ionization chamber (PTW 30012) in the hole of the rotatable inner cylinder provided for ionization chamber placement. The inner cylinder was rotated until the ionization chamber coincided with the center of the phantom (see Figure 3.16). A 25 x 25 cm^2 field (the same as used in the reconstruction process) was setup and the center of the phantom was positioned at the isocenter as represented by the in-room laser system. The active volume of the ionization chamber was thus setup to coincide with the center axis (CAX) of the radiation field. By setting the electrometer's interval time (time over which

the electrometer reading should be integrated) to its maximum the total dose delivered over the 200° arc was determined with the following equation:

$$Dose\ (cGy) = N_{D,W} \times C_{T,P} \times M \qquad (3.4)$$

Where, $N_{D,W}$ is the calibration coefficient in mGy/Displayed nC obtained from the calibration certificate of the electrometer ionization system, $C_{T,P}$ is the correction factor for temperature and pressure and M is the electrometer reading in nC.

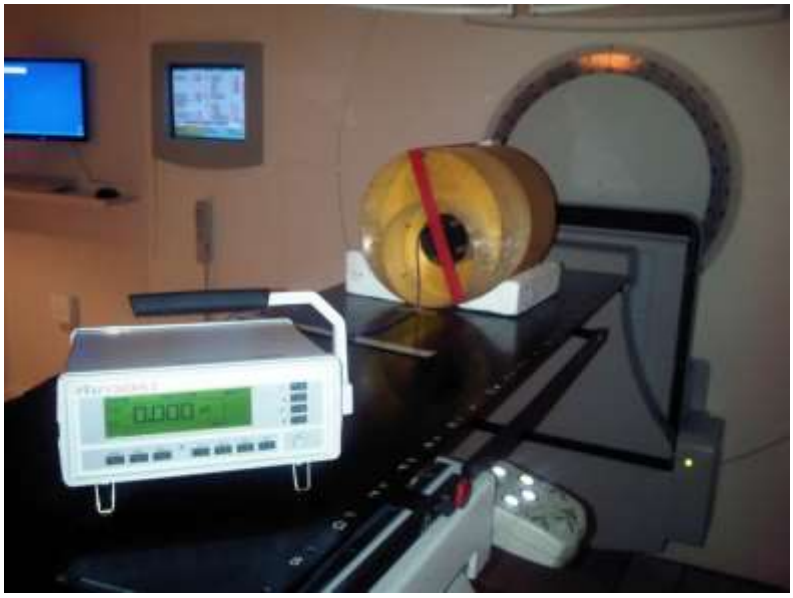

Figure 3.15 The ionization chamber and electrometer setup used to determine the dose delivered during the image acquisition process. The ionization chamber was placed in the center of a cylindrical perspex phantom such that the active volume coincides with the treatment isocenter.

3.4.2 Film measurements

The film measurement was performed by placing a Kodak Extended Dose Range (EDR2) film vertically between two cylindrical perspex phantoms (see Figure 3.16). The film was positioned in the gantry rotation plane intersecting the isocenter. Projection images from -100° to 100° with 1° intervals were acquired. The film was developed in a dark room and scanned with a Vidar scanner® for digital evaluation. Films were irradiated by increasing amounts of monitor units (1Mu = 1 cGy) to obtain a calibration curve for conversion of optical density to dose.

Figure 3.16: The film measurement setup used for determination of dose during image acquisition. An EDR2 film was placed vertically between two perspex phantoms and positioned to coincide with the treatment isocenter. The 200 MU protocol (-100º to 100º gantry angle, 1 MU/degree) was used to irradiate the film.

3.4.3 Treatment planning system

A treatment plan was computed on the Xio treatment planning system (Computerized Medical System, St Louis, MO). The perspex phantom was scanned on the conventional CT scanner and transferred to treatment planning to generate a plan using an 8 MV photon beam delivering 1 MU per degree for an arc of 200°. The dose in the center of the phantom at the isocenter plane was noted and compared to the dose of the ionization chamber and film measurements.

3.5 Positional accuracy and rotation

A standard method for assessing patient positioning accuracy is the acquisition of weekly port films before the actual treatment. A reference image usually obtained during the treatment stage is used to draw in bony structures using drawing tools. The portal image is superimposed on the reference image and the bony landmarks on both images are matched. The translation in the X and Y direction and rotation of the treatment field are recorded through matching software of the system. In this study the same principle was implemented; two images were used but instead of drawing in bony landmarks matching was done with three reference or anatomical points on both images. The translation and rotation was determined through mathematical procedures explained in the subsequent section.

The Rando head phantom was used to determine the accuracy of the reconstruction algorithm regarding the measurement of setup errors in terms of shift (lateral, superior-inferior and longitudinal) and rotation. Two sets of images (200 images per set) were acquired; the first set (for both shift and rotation) with the phantom setup more or less at the isocenter and the second with the phantom in the same position but the bed moved a known distance (2 cm) in a lateral, superior and longitudinal direction for determination of shift and rotated five degrees for

determination of rotation. The transverse images of these two sets were evaluated to determine if the shift of 2 cm in all the directions and rotation of five degrees could be measured.

The longitudinal shift was determined by locating the corresponding slices (detector row gun-target direction of linac), in terms of pixel number, on the shifted and 'original'/non-shifted image. The difference in slice position (pixel number) multiplied by the sampling interval (cm/pixel) yields the shift in the longitudinal direction.

The following equation was used:

$$shift\ in\ longitudinal\ direction = (S_1 - S_2)pixel \times (sampling\ interval)\frac{cm}{pixel} \qquad (3.5)$$

where S_1 and S_2 are the slice positions for data set one and two respectively.

The lateral and superior-inferior shifts were determined by choosing five corresponding points of interest (A-E) on a transversal image of each data set. The coordinate positions (in terms of pixel number) of the corresponding points were subtracted from each other and multiplied by the sampling interval (cm/pixel) to yield the shift in these two directions.

Image rotation was determined by choosing five corresponding points of interest (A-E) on both images. The rotation was determined by using the coordinate positions of these points and the following equation:

$$\cos\theta = \frac{a \cdot b}{|a||b|} \qquad (3.6)$$

where *a* and *b* are vectors from the origin of the image (center of image at pixel address (0,0)) to the coordinate position of point A on the transversal image from data set one and the

corresponding point A on the transversal image from data set two respectively. The angle θ between these two vectors represents the rotation angle.

The inter- and intra observer dependency for the determination of both positional accuracy and rotation was evaluated. For inter observer dependency five observers were asked to determine the positional accuracy and rotation for images reconstructed with backprojection intervals ranging from 1 degree to 15 degrees. These measurements were repeated by the author (five times) to determine the intra observer dependency. The results were compared and analyzed.

Chapter 4

Results and discussion

4.1 Image reconstruction

CBCT images were reconstructed from projection images acquired over a 200° arc using ~1.6 mm slice thicknesses and a 256 x 256 reconstruction matrix. A projection profile for each row in the image at each gantry angle was obtained. These row profiles (dashed line in Figure 4.1), corresponds to a specified z-position (longitudinal direction) on the projection image. They are (I) corrected for geometric misalignments and (II) filtered before they are backprojected onto the reconstruction matrix.

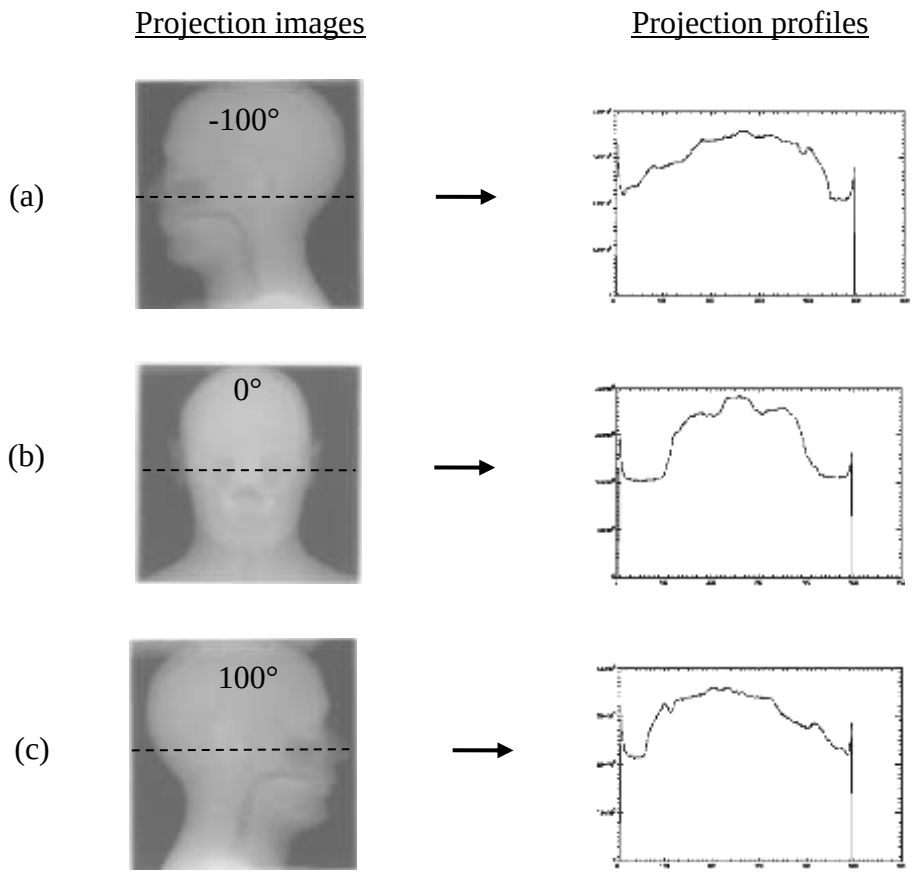

Figure 4.1: Projection images and their corresponding projection profiles of the Rando head phantom for gantry angles -100°, 0° and 100° respectively.

After geometric misalignment corrections (discussed in section 4.2) are applied, the profiles are convolved with a sinc filter function (Figure 4.2) before they are backprojected onto the reconstruction matrix to yield the reconstructed image (Figure 4.3).

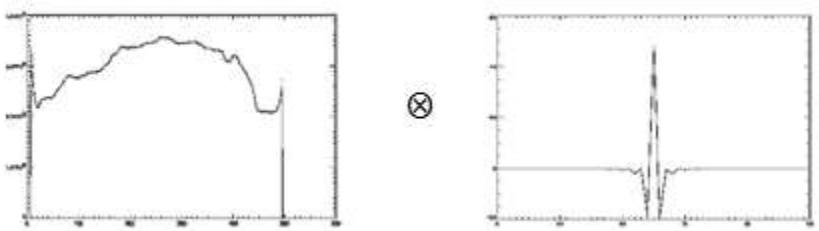

Figure 4.2: Profiles (left) are convolved with a sinc filter function (right) to reduce blurring and enhance detail in the reconstructed image.

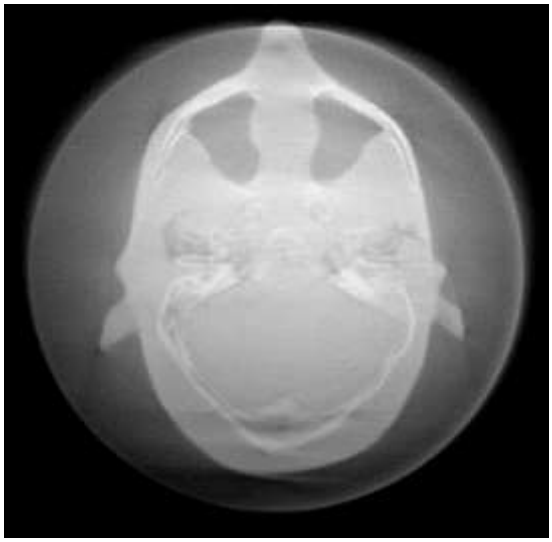

Fig 4.3: Reconstructed CBCT image of the Rando head phantom using a 200° arc with 1° increments.

The effect of the filter on the reconstructed CBCT image can clearly be demonstrated (Figure 4.4). Due to the high pass nature of the sinc filter function image blurring is reduced while detail in the reconstructed image is enhanced.

This filter amplifies high frequencies which also represents noise and will lead to some noise increase in the images. Noise can be reduced by applying a low pass filter (Shepp-Logan or Low Pass Cosine) or defining a window function in the backprojection algorithm.

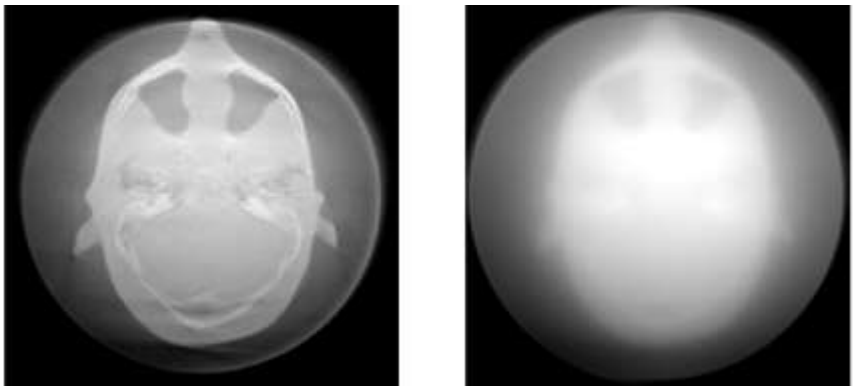

(a) (b)

Fig 4.4: The reconstructed image of the Rando head phantom (a) with and (b) without the sinc filter function applied.

Megavoltage x-ray interactions are dominated by Compton interactions in tissue equivalent materials. Thus, since relative electron densities are very similar for soft tissue, poor soft tissue contrast in planar and reconstructed images is observed. The contrast differences are of the same order as image noise and applying a smoothing filter to megavoltage images would practically remove tissue contrast. As a result the image would appear more homogeneous in the soft tissue domain.

Experiments were done using a smoothing filter in addition to the sinc filter function, but this degraded the overall image quality (contrast and resolution) of the reconstructed image significantly. On these grounds it was decided to only use the sinc filter function for reconstruction.

Image acquisition time is more or less an hour and a half due to the 'step-and-shoot' technique being used. This is impractical considering patient comfort and immobilization. The reconstruction time for one transverse slice is approximately two and a half minutes. Image acquisition and reconstruction time can significantly be reduced by using fewer projections i.e. backprojecting the profile for every second or third gantry angle instead of every gantry angle over the 200° arc. Using 2° instead of 1º increments the acquisition and reconstruction time can be reduced by a factor of ±2. However, there exists a trade-off between reconstruction time (number of projection images used for reconstruction) and the visual appearance of the reconstructed CBCT image (Figure 4.5). The window level and width for these images were not adjusted.

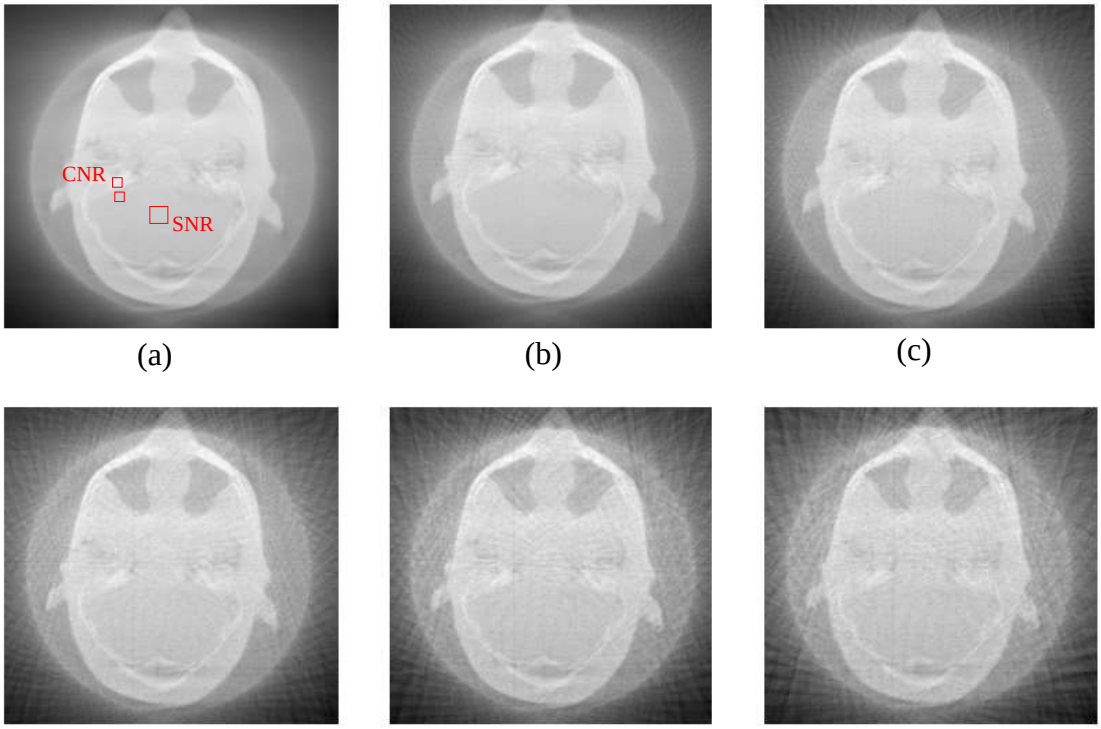

Figure 4.5: Reconstructed image of Rando head phantom with 200° arc in increments of (a) 1°, (b) 2°, (c) 3°, (d) 4°, (e) 5° and (c) 6°.

Based on grey scale values the signal-to-noise ratio (SNR) and contrast-to-noise ratio (CNR) was determined (see section 2.4) to illustrate the influence of the number of projection images used for reconstruction on these parameters (Table 4.1). To evaluate SNR a ROI was drawn in on a relatively uniform part of the image. CNR evaluation was done by drawing two ROIs, one on a bony landmark and one adjacent to that representing background (see figure 4.5 (a)).

Table 4.1: Influence of the number of projection images used for reconstruction on the signal-noise (SNR) and contrast-noise (CNR) ratios.

Image acquisition interval	SNR	CNR
1°	118.33	8.67
2°	94.97	6.47
3°	70.60	6.19
4°	59.61	6.23
5°	48.82	6.24
6°	50.05	6.35
7°	49.78	6.45
8°	44.15	5.95
9°	40.94	5.73
10°	39.64	4.57

As the number of projection images are reduced the noise increases causing both the SNR and CNR to deteriorate (Figure 4.6 & 4.7). The trade-off between number of projections and image quality is clearly demonstrated by the results in Table 4.1. Image quality will be discussed in more detail in section 4.3. In the next two figures the SNR and CNR are plotted.

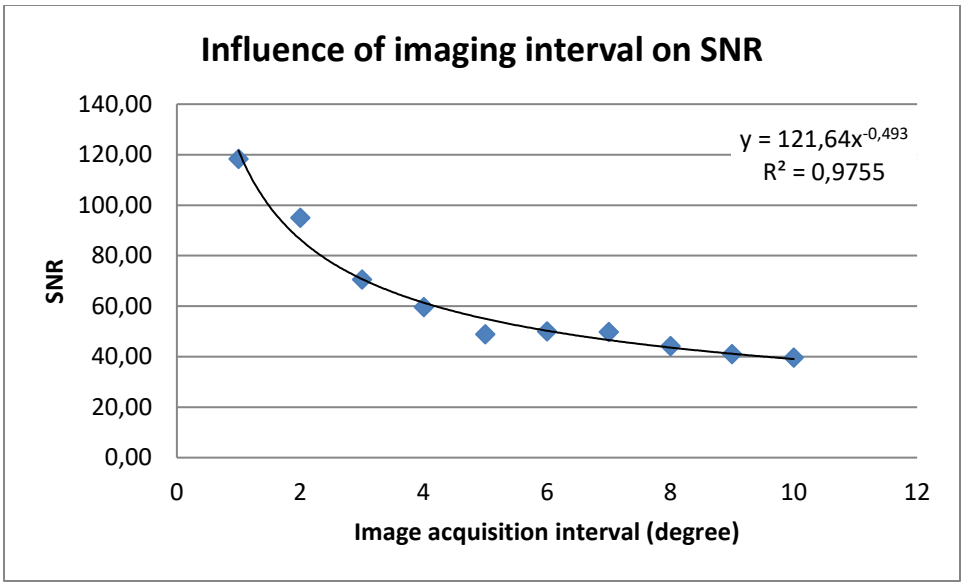

Figure 4.6: The influence of image interval used for reconstruction on the signal-noise ratio (SNR).

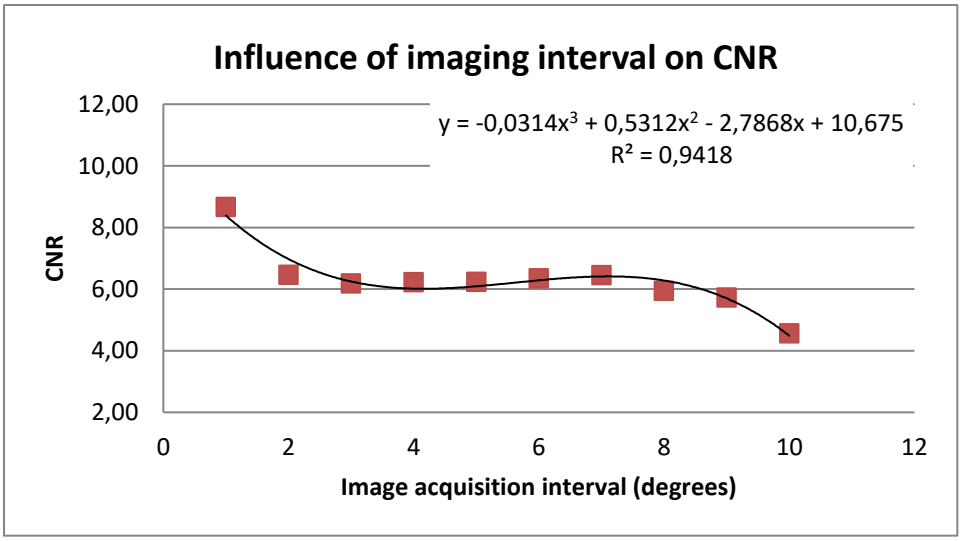

Figure 4.7: The influence of image interval used for reconstruction on the contrast-noise ratio (CNR).

From Figure 4.6 and 4.7 it can be seen that both the contrast-to-noise ratio (CNR) and signal-to-noise ratio (SNR) will get worse up to a certain image acquisition interval and then stay relatively constant for any further reduction in number of intervals used during image acquisition. For the CNR a further degradation is seen above image sampling rates of every eight images.

The SNR and CNR can be approximated with reasonable accuracy by using the functions fitted through these two data sets (equations are displayed on each graph). Knowing the level of CNR or SNR needed these equations can be used to determine the number of image intervals during image acquisition to achieve the optimal trade-off between image quality and dose delivered.

4.2 Geometric calibration

All the image alignment variations that will be discussed in this section are accounted for in the reconstruction process by adjusting the back-projection data to be consistent with the geometry of acquisition at the gantry angle of interest.

4.2.1 Piercing point

The piercing point and detector rotation angle, η, are the two parameters that will have the largest influence on the reconstructed image as discussed in 2.3.3 and 2.3.5. [25]

4.2.1.1 Method one – single BB:

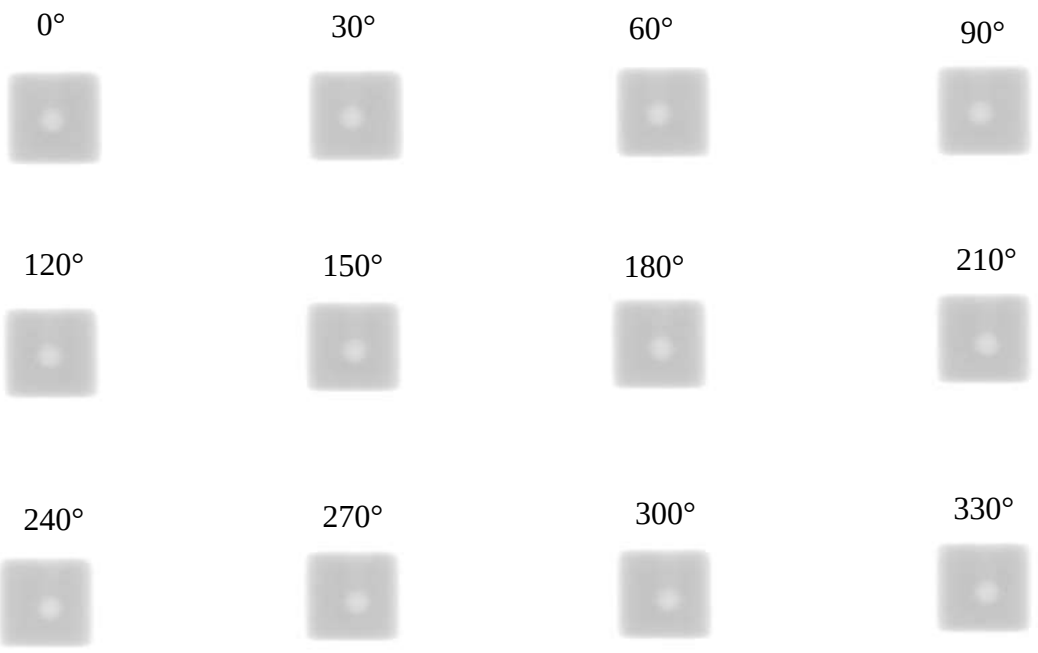

Figure 4.8: Images obtained of a single BB, attached to a perspex rod setup at isocenter, for a series of gantry angles. These images are used to determine the detector offset in the AB (left-right) and GT (gun-target) directions.

The position of the central axis on the EPID (piercing point) was determined by finding the maximum pixel in the ROI as explained in section 3.2.2. This was done for all gantry angles shown in Figure 4.8. These measurements were repeated on three separate days over a seven day period. The mean value of the three measurements was determine and is shown in Figure 4.9 and 4.10. The mean (u,v) location, where (u,v) is a pixel in the 2D detector domain, of the projected isocenter (piercing point) on the detector plane for all gantry angles measured is (513.5, 515.2), where the center of the 1024 x 1024 detector is denoted by (512,512).

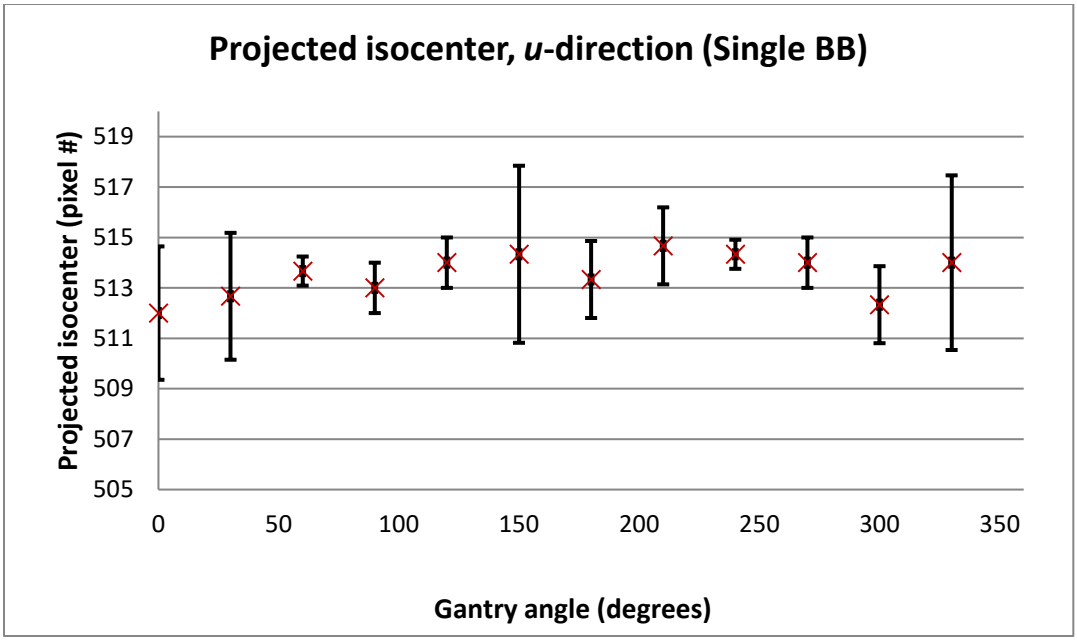

Figure 4.9: Results obtained for determination of the projected isocenter in the *u*- direction for three measurements over a 7 day period is illustrated. The standard deviation in the three sets is shown. Each set was measured on a separate day.

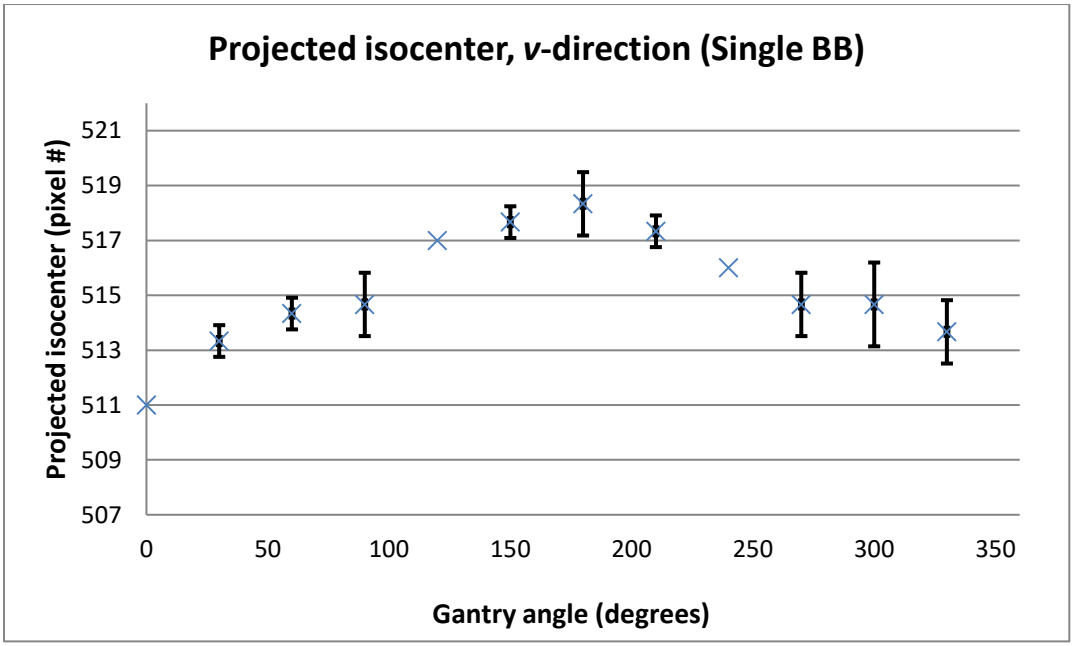

Figure 4.10: Results obtained for determination of the projected isocenter in the *v*- direction for three measurements over a 7 day period is illustrated. The standard deviation in the three sets is shown. Each set was measured on a separate day.

Table 4.2: The *(u, v)* coordinates of the projected isocenter for three measurements over a 7 day period.

	Day 1		Day2		Day3		Average		Standard deviation	
	u	v	u	v	u	v	u	v	u	v
0	513	511	510	512	509	511	509.50	341.00	2.65	0.00
30	515	513	506	512	510	514	508.00	352.00	2.52	0.58
60	514	515	512	514	513	514	512.50	362.67	0.58	0.58
90	512	514	514	515	514	516	514.00	373.67	1.00	1.15
120	514	517	516	519	515	517	515.50	385.33	1.00	0.00
150	514	517	518	518	518	518	518.00	395.33	**3.51**	0.58
180	513	519	519	518	515	517	517.00	405.00	1.53	1.15
210	515	518	516	517	516	517	516.00	414.67	1.53	0.58
240	514	516	515	516	514	516	514.50	424.00	0.58	0.00
270	514	514	514	517	513	514	513.50	433.67	1.00	1.15
300	512	513	510	515	511	515	510.50	443.33	1.53	**1.53**
330	516	513	509	515	510	515	509.50	453.33	3.46	1.15

From Figure 4.9 and 4.10 it can be seen that the reproducibility of this method over a period of 7 days is good with a maximum standard deviation of 3.51 pixels in the *u*-direction and 1.53 pixels in the *v*-direction. This corresponds to 0.88 mm and 0.38 mm respectively (pixel size is 0.25 mm at isocenter).

The pixel shift of the projected isocenter for each gantry angle is determined by calculating the difference in the projected isocenter and mean isocenter pixel locations. The maximum deviation for the 360° rotation is 4.5 pixels in the *u*-direction and 4.2 pixels in the *v*-direction corresponding to 1.13 mm and 1.06 mm (1 pixel equals 0.25 mm at isocenter) respectively. These deviations can be attributed to the flex of the gantry arm due to gravitational forces acting on the gantry system.[1] The overall motion due to these forces is less than 2 mm in both directions.

The ROIs drawn in on Figure 4.8 should be large enough to cover the entire BB but smaller than the field size of 2 x 2 cm^2. The effect of different sizes of ROIs on the projected isocenter (u,v) was evaluated. The results are shown in Table 4.3. When the ROI is larger than the field size used the maximum pixel would be on the outside of the field instead of on the BB (see Figure 4.11). From Table 4.3 it can be concluded that as long as the ROI is smaller than the field size (< 80 x 80 pixels) and covers the entire BB, the size of the ROI would not affect the measured shift. This makes this method robust enough to yield consistent and stable results.

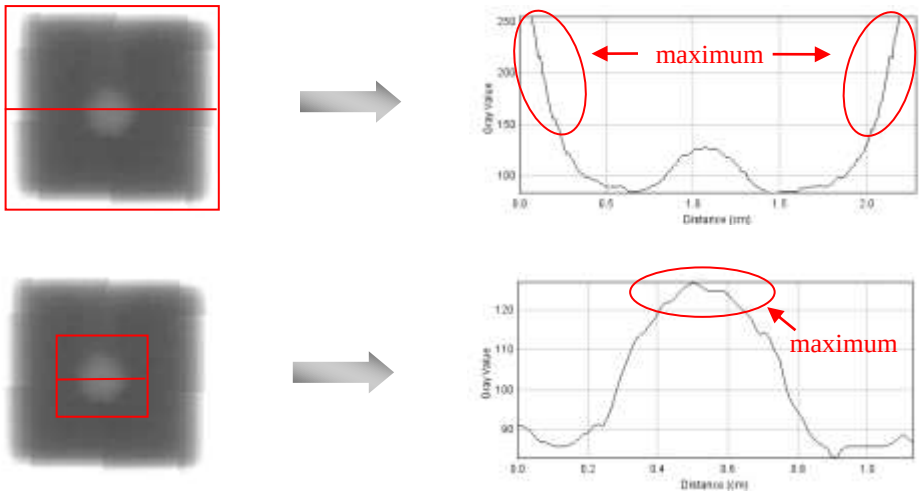

Figure 4.11: Profiles drawn through the ROIs to illustrate the influence of the size of a ROI on determination of maximum pixel value in the ROI. For ROIs larger than the field size the maximum pixel value will be on the edge of the field (indicated with ovals). ROIs smaller than the field size but large enough to cover the entire BB will yield the maximum pixel value in the center of the BB as expected.

Table 4.3: Results obtained to evaluate the influence of different ROI sizes on determination of projected isocenter.

	ROI size (pixels)							
	u				***v***			
	20x20	**30x30**	**40x40**	**80x80**	**20x20**	**30x30**	**40x40**	**80x80**
0	509	509	509	**468**	517	517	517	**476**
30	511	511	511	**470**	516	516	516	**474**
60	509	509	509	**471**	515	515	515	**475**
90	511	511	511	**472**	518	518	518	**476**
120	513	513	513	**474**	519	519	519	**478**
150	516	516	516	**556**	521	521	521	**479**
180	516	516	516	**557**	521	521	521	**479**
210	518	518	518	**558**	521	521	521	**477**
240	516	516	516	**559**	523	523	523	**478**
270	520	520	520	**560**	521	521	521	**479**
300	516	516	516	**561**	521	521	521	**481**
330	516	516	516	**558**	520	520	520	**479**

4.2.1.2 Method two – calibration phantom:

A mentioned previously, the isocenter (u,v) can also be determined for the EPID system using a specially designed calibration phantom (see section 2.3). Figure 4.12 shows one planar view of the phantom as detected by the EPID.

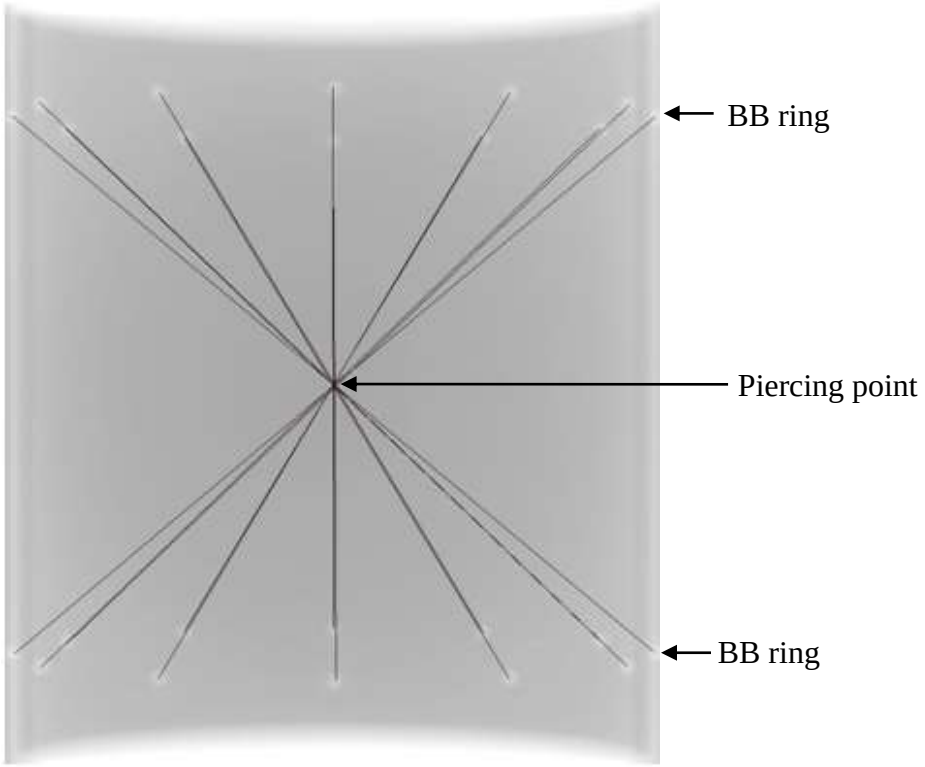

Figure 4.12: Lines are generated to connect opposing pairs of BBs on contra lateral sides of the phantom. The intersection of these lines indicates the piercing point.

Figure 4.12 illustrates the lines generated by connecting opposing pairs of BBs on contra lateral sides of the phantom. The intersection point (piercing point) was determined by computing the equation of each line and calculating the point where all these lines intersect each other. The variation in the piercing point (isocenter coordinates) for each gantry angle over the 200° arc is illustrated in Figure 4.13.

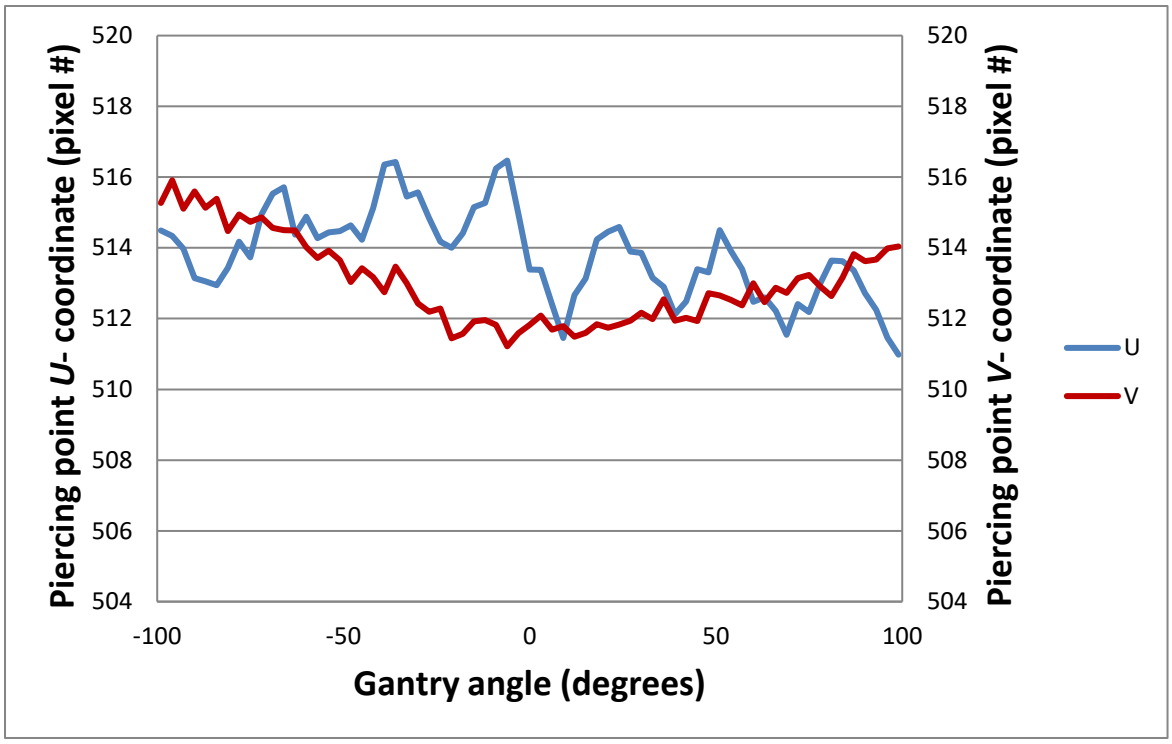

Figure 4.13: The *(u,v)* coordinates of the piercing point as a function of gantry angle. These values were obtained using the geometric calibration phantom.

The center of the 1024 x 1024 detector matrix is indicated by pixel position (512,512). The mean (*u*,*v*) location on the detector is (514,513) and the maximum deviaiton of the projected isocenter (piercing point) is within 3.0 and 4.2 pixels from that pixel address. These deviations correspond to 0.75 mm for the *u*-coordinate and 1.05 mm for the *v*-coordinate (1 pixel equals 0.25 mm at isocenter).

From the Figure 4.13 it can be seen that the deviation in the *u*-direction follows a repetitive pattern and in the *v*-direction almost a 180° period. As explained in the previous method, this can be attributed to flex in the arm of the detector and gravitational forces acting on the gantry as it rotates around the phantom or patient.[1] The overall movements in both directions is less than 2 mm.

The reproducibility of this method over a seven day period was evaluated. Three measurements on three separate days were performed.

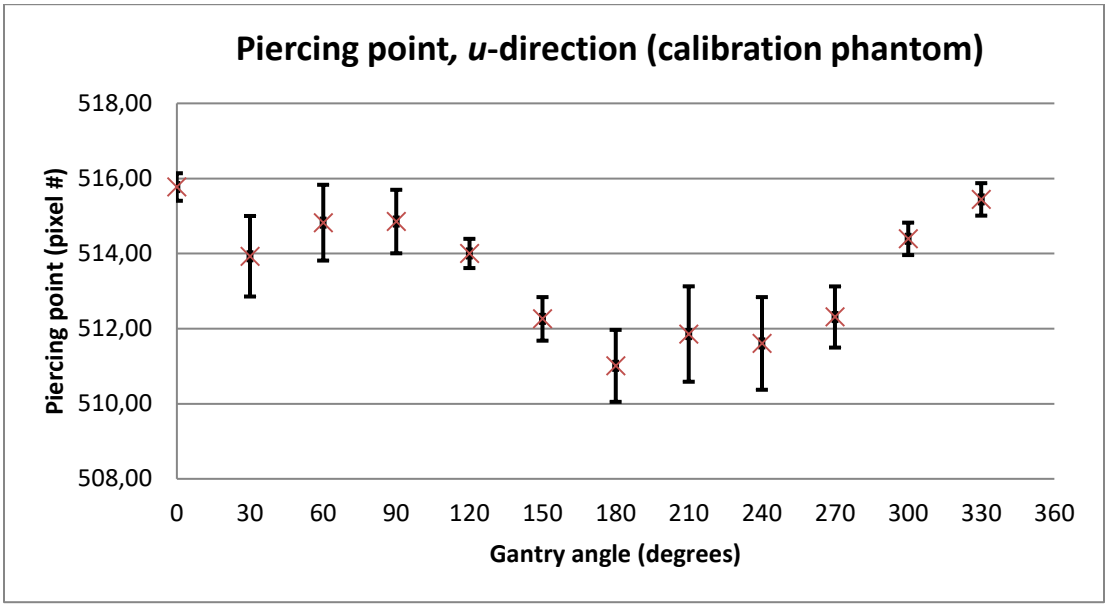

Figure 4.14: Results obtained for determination of the piercing point (projected isocenter) in the *u*-direction for three measurements over a 7 day period. The standard deviation in the three sets is shown. Each set was measured on a separate day.

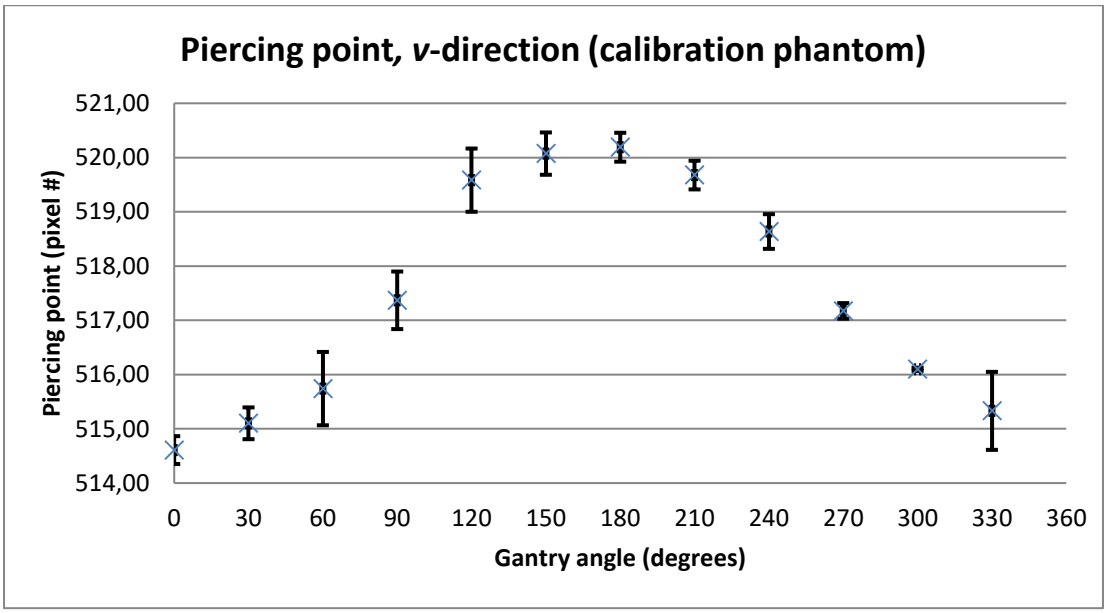

Figure 4.15: Results obtained for determination of the piercing point (projected isocenter) in the *v*-direction for three measurements over a 7 day period. The standard deviation in the three sets is shown. Each set was measured on a separate day.

The reproducibility in determination of piercing point (with calibration phantom) is illustrated in Figures 4.14 and 4.15. The maximum standard deviation is 1.27 pixels in the *u*-direction and 0.72 pixels in the *v*-directions. This corresponds to 0.32 mm and 0.18 mm. From these results it can be seen that this method yields reproducible results.

The mean (u, v) location for the single BB and calibration phantom method is (513,515) and (514, 513) respectively. The difference in these coordinates correspond to 0.25 mm in the *u*-direction and 0.5 mm in the *v*-direction. The deviations from the mean projected isocenter for each method is smaller than 2 mm. In both methods the deviations follow a repetitive pattern in the *u*-direction and a more or less 180° period in the *v*-direction illustrating the forces (previously mentioned) acting on the gantry head as well as on the EPID for the 360° rotation around the phantom.

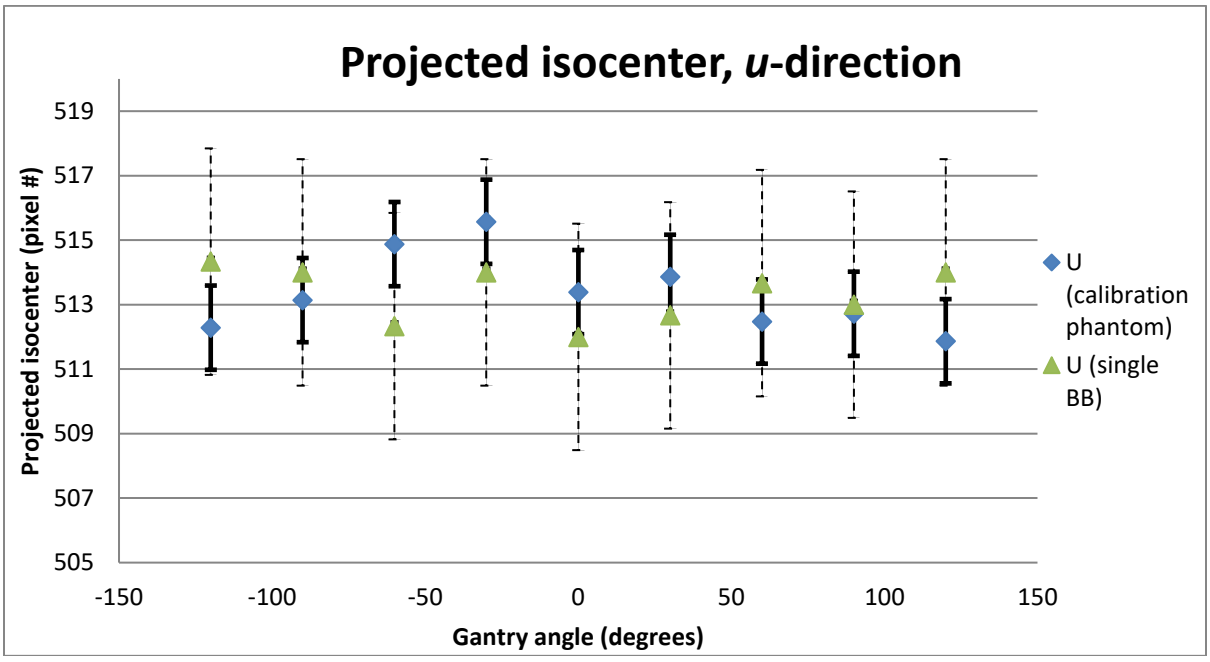

Figure 4.16: The difference in projected isocenter (*u*-direction) determined with the calibration phantom and single BB method respectively.

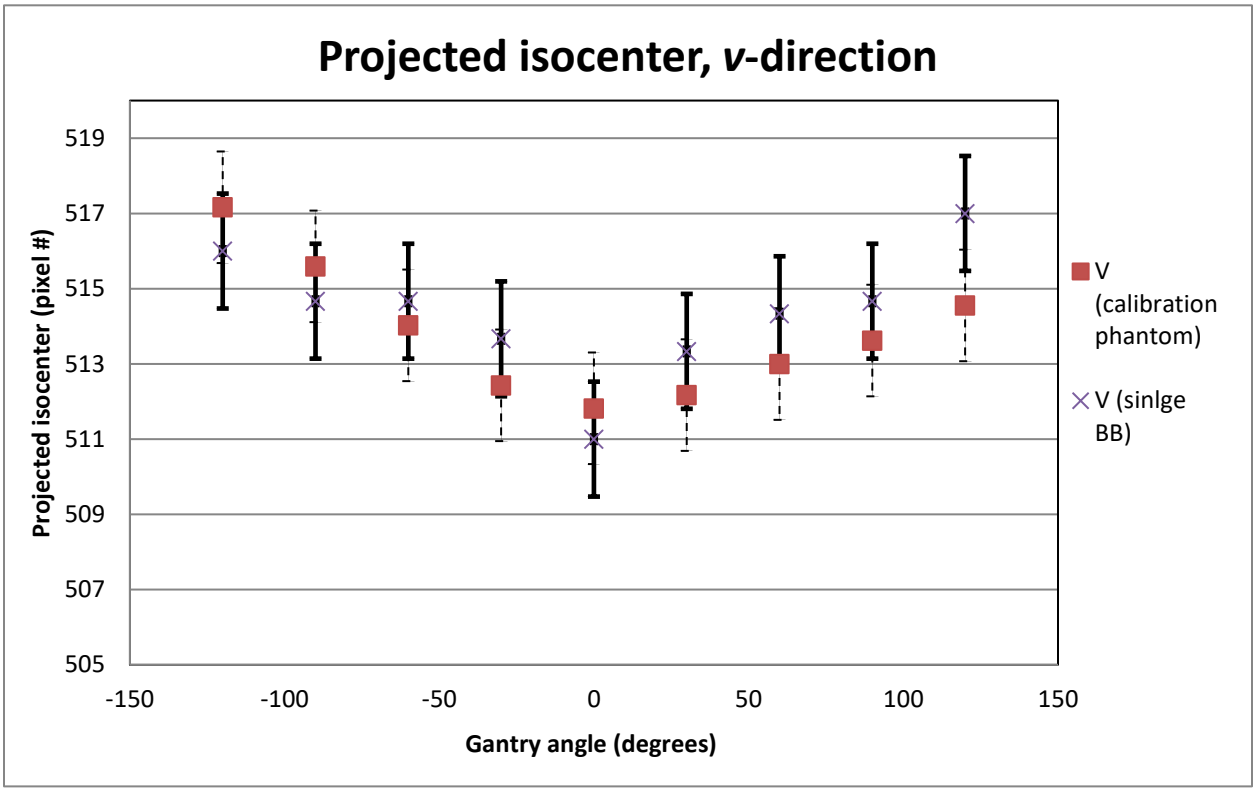

Figure 4.17: The difference in projected isocenter (*v*-direction) determined with the calibration phantom and single BB method respectively.

There is only a small difference in results obtained with these two methods. The maximum standard deviation between these methods is 1.80 (0.45 mm) in the *u*-direction and 1.73 (0.43 mm) in the *v*-direction. The reproducibility of both these methods is very good. Thus, either of these methods will yield accurate results in the determination of the projected isocenter location on the EPID.

4.2.2 Detector rotation angle, η

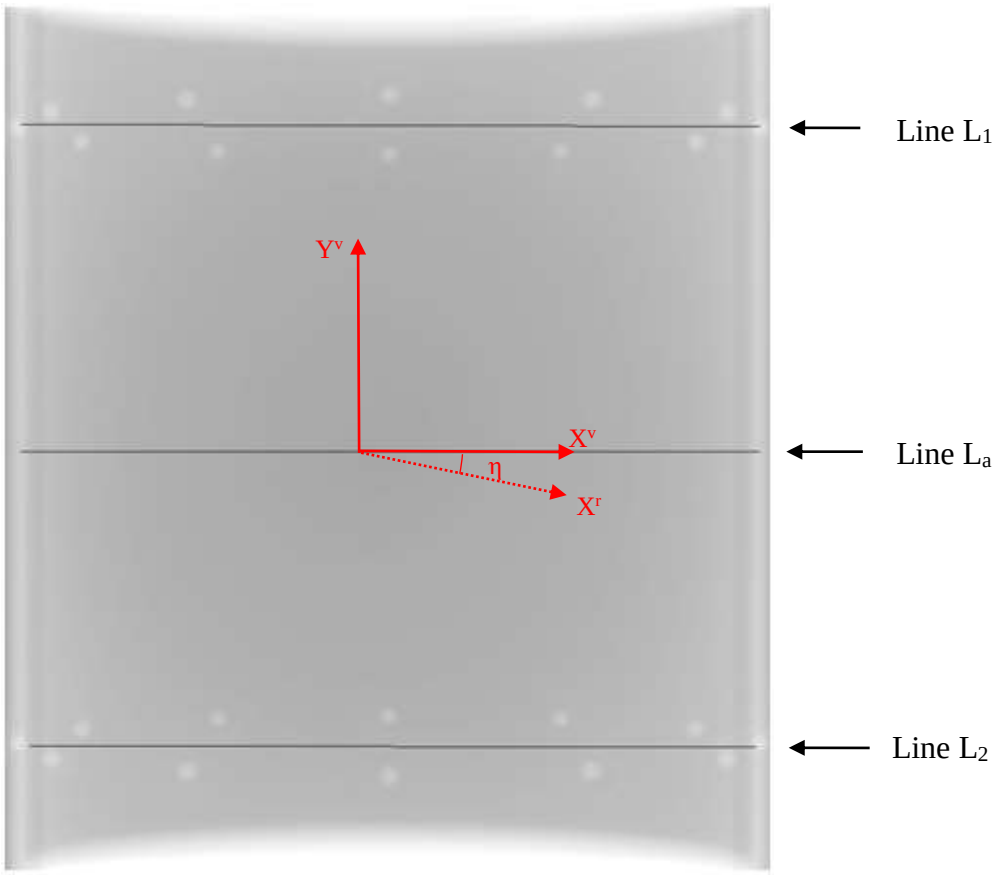

Figure 4.18: Illustration of lines generated to determine the rotation angle of the detector. When the detector has a tilt angle, ∅, of zero around the Y^v axis lines L_1 and L_2 will be parallel to line L_a. However, when the detector tilt angle ∅ is nonzero line L_a will be parallel to the X^r axis. Therefore, the angle between line L_a and the X^v axis will yield the rotation of the detector with respect to its normal axis (rotation angle, η). See section 3.2.3.

Line L_a is always parallel to X^r (x-axis of real detector plane). When the detector tilt angle, ∅, is zero line L_a will be parallel to lines L1 and L2 which is parallel to X^v (x-axis of virtual detector plane). However, when the detector tilt angle, ∅, is nonzero line L_a will be parallel to X^r. Thus, by calculating the angle between lines L_a and the X^v (or lines L1 and L2 and axis X^r respectively) using equation 3.2 the detector angle or rotation angle, η was determined. The variation with gantry angle is illustrated in Figure 4.19.

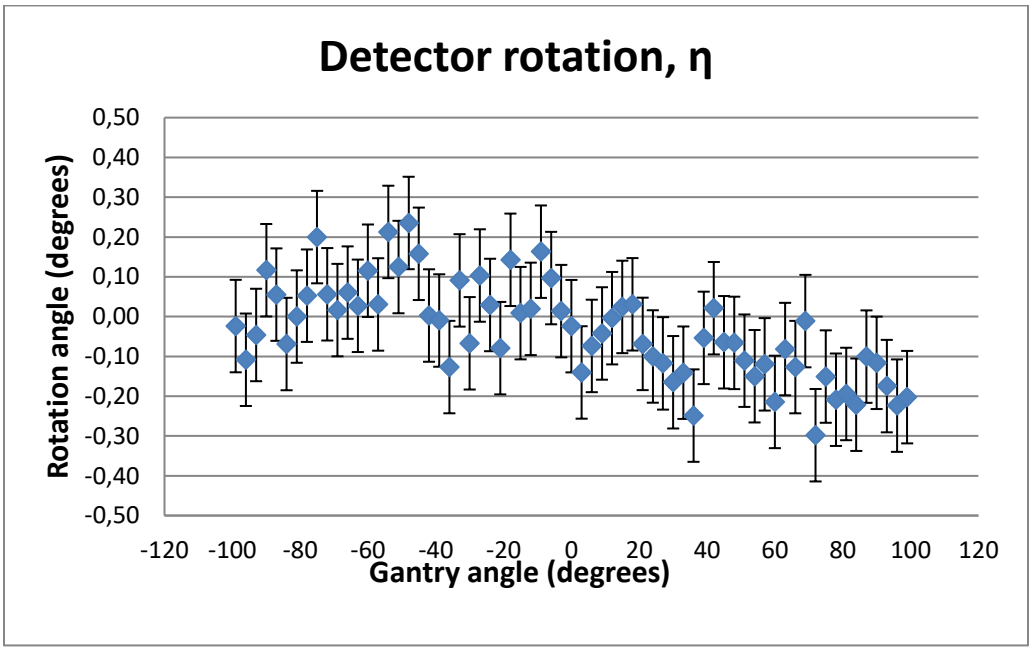

Figure 4.19: Detector rotation, η, as a function of gantry angle for the 200° arc used for image acquisition.

From the Figure 4.19 it can be seen that the rotation of the detector around its normal axis over the 200° arc is very small. The maximum rotation is 0.24° with a standard deviation of 0.21. Omitting to correct for detector rotation could have a severe influence on the reconstructed image, but when the rotation angle is small, as is the case here, the weighted and filtered projections corrected for rotation would not differ much from the weighted projections without rotation.

Figure 4.20 illustrates the reconstructed image (a) with and (b) without the rotation correction. Visually there is no significant difference between these images. Although these rotation angles are very small, projection images were rotated by angle η (corresponding to rotation for each gantry angle) before backprojection. Therefore, for the remainder of the calibration procedure the detector rotation angle, η, has been estimated and corrected for.

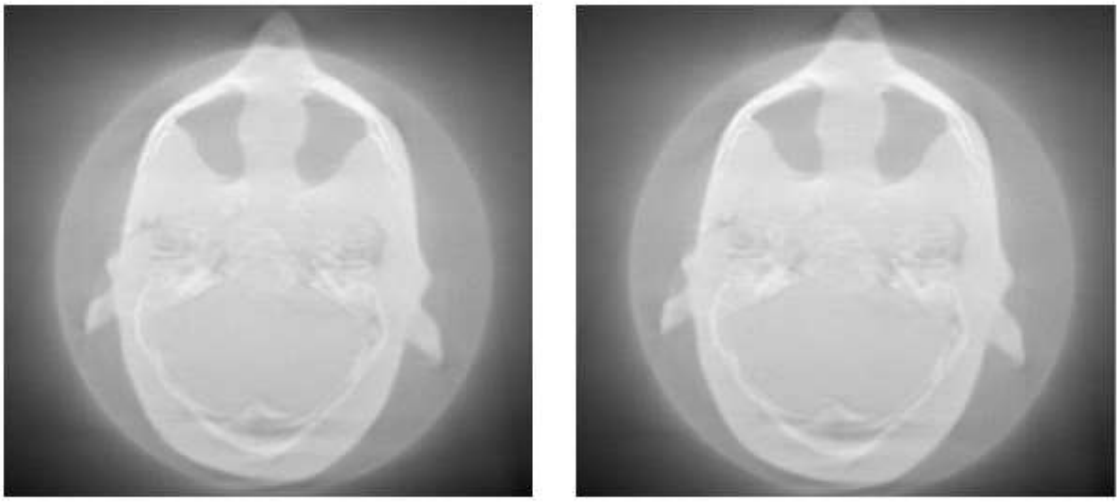

(a) (b)

Figure 4.20: The reconstructed image with (a) and without (b) the correction for detector rotation. Visually the difference in these images is insignificant.

4.2.3 Detector tilt angles, θ and ϕ

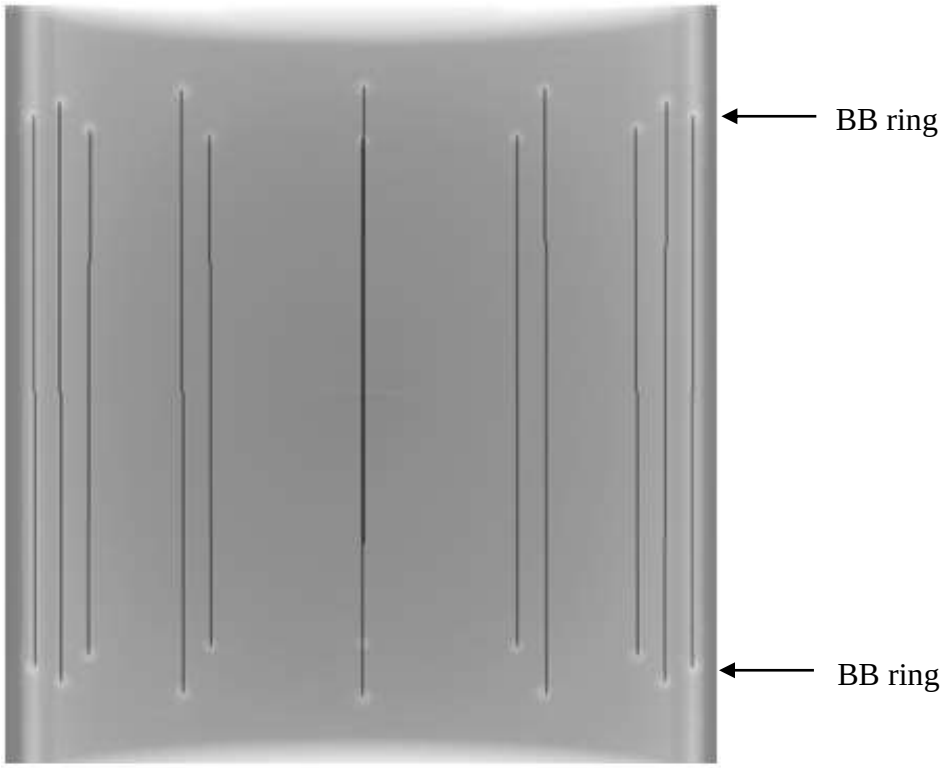

Figure 4.21: Lines generated to connect opposing pairs of BBs for determination of the detector tilt angles ϕ and θ. These lines converge to one point $P_\theta = (\alpha_\theta/\beta_\theta)$, due to the detector angle, θ. The detector angles ϕ and θ can be determined from equation 3.3.

Due to the detector angle, θ, the lines connecting opposing pairs of BBs converge to one point, the converging point $P_\theta = (\alpha_\theta/\beta_\theta)$. Equation 3.3 and the ellipse model described by equations 2.16 and 2.17 was used to determine the detector angles ϕ and θ.

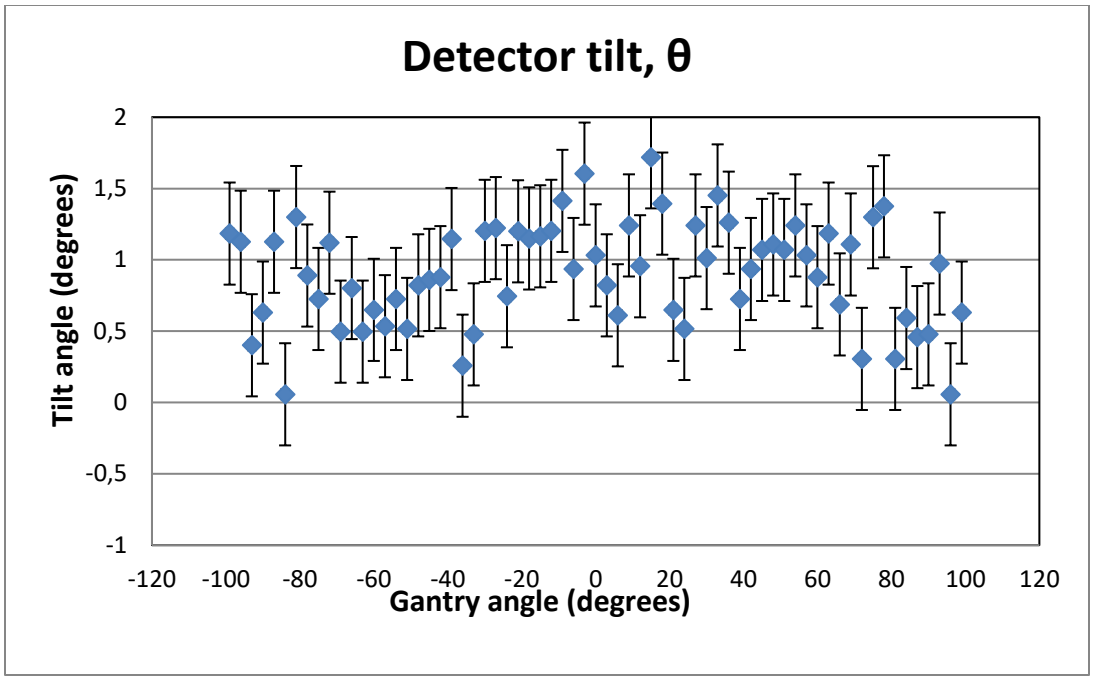

Figure 4.22: Results obtained for the detector (EPID) tilt, θ, around the central row.

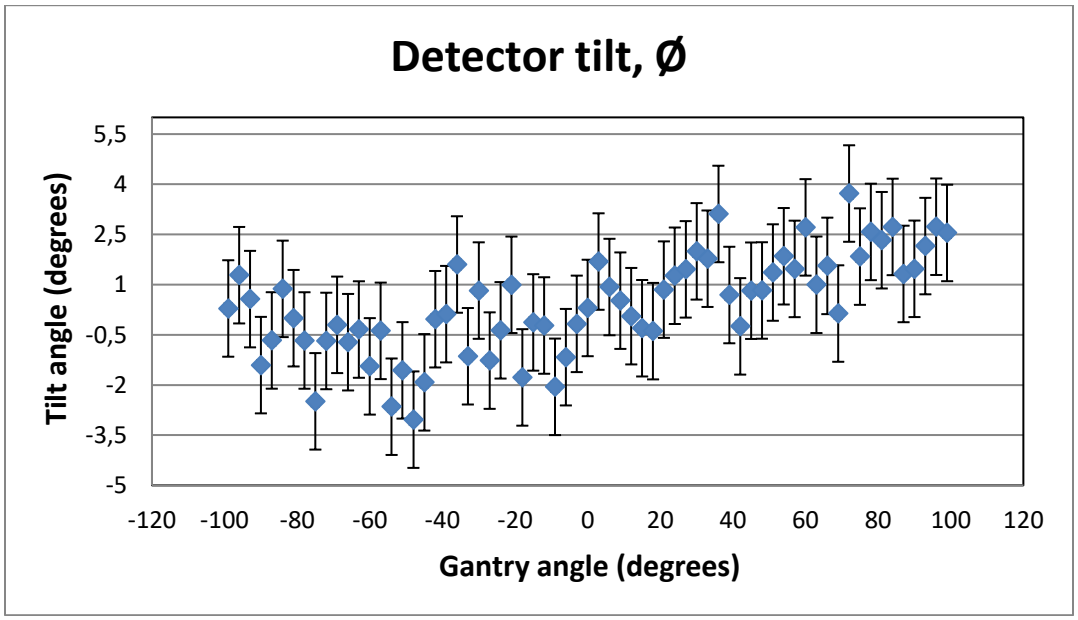

Figure 4.23: Results obtained for the detector (EPID) tilt, ϕ, around the central column.

Detector tilt angels are to some degree sensitive to the accurate positioning of the BBs in the phantom. The phantom was manufactured with sub-millimeter accuracy. Small errors during the manufacturing process or in the determination of BB positions on the 2D image might influence these parameters.

To test the influence of the determined BB position (on the 2D image) on the tilt angles one projection image was used and random planar shifts in the *y*-direction (horizontally) of up to 0.5mm, 1 mm and 2 mm in BB positions were simulated. These random shifts (trials) were repeated five times and the results were analyzed as shown in Table 4.4, Figure 4.24 and 4.25.

Table 4.4: The influence of BB position on the 2D image on tilt angles theta and phi.

	θ (degrees)			∅ (degrees)		
Trial #	0.5 mm	1 mm	2 mm	0.5 mm	1 mm	2 mm
1	-5.0	-3.5	-2.7	3.3	3.4	3.8
2	-2.9	-4.6	-3.7	3.7	3.5	4.0
3	-4.2	-5.8	-2.9	4.0	3.2	4.0
4	-3.4	-3.8	-3.5	3.8	3.7	3.7
5	-4.9	-2.5	-4.2	3.8	4.5	2.7
Average	-4.1	-4.1	-3.4	3.7	3.6	3.6
STDEV	0.9	1.2	0.6	0.3	0.5	0.5

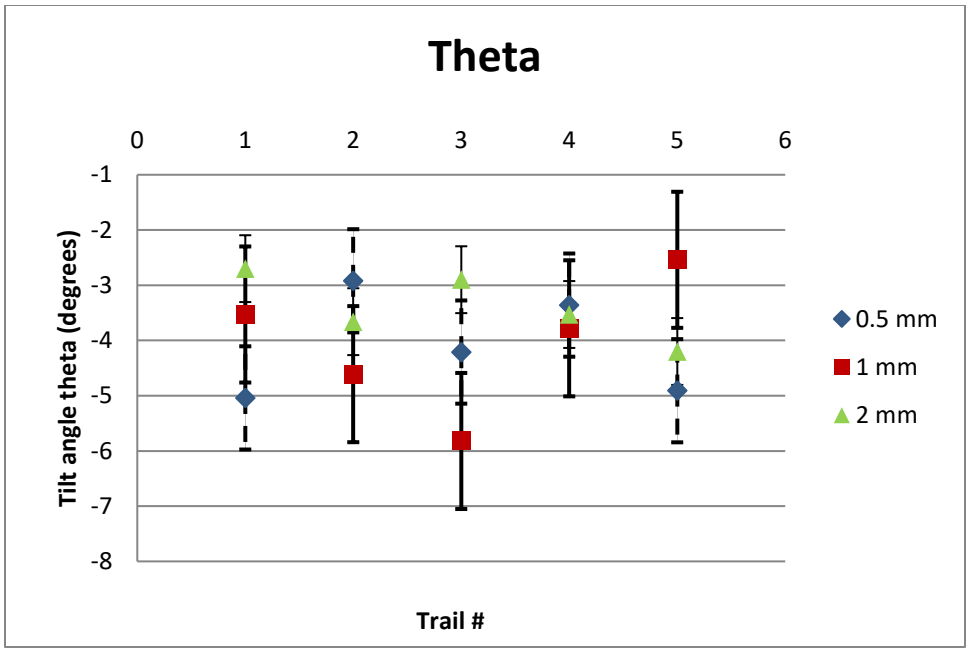

Figure 4.24: The influence of BB position on the 2D image on tilt angle theta.

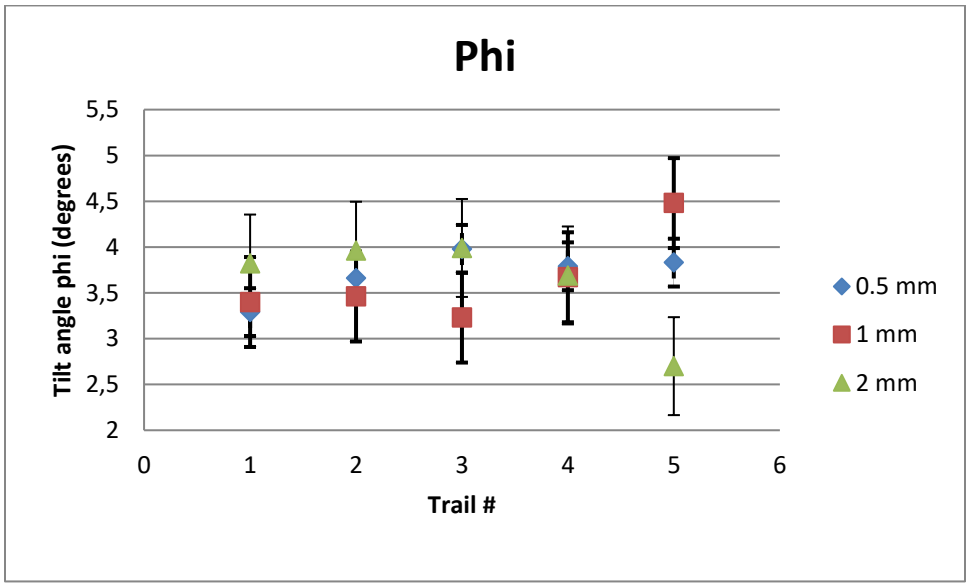

Figure 4.25: The influence of BB position on the 2D image on tilt angle phi.

From the results obtained it can be seen that the influence is more considerable on theta than phi. The statistical influence of planar shifts up to 2 mm on detector angles $\emptyset$ and θ is insignificant as shown in table 4.4. These shifts would not yield any artifacts when reconstructed images are visually inspected.

In the literature a study was conducted comparing reconstructed transversal images corrected for piercing point (isocenter (u, v)), detector angle (η) and detector tilt angles (ϕ and θ) with reconstructed images corrected only for piercing point and detector angle, η, omitting detector tilt angle correction. [25] The results showed that detector tilt angles have a negligible influence on the reconstructed images and images only corrected for piercing point and detector rotation angle, η does not look qualitatively worse than images corrected for all three above mentioned parameters. Therefore in this study the geometric corrections were restricted to piercing point and detector rotation angle, η. Tilt angles were omitted due to the fact that this will reduce the overall accuracy of the geometric calibration method.

4.2.4 Gantry angle variation

The gantry angle used in the reconstruction algorithm was obtained from the readout of the Elekta desktop and not the set gantry angle. Variation between these values is illustrated in Figure 4.26.

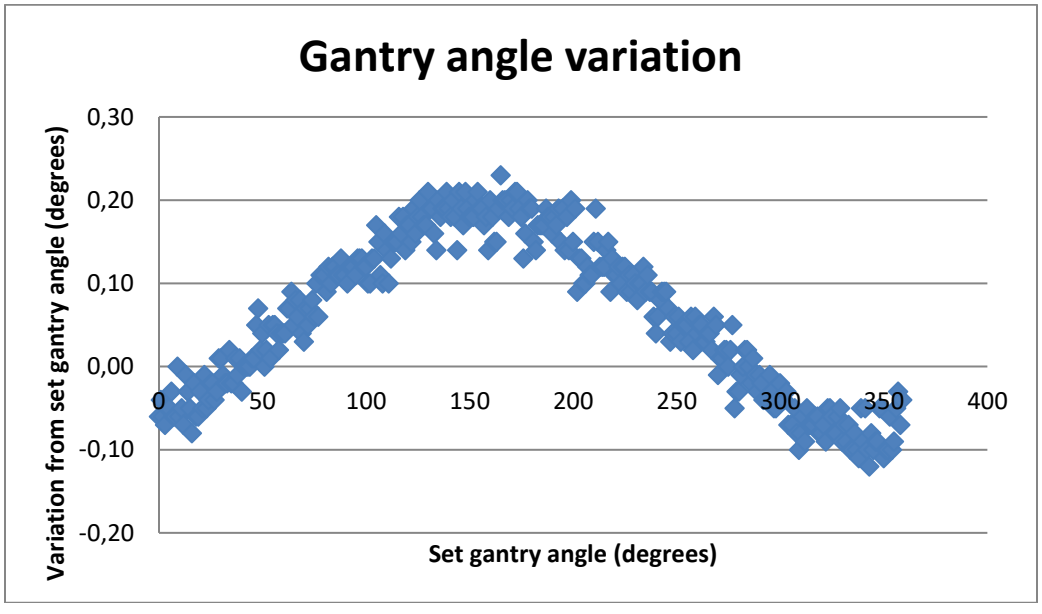

Figure 4.26: Results obtained for gantry angle variation with rotation through 360°.

Figure 4.26 shows the variation in set gantry angle vs. true gantry angle for rotation through 360°. The biggest variation from the set gantry angle was 0.23° and the standard deviation over the full rotation was 0.10. The variation in set gantry angle was accounted for in the reconstruction process to ensure that data were backprojected from the true gantry angle position.

Table 4.5 Summary of geometric misalignment corrections used in the reconstruction algorithm.

Geometric misalignment corrections	
Piercing point (projected isocenter):	
• **Single BB method**	Mean (*u)* pixel location: 513 ± 1.9 Mean (*v)* pixel location: 515 ± 2.2 Max deviation: *u*-direction: 4.5 pixels (1.1 mm) *v*-direction: 4.2 pixels (1.1 mm)
• **Calibration phantom**	Mean (*u)* pixel location: 514 ± 1.3 Mean (*v)* pixel location: 513 ± 1.5 Max deviation: *u*-direction: 3.0 pixels (0.8 mm) *v*-direction: 4.2 pixels (1.1 mm)
Detector rotation, η	Maximum rotation: 0.24 ° STDEV: 0.21
Gantry angle variation	Maximum deviation: 0.23° STDEV: 0.10

4.3 Image quality

The process of patient setup verification involves the registration of reconstructed CBCT images to CT images from treatment planning. Therefore, the accurate setup verification of patients on the treatment couch largely depends on images available for comparison. The quality of these images needs to be sufficient in order to achieve an optimal result during patient setup verification.

4.3.1 Uniformity and noise

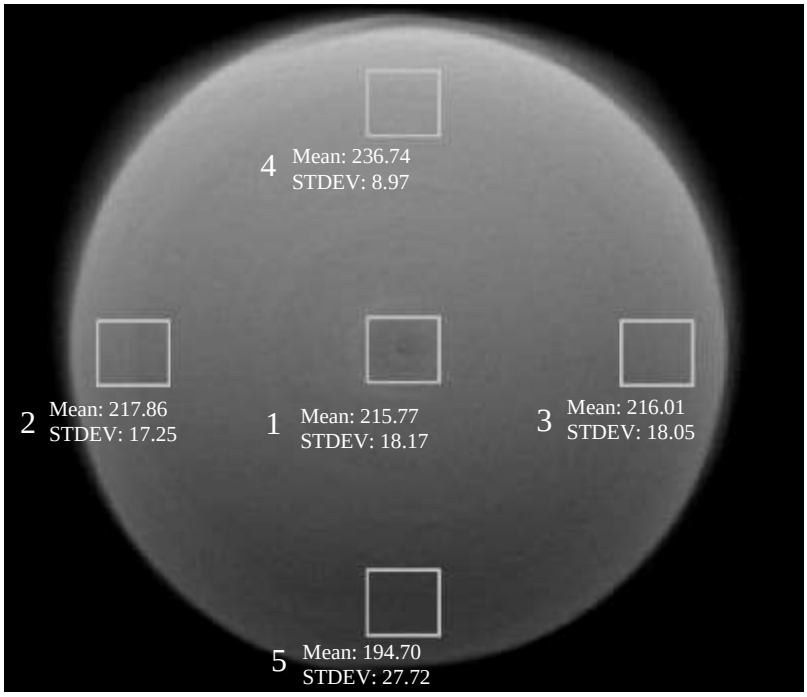

Figure 4.27: Reconstructed image obtained for the uniform part of the phantom for evaluation of uniformity and noise.

Table 4.6: Summary of results obtained for uniformity and noise measurements.

ROI	Mean	STDEV(σ)
1	215.77	18.17
2	217.86	17.25
3	216.01	18.05
4	236.74	8.97
5	194.70	27.72
Average	216.22	18.03
Max	236.74	27.72
Min	194.70	8.97

The integral non-uniformity (equation 3.5) was used to evaluate the uniformity in the reconstructed image. The maximum and minimum mean values were 236.74 and 194.70 respectively.

$$Integral\ nonuniformity = \frac{236.74 - 194.70}{236.74 + 194.70} = 0.097$$

The integral non-uniformity of the image is 9.7% which is poor compared to the non-uniformity of 0.37 % of the conventional CT scanner used in our department. This non-uniformity is largely due to the variation in mean values in the vertical direction of the image. The large variation in this direction is due to the attenuation of the beam. This variation can be rectified by either applying an attenuation correction or acquiring the projection over the entire 360°. A parker weighting factor which accounts for redundant data due to the use of a shorter scanning trajectory (200° instead of 360°) would also improve the uniformity of the reconstructed images. These techniques are beyond the scope of this study and were therefore not include. The integral non-uniformity in the horizontal direction is 0.43% which is more comparable to that of the

conventional CT scanner. The variation in uniformity for the vertical and horizontal directions of the reconstructed image is shown in Figure 4.28.

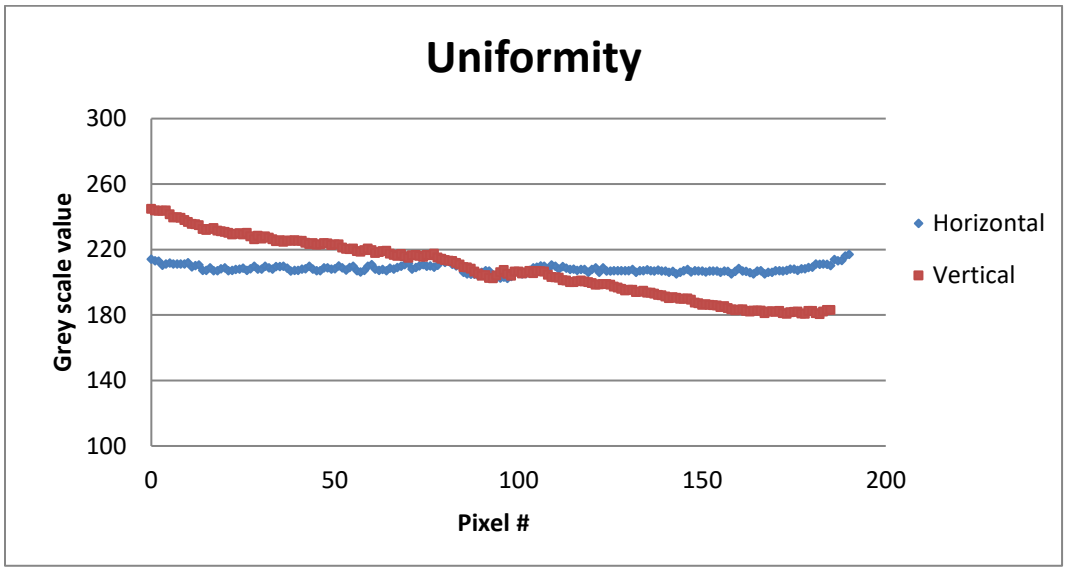

Figure 4.28: Uniformity obtained from a plot of all pixels along centered vertical and horizontal lines.

The level of noise was evaluated inspection of the SNR (see equation 3.6). The average mean and standard deviation values of the pixels in all 5 ROIs were used to determine this ratio:

$$SNR = \frac{216.22}{18.03} = 11.99$$

The desirable result is to maximize the signal and minimize the noise therefore; the SNR should be very high. A value of 11.99 is thus not optimal. In Figure 4.28 the SNR for region 4 is 26.39 compared to 7.02 for region 5, almost four times more. This can be attributed to the attenuation of the beam. The SNR in this area can be improved by applying an attenuation correction factor

or acquiring the projections over the entire 360°. As mentioned previously implementation of these techniques are beyond the scope of the study and were not included.

4.3.2 Spatial resolution

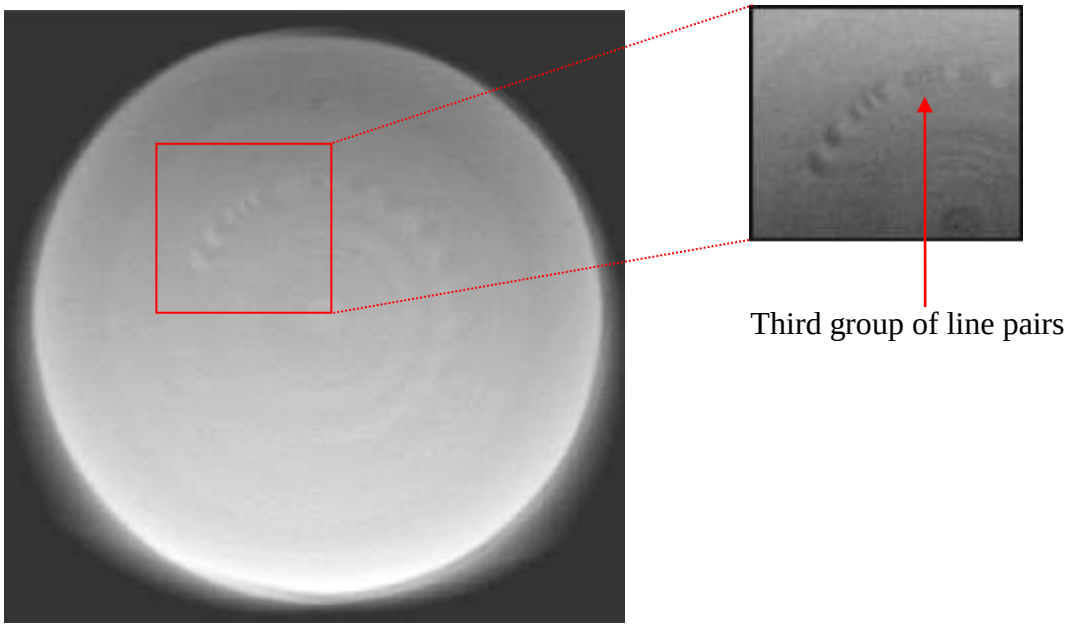

Figure 4.29: Reconstructed image obtained for the high resolution module with 21 line pair per cm gauge. The image was visually inspected to obtain the group of line pairs that can still be seen as separate bars (see insert).

Figure 4.29 shows a slice of the image quality phantom (Catphan) containing the high resolution module used for evaluation of spatial resolution. The bars in group three are still visible which corresponds to a gap size of 0.167 cm (see section 3.3.2) and 3 lp/cm. This result was obtained with the 200 MU protocol (160 cGy at isocenter) used in the reconstruction process (section 3.1). This resolution will be sufficient for registration of bony landmarks and small objects such as surgical clips or fiducial markers, but higher doses would be necessary to distinguish between soft tissues due to contrast degradation.

4.3.3 Contrast resolution

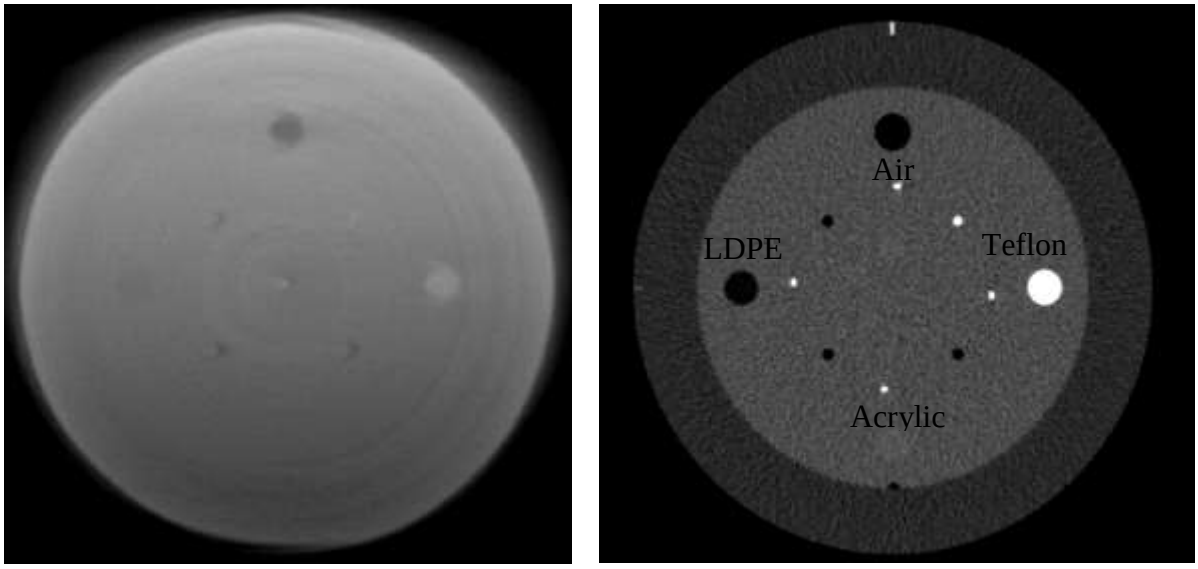

(a) (b)

Figure 4.30: The reconstructed images of the sensitometry module obtained with (a) a megavoltage beam and EPID and (b) a kilovoltage beam of a conventional CT scanner. These images were used for visual evaluation of the contrast resolution.

From Figure 4.30 the air and Teflon samples can clearly be distinguished on the megavoltage image (left). These two samples have the lowest and highest Hounsfield numbers, -1000 H and 990 H respectively. The LDPE (-100 H) sample can be seen vaguely on the left-hand image, but the acrylic sample (120 H) cannot be seen at all.

The contrast of the megavoltage image would therefore be sufficient to visualize objects with high electron density differences such as bone and air cavities. Soft tissue visualization (objects with small electron density differences) would be unfeasible.

The reconstructed megavoltage images can thus be used for patient positioning in situations where fiducial markers, which would clearly be seen on these images, are implanted in the patient. Due to unsatisfactory soft tissue visualization these images should and could not be used for treatment planning or contouring purposes.

4.3.4 Image artifacts

Image artifacts degrade the overall image quality of an image. Displayed below are some of the artifacts visible on the reconstructed images of the image quality phantom (Figure 4.31) Rando head phantom (Figure 4.32).

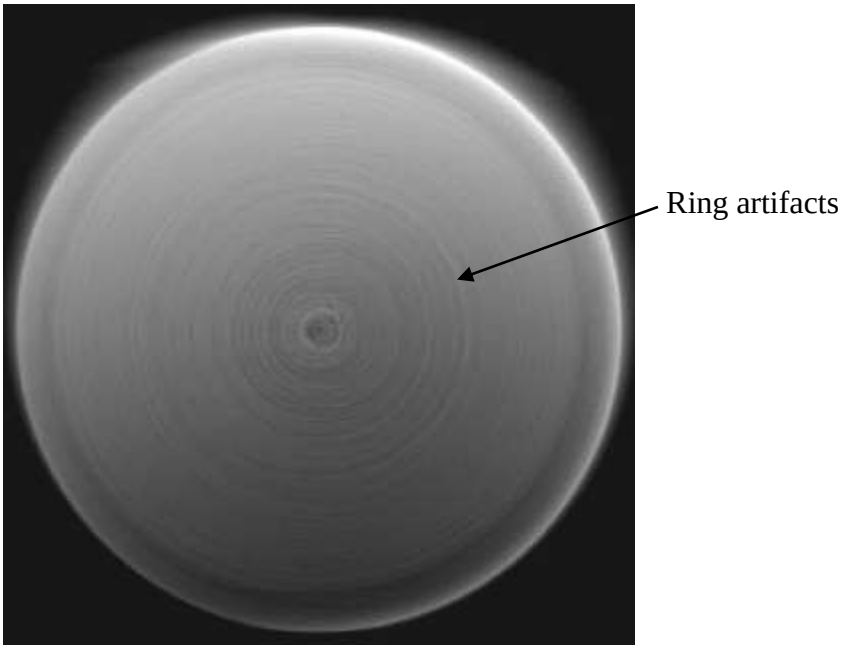

Figure 4.31: Ring artifacts visible on a reconstructed axial slice. These light and dark bands are caused by differences in pixel response in the EPID.

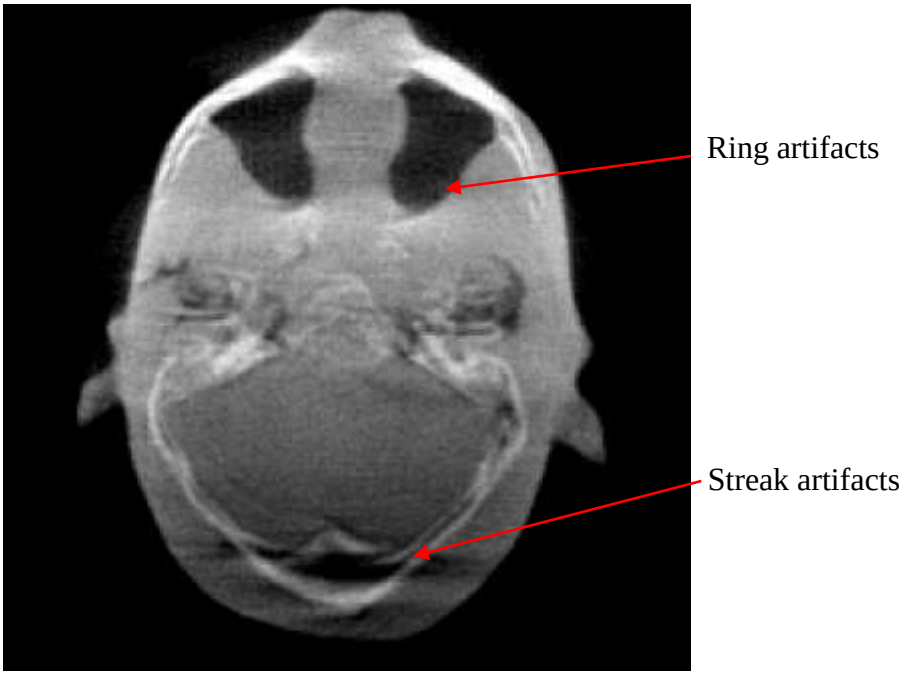

Figure 4.32: A reconstructed axial slice of the Rando head phantom. Ring artifacts as well as streak artifacts can clearly be seen on this image.

Ring artifacts are visible on both examples (Figure 4.31 and 4.32). Although these rings are clearly visible in a uniform phantom (Figure 4.31) these rings are less pronounced on the clinical image (Figure 4.32). As mentioned in sec 2.3.8 ring artifacts would rarely interfere with clinical decision but it most definitely will reduce the diagnostic quality of images. Ring artifacts can be reduced or corrected for by recalibration of the detector gain.

Streak artifacts are visible in Figure 4.32. This artifact occurs in the bony regions of the head phantom due to beam hardening as explained in section 2.3.8. These artifacts can be reduced by adding filtration (a piece of attenuating material) to reduce the low energy component of the beam and pre-harden the beam before it enters the phantom or patient. Corrections for beam hardening can also be incorporated in the reconstruction software. Implementation of corrections to reduce or rectify artifacts was beyond the scope of this study and therefore not included.

4.4 Dose measurement

4.4.1 Ionization chamber measurements

The linearity of the linac output for the lower range MUs were checked before dose measurements were made to ensure a constant beam output (1 MU = 1 cGy) over the 200° arc.

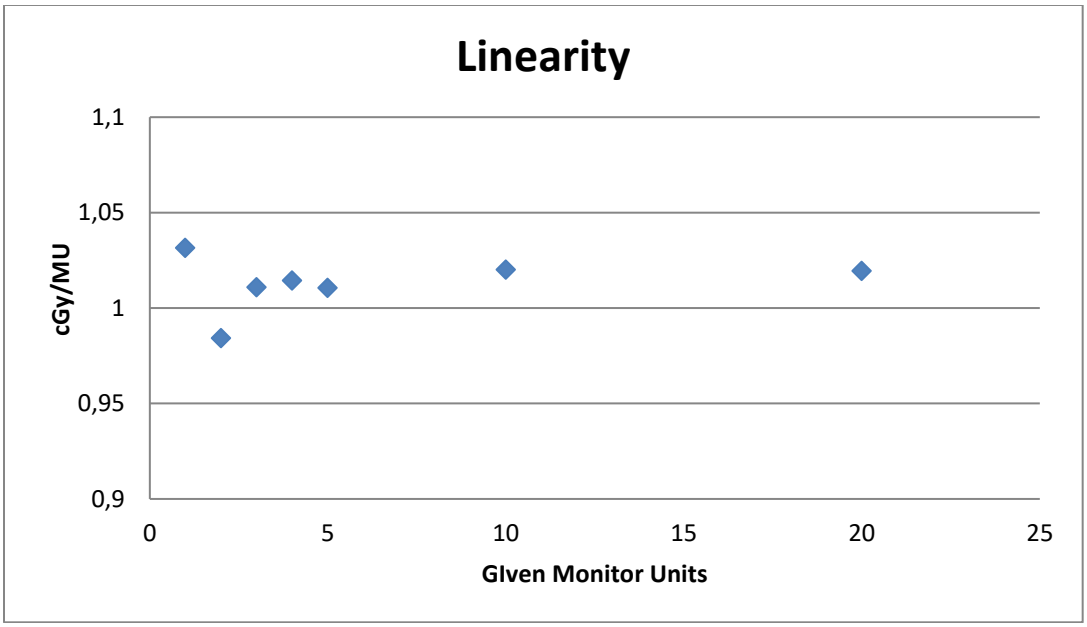

Figure 4.33: The linearity of the linac for the lower range of MUs.

The largest deviation in beam output is 0.3%. From the results obtained (Figure 4.33) it can be concluded that the linac is linear in the lower range of MUs and the dose measured would be within 0.3% of the 'true' dose delivered at the point of measurement.

The ionization chamber-electrometer measurement for the 200° arc was repeated three times. The average of these measurements was used to determine the dose at the central part of the phantom (isocenter), see Figure 3.16. Results are displayed in Table 4.7.

Table 4.7: Results for ionization chamber measurements to determine the dose at the isocenter.

Measurement no.	Ionisation (nC)
1	25.25
2	25.25
3	25.17
Average	25.22
$N_{d,w}$ (mGy/displayed nC)	53.43
Temp (°C)	21
Pressure (mBar)	856
Dose (cGy)	**160.01±0.04**

4.4.2 Film measurements

The films obtained for dose measurements were converted to digital format by using a Vidar film scanner ®. An in-house developed IDL-base code was then used to analyze the film obtained during the 200° image acquisition arc.

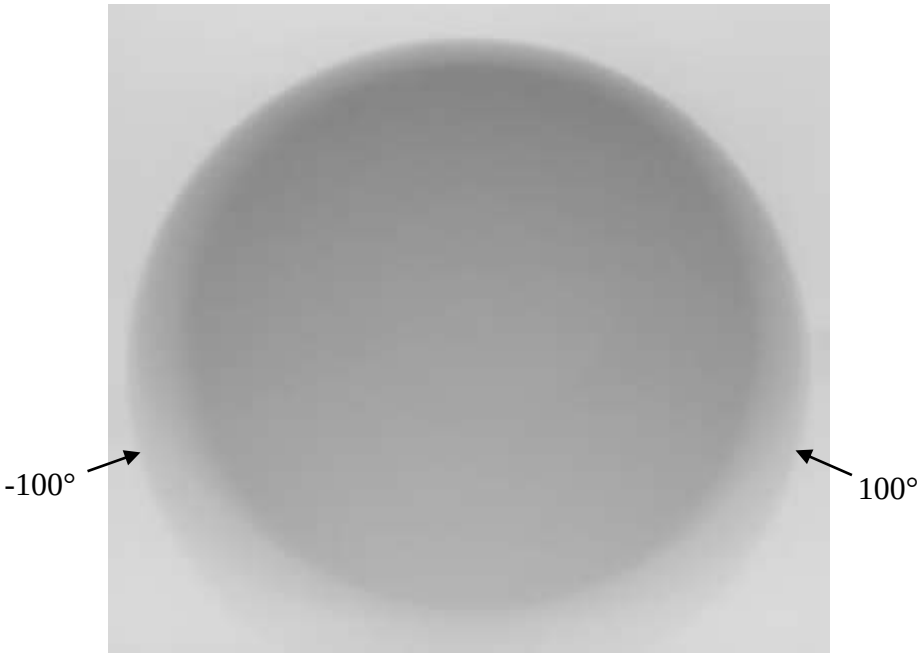

Figure 4.34: The film obtained after exposing it to a 200° arc from -100° to 100 ° gantry angle at one degree intervals.

Films were used to determine a calibration curve for the conversion of optical density to dose. A calibration film was irradiated using a set of 10 x 10 cm^2 fields, each field representing a certain amount of MUs (ranging from 0 to 210 in intervals of 15 MUs). A region of interest (ROI) drawn in on the central part of each field represented the optical density for the corresponding amount of MUs given (Figure 4.35).

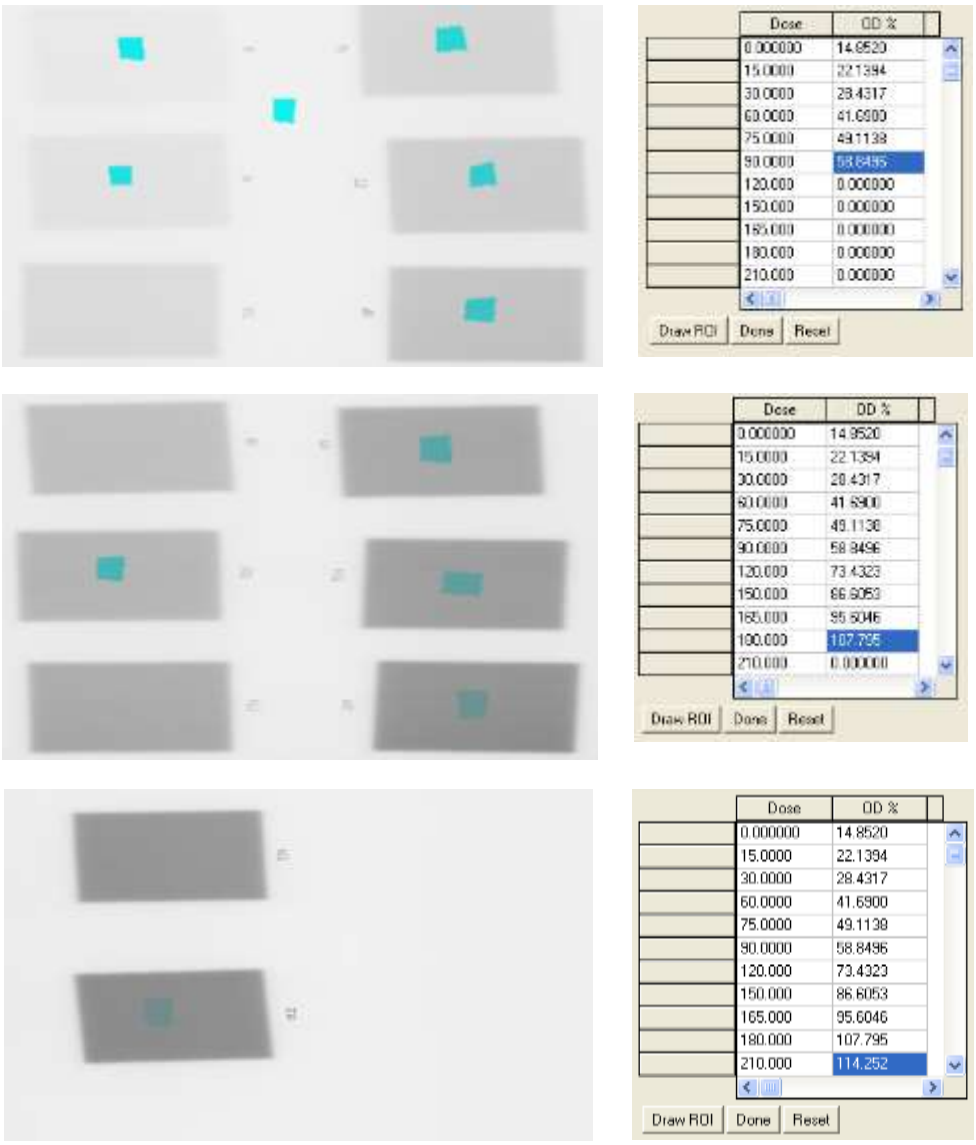

Figure 4.35: The calibration films obtained to generate a calibration curve for the conversion of optical density to dose. ROIs are shown as green on the film.

The best fit through all the data points is obtained (Figure 4.36). This curve is used for subsequent analysis of the film.

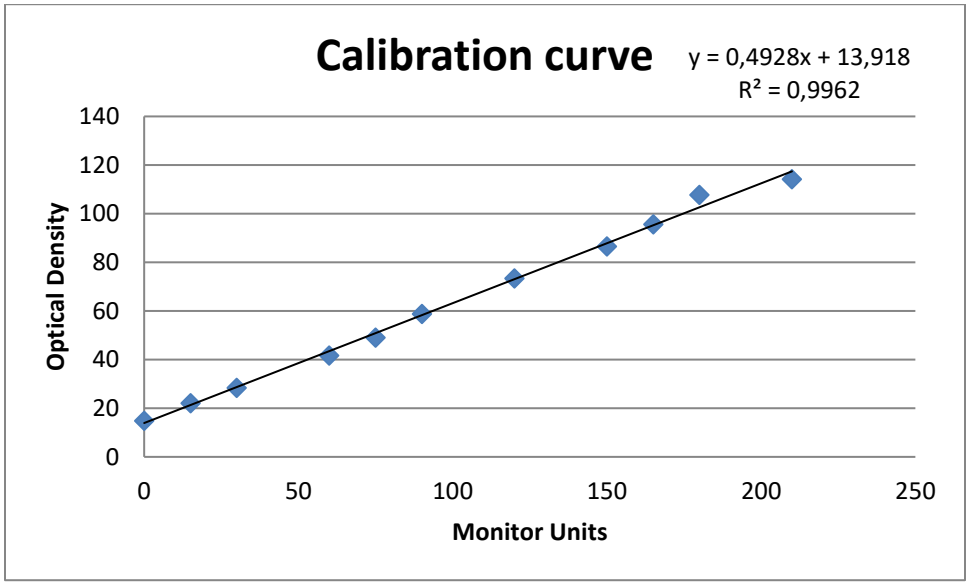

Figure 4.36: Calibration curve for conversion of optical density to dose.

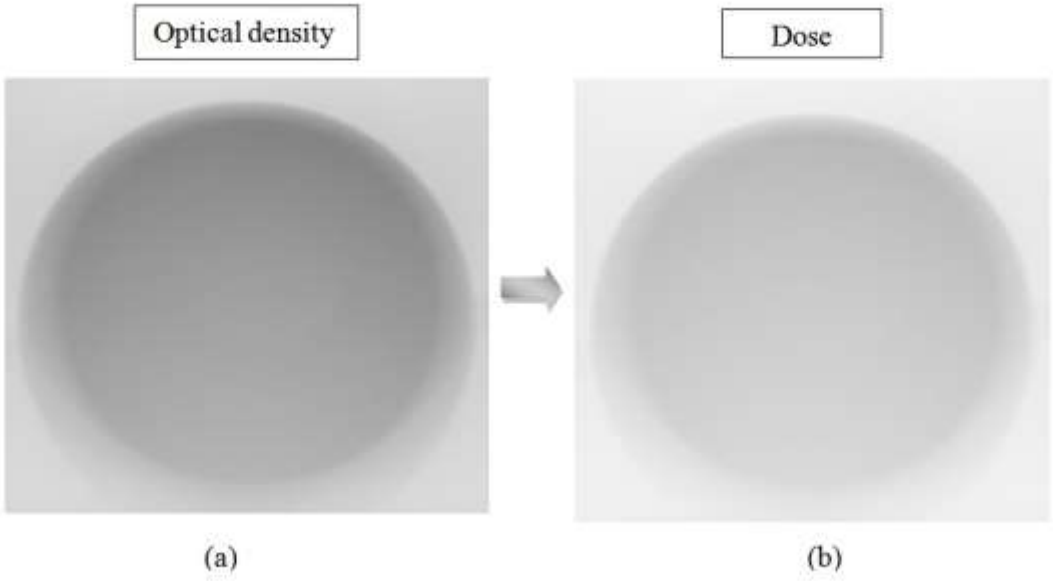

Figure 4.37: The film representing the dose received in terms of (a) optical density values is converted to (b) dose values by using the calibration curve obtained.

To compare ionization chamber and film results the dose on the film at the position of the ionization chamber (center of the phantom, see section 3.4) needs to be determined. The dose at any point on the film coordinate system can be obtained by positioning the cursor at any point of interest. The *x* and *y* coordinates of the ionization chamber position (in terms of the film coordinate system) is (401, 290). The dose at that point is 159 cGy (Figure 4.38).

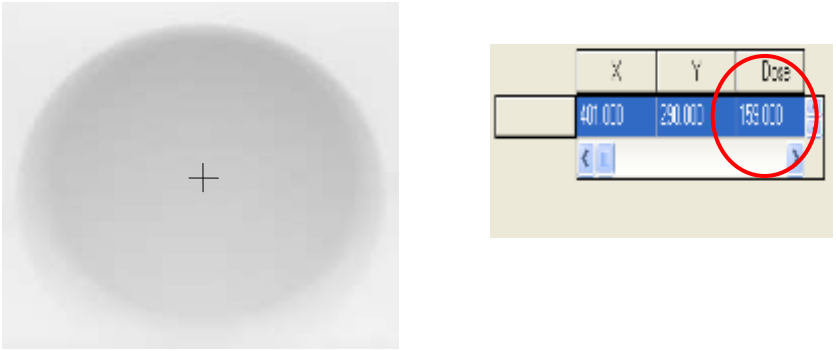

Figure 4.38: The dose at any film coordinate position can be obtained by positioning the cursor at any pointof interest.

The plot of the profile through the center of the phantom confirms the results obtained in Figure 4.38. The dose at the periphery of the phantom are in the order of 180 cGy decreasing to 160 cGy in the center of the phantom (Figure 4.39).

There is a definite decrease in dose in the vertical direction of the phantom. The dose varies from 230 cGy at the top to 130 cGy at the bottom of the phantom (Figure 4.39). This can be attributed to the geometry of the 200° arc. There is an overlap of projections in the top part of the phantom, while the bottom part (from 100° to 260°) does not have any projections overlapping.

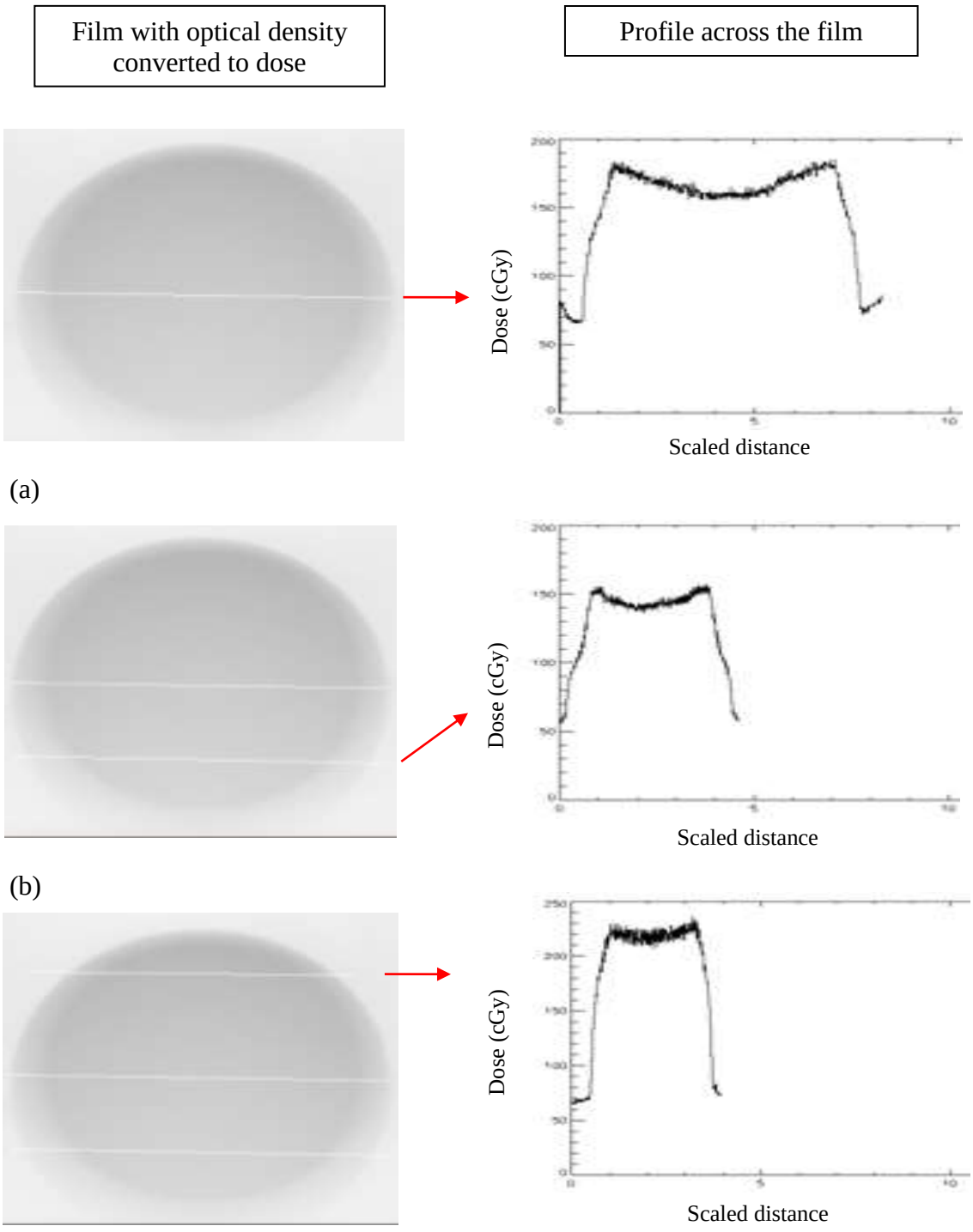

Figure 4.39: Profiles plotted on the film (optical density converted to dose) showing the dose distribution at (a) the center, (b) the bottom, and (c) the top part of the phantom for the entire 200° arc.

4.4.3 Treatment planning system

Figure 4.40 illustrates the dose distribution for the treatment plan computed for the image acquisition technique used in this study. The reference point was set to be at the position of the ionization chamber during measurements (this point marks the isocenter and is also used as the normalization point). The dose at the reference point is 158.9 cGy. The effect of the arc geometry (as discussed in 4.4.2) is clearly demonstrated in the dose distribution. The high dose area is in the top part of the phantom and decreases as we move down in a vertical line through the phantom. The maximum dose is 232.1 cGy which corresponds with film measurements.

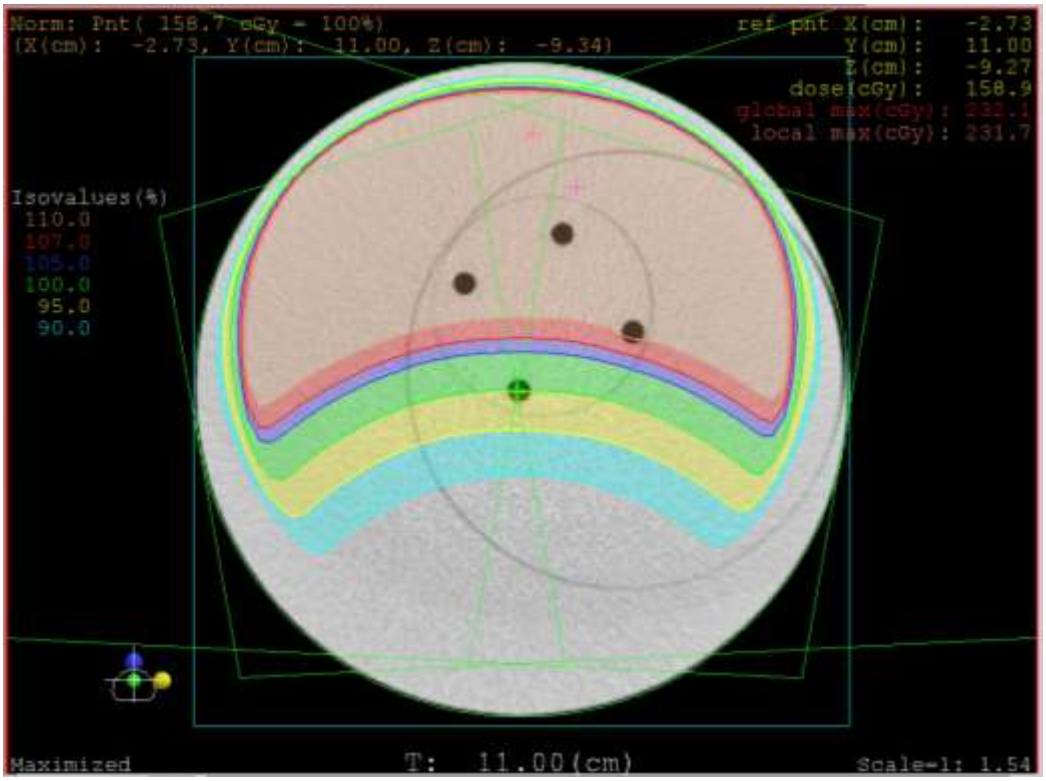

Fig 4.40: A treatment plan computed for the image acquisition technique used in this study. An arc was used with the start point at -100° and end point at 100° gantry angle. An 8 MV beam was used delivering one MU per degree.

Table 4.8: Results obtained for dose measurements with an ionization chamber, film and treatment planning system.

	Dose at the isocenter position (cGy)
Ionization chamber	160.01
Film	159.00
Xio TPS	158.90
Average	159.30
Standard deviation	0.61

The dose measurements for the ionization chamber, film and TPS correspond well with each other. The average dose measured of the three modalities is 159.30 cGy with a standard deviation of 0.61 cGy.

In general doses received during image acquisition (prior to treatment) are incorporated in the prescribed dose. These doses are usually in the vicinity of 10 cGy.[3] A dose of 159.30 cGy is clearly too high and would be unacceptable for clinical use. Various options can be explored to reduce the dose such as fewer projections (see Figure 4.41) and using arc therapy mode instead of ‘step-and-shoot’, but all these methods might worsen the image quality to an unacceptable extent.

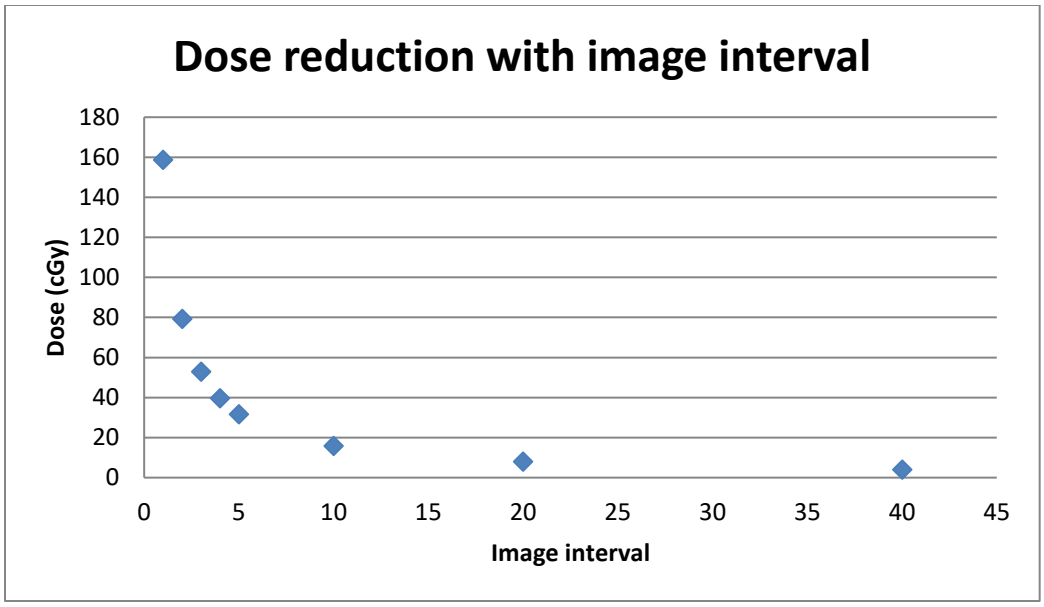

Figure 4.41: Illustrated here is the reduction in dose with increase in projection image interval during image acquisition for reconstruction.

As the interval between projection images acquired is increased (fewer projection images are used) the dose to the central part of the phantom will decrease noticeably (Figure 4.41). The dose can be reduced from 160 cGy to 15 cGy when the image interval is increased from one to ten. As mentioned previously the limiting factor however will be the level of image quality necessary to reach the outcome for which the images are needed (registration of bony anatomy for setup verification).

4.5 Positional accuracy

Shown in Figure 4.42 are the reconstructed transverse images of the two data sets with (a) the phantom more or less at isocenter and (b) the phantom in the same position but the treatment couch moved a known distance of 2 cm in lateral, longitudinal and anterior-posterior direction.

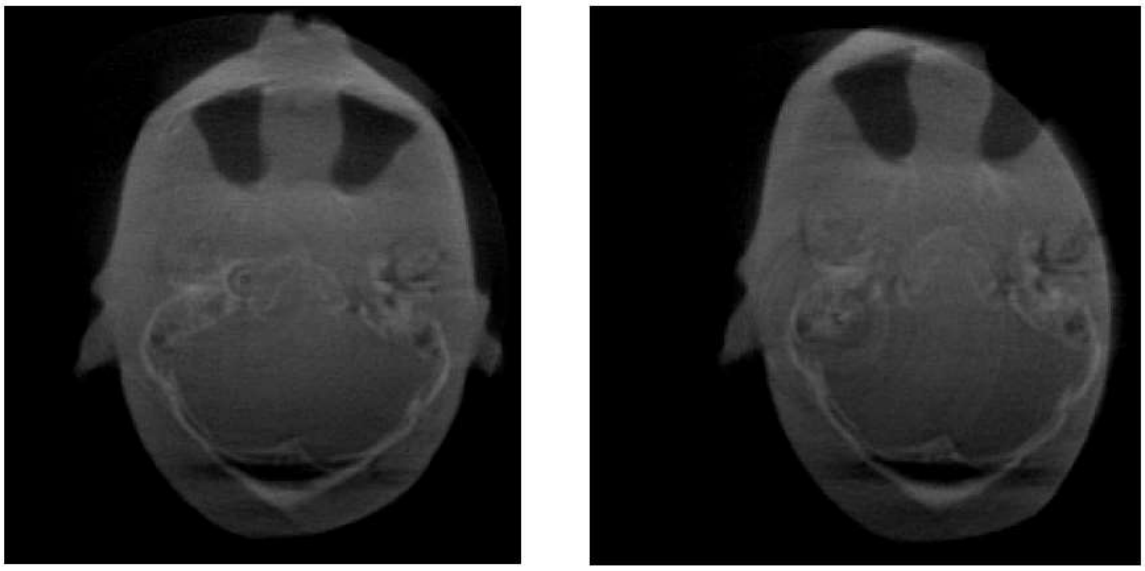

(a) (b)

Figure 4.42: To simulate a setup error, images of the Rando head phantom for two 200° arcs were acquired. The first arc (a) was acquired with the phantom setup more or less at isocenter. For the second arc (b) the treatment couch was moved 2 cm in the lateral, longitudinal and anterior directions without moving the phantom.

Due to a shift in the longitudinal direction the position in the reconstruction matrix of the corresponding reconstructed transverse slices will be different for the two data sets. The difference in slice position was determined by visually inspecting the reconstructed transverse images to find the corresponding slice in each data set.

The shift can be calculated using equation (3.5):

$$shift\ in\ longitudinal\ direction = (S_1 - S_2)pixel \times (sampling\ interval)\frac{cm}{pixel}$$

where S_1 and S_2 are the slice positions for data set one and two respectively. The sampling interval at the isocenter is 0.0976 cm/pixel.

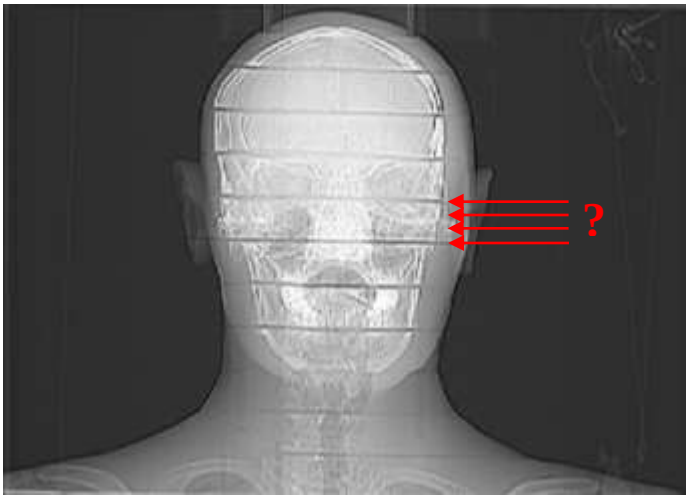

Figure 4.43: The longitudinal shift is calculated by determining the difference in slice position in the reconstructed matrix. Multiplying the difference in slice position by the known sampling interval yields the shift in the longitudinal direction.

$$shift\ in\ longitudinal\ direction = (128 - 108) pixels \times \frac{0.0976 cm}{pixel} = 1.95\ cm$$

The shift in the lateral and anterior-posterior direction was determined by choosing five corresponding points on each image (Figure 4.44). The shift / translation were determined by calculating the difference in coordinate position for equivalent points on the two images.

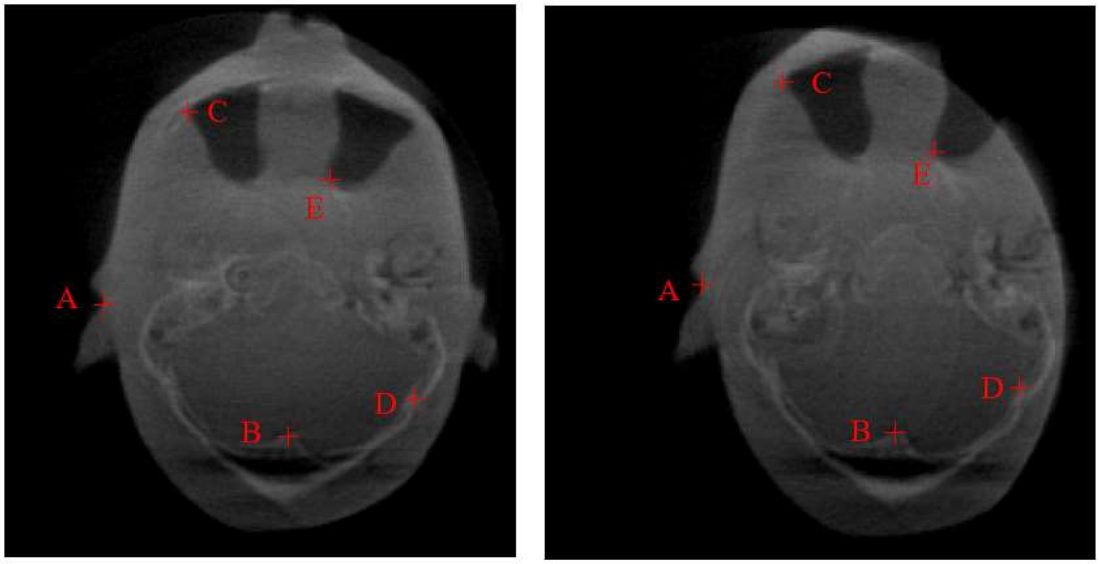

(a) (b)

Figure 4.44: Five points representing certain anatomical landmarks (similar for each image) were chosen on image (a) and (b). The difference in the position of corresponding points on each image yield simulated shift in the lateral and anterior-posterior directions.

Rotation was evaluated by simulating a rotation of five degrees. The method followed is basically the same as in the case of translation measurements. Five points were chosen on the original and rotated transversal images. With no translation the coordinates of the points on the two images can be matched performing a rotation.

The rotation necessary to match these points was calculated by using the coordinates of points A-E in Figure 4.44 and equation (3.6):

$$\cos\theta = \frac{a \cdot b}{|a||b|}$$

where *a* and *b* are vectors from the origin of the image (center of image at pixel address (0,0)) to the coordinates of point A on Figure 4.44 (a) and the corresponding point A on Figure 4.44 (b).

The angle θ between these two vectors represents the rotation angle (see Figure 4.45). This was repeated for all five points.

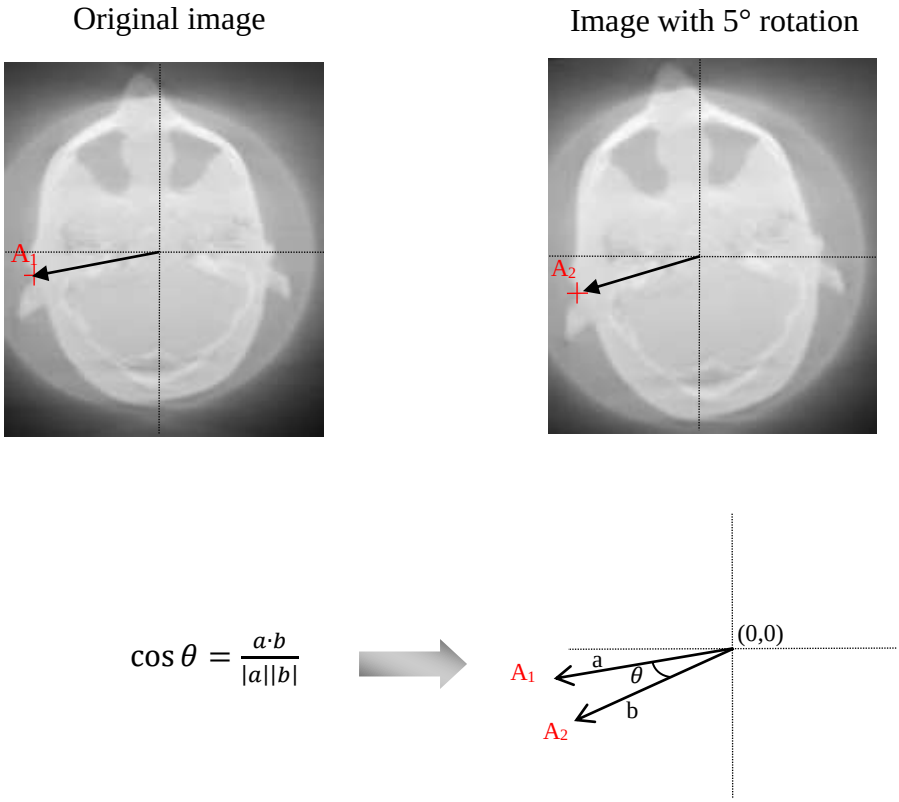

Figure 4.45: Rotation was determined by using the coordinate positions, (x,y), of two corresponding points on the original and rotated images. The rotation angle, , was calculated by using equation 4.2.

The measured shift and rotation was calculated for images reconstructed with 1°, 5°, 10° and 15° projection intervals. The intra- and inter observer dependency was evaluated and is illustrated in the subsequent graphs.

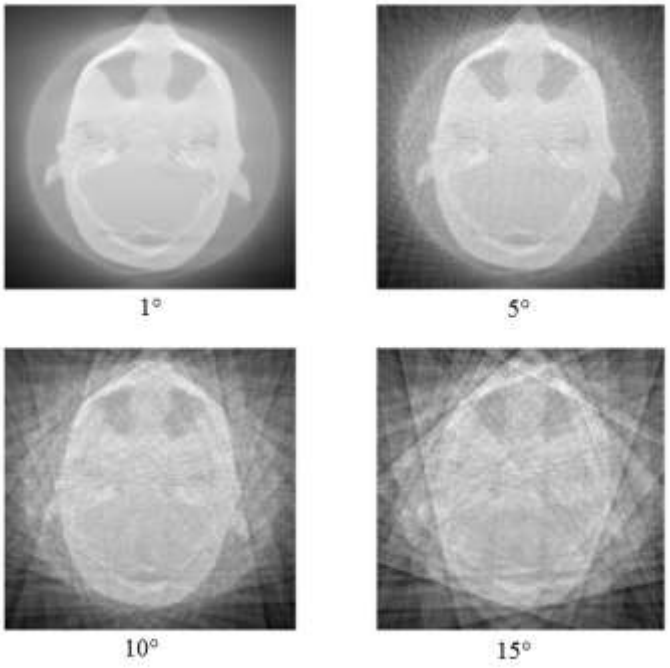

Figure 4.46: Reconstructed images obtained by using image intervals of 1°, 5°, 10° and 15°. Positional accuracy was evaluated on all these images.

4.5.1 Translation (shift)

The phantom was shifted a known distance of 2 cm in all directions. The expected shift in all directions should therefore be 2 cm. In Figure 4.47 the difference from the expected value (2 cm) are shown for each imaging interval used.

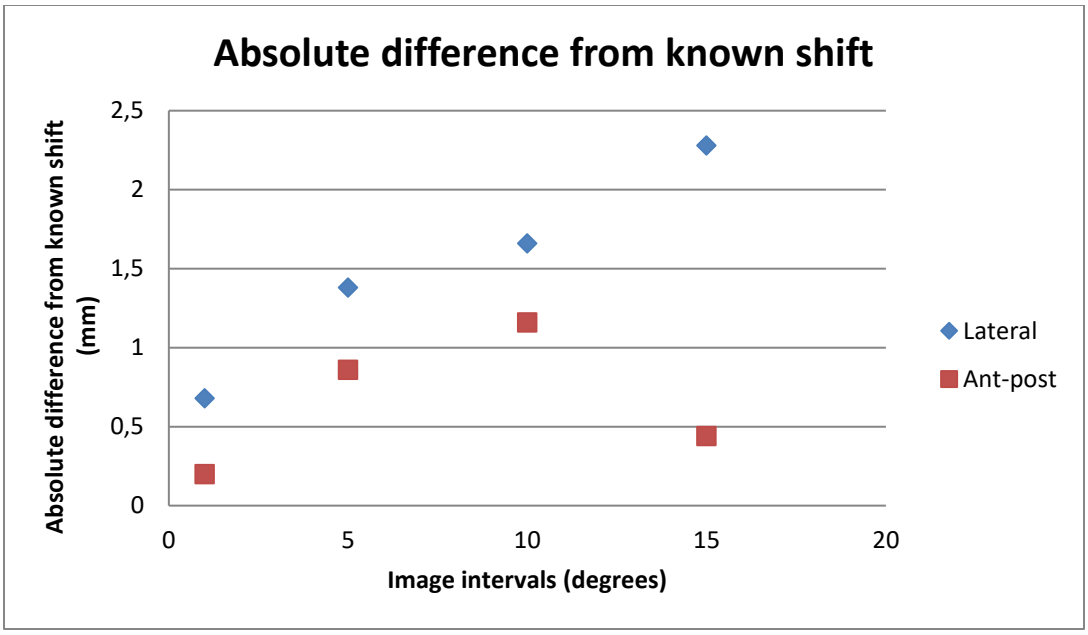

Figure 4.47: The absolute difference between the measured lateral and anterior-posterior shifts (based on intra-observer measurements) and the known shift of 2 cm.

The absolute difference in the lateral and anterior-posterior directions are all within 2 mm of the expected value for the first three imaging intervals (1°, 5° and 10°). In the lateral direction the difference is more than 2 mm for the 15° interval which is substandard from a clinical point of view.

Using imaging intervals of 10° and 15° may have several advantages such as a shorter imaging time and lower dose to the patient, but as can be seen from Figure 4.46 the image quality is very poor with reconstruction artifacts due the reduced number of projections used. When these images are used for evaluation of positional accuracy observers tend to use the artifacts rather than true anatomical features as reference point. This will yield false positive values as in the case of the anterior-posterior shift measured on the 15° interval image (see Figure 4.47).

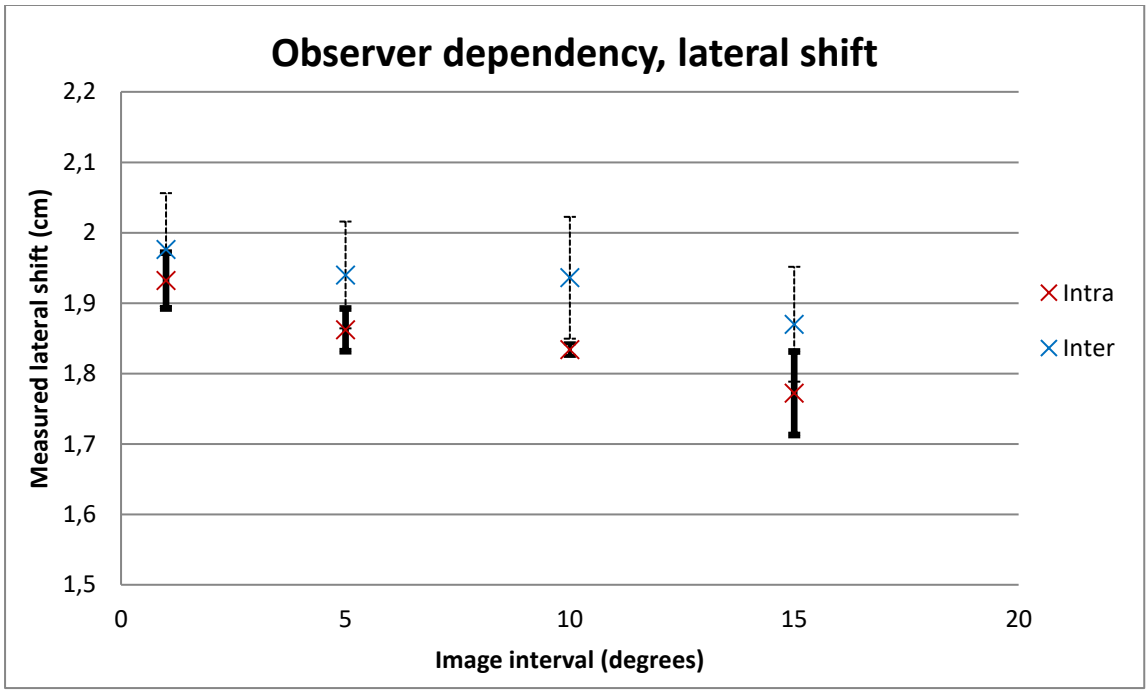

Figure 4.48: Observer dependency in determination of the lateral measured shift for various imaging intervals.

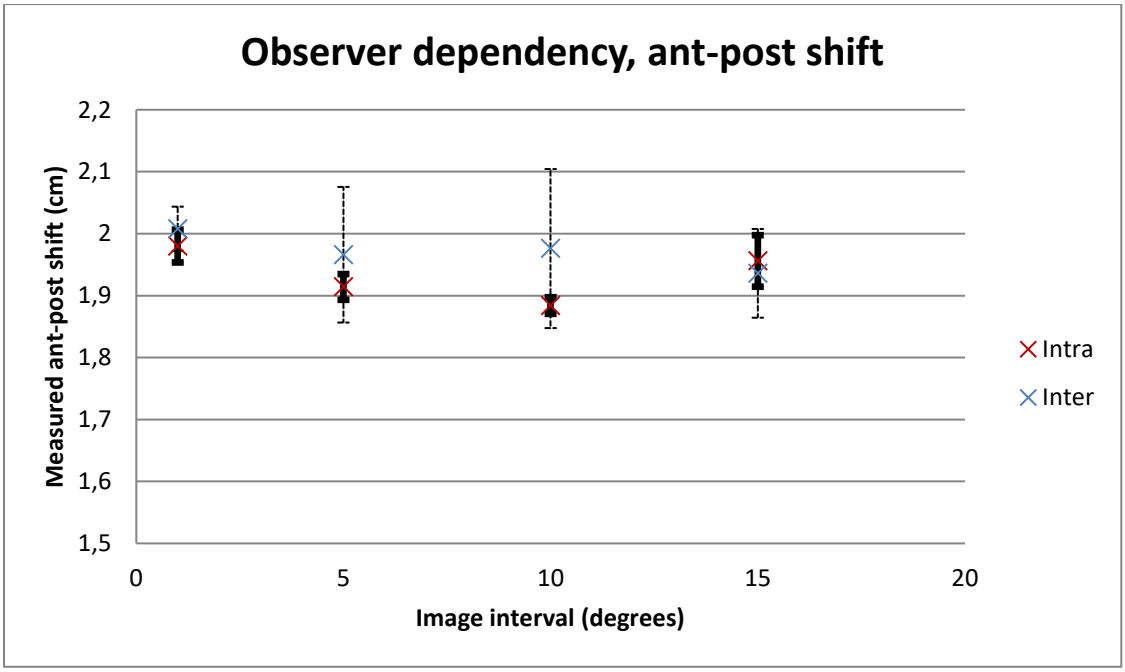

Figure 4.49: Observer dependency in determination of the ant-post measured shift for various imaging intervals.

From Figure 4.48 & 4.49 it can be seen that the intra-observer dependency is relatively small for measured lateral and anterior-posterior shifts with a maximum standard deviation of 0.06 and 0.04 cm respectively. The maximum deviations are both at an imaging interval of 15°. The inter-observer dependency is more pronounced with an average standard deviation of 0.08 cm for the lateral and 0.09 cm for the anterior-posterior shifts.

Table 4.9: Absolute difference in intra- and inter observer measurements for lateral and anterior-posterior shifts.

	Absolute difference (mm)	
Image interval (degrees)	Lateral	Anterior-posterior
1	0.44	0.28
5	0.78	0.52
10	1.02	0.92
15	0.98	0.2

The difference between intra- and inter observer measurements are all less than 2 mm for both lateral and anterior-posterior shifts. The maximum difference is 1.02 mm for the lateral shift at an imaging interval of 10°. A difference of 2 mm and less is clinically acceptable. It can therefore be concluded from these results that the method used for determination of lateral and anterior-posterior shift is observer independent.

4.5.2 Rotation

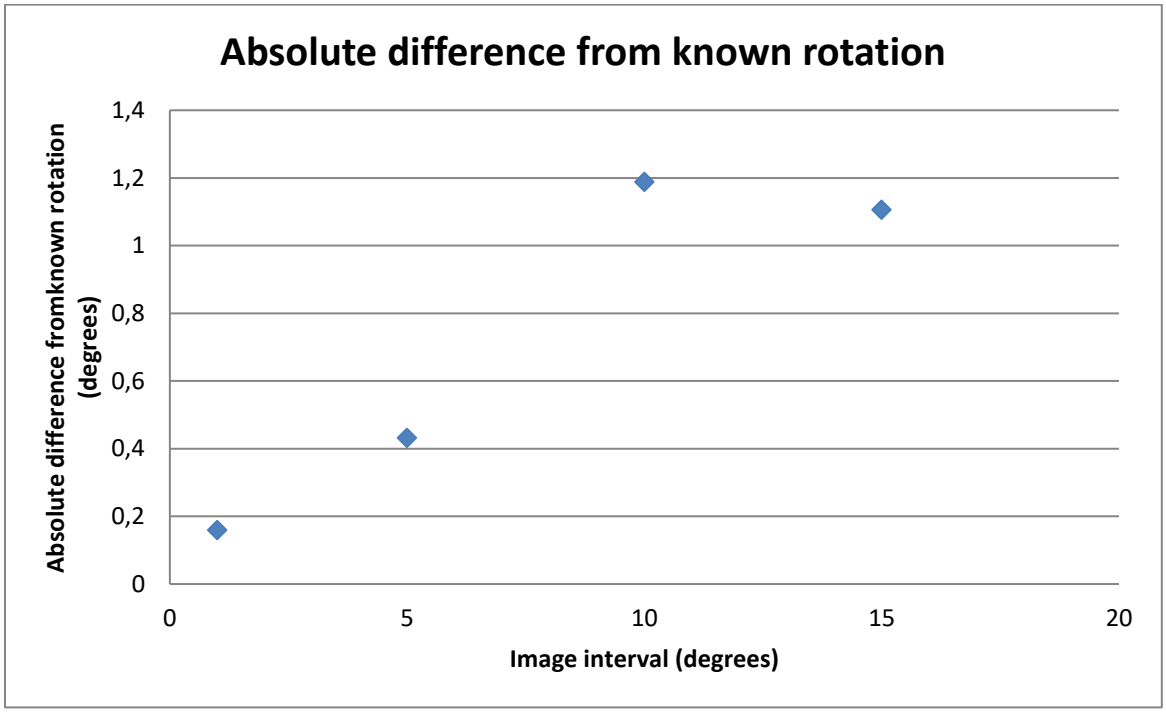

Figure 4.50: The absolute difference (based on intra-observer measurements) between the measured rotation and known rotation of 5°.

The absolute difference between measured rotation and known rotation is less than 1° for imaging intervals of 1° and 5° and larger than 1° for both 10° and 15° intervals (Figure 4.50). Due to poor image quality and large reconstruction artifacts on the images obtained with 10 and 15° intervals, the recommendation would be to only use images reconstructed with a maximum image interval of 5° for determination of rotation.

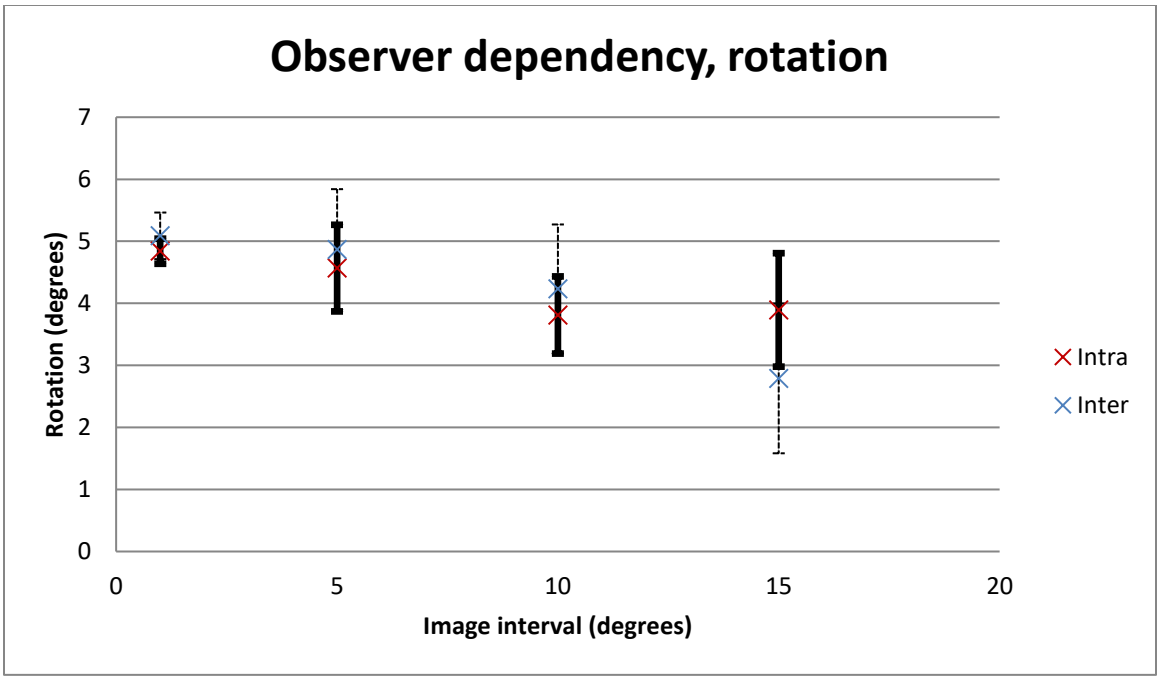

Figure 4.51: Observer dependency in determination of rotation for various imaging intervals.

Figure 4.51 shows that the inter-observer dependency for determination of rotation is more prominent than the intra-observer dependency. The maximum standard deviation for both intra- and inter observer measurements is at an imaging interval of 15° with values of 0.91° and 1.21° respectively.

Table 4.10: Absolute difference in intra- and inter-observer measurements for rotation.

	Absolute difference (degrees)
Image interval (degrees)	Rotation
1	0.25
5	0.30
10	0.42
15	1.10

The maximum difference is 1.10° at an imaging interval of 15°. For both intra- and inter observer measurements the absolute difference at 1°, 5° and 10° imaging intervals are small with

a maximum of 0.42°. From these results it can be concluded that the method used for determination of rotation is observer independent.

Table 4.11: Summary of results obtained for positional accuracy measurements based on intra-observer measurements for 1° and 5° image intervals.

Positional accuracy	
Longitudinal:	
• **Shift**	1.95 cm
• **Difference from known shift of 2 cm**	0.05 cm
Lateral:	1.93 cm ± 0.04
• **Shift (1°)**	0.07 cm
• **Difference from known shift of 2 cm**	1.86 cm ± 0.03
• **Shift (5°)**	0.14 cm
• **Difference from known shift of 2 cm**	
Superior-inferior:	1.98 cm ± 0.03
• **Shift (1°)**	0.02 cm
• **Difference from known shift of 2 cm**	1.91 cm ± 0.02
• **Shift (5°)**	0.09cm
• **Difference from known shift of 2 cm**	
Rotation:	4.84° ± 0.20°
• **Shift (1°)**	0.16°
• **Difference from known rotation of 5°**	4.57° ± 0.70°
• **Shift (5°)**	0.43°
• **Difference from known rotation of 5°**	

From Table 4.11 it can be seen that the maximum deviation from the known shift for all three directions are less than 2 mm with the maximum 1.4 mm in the lateral direction. Although a positional error of ± 2 mm is tolerable, it could be clinically unacceptable in some cases especially with high-precision radiotherapy techniques such as IMRT. A setup error of this order could have detrimental effects in high dose gradient regions causing possible under dosage of the target and over dosage of the surrounding normal tissues. The maximum deviation from the known rotation is 0.43° which is an acceptable value. Although the results for both translation and rotation obtained at 5° intervals are satisfactory, higher levels of accuracy can be achieved by reducing the image intervals (less than 5°).

Considering the dose received during the 200° image acquisition arc, using 5° instead of 1° image intervals will reduce the dose in the central part of the phantom/patient from ± 158 cGy to ± 30 cGy (dose delivered for one image interval is approximately 0.793 cGy). Except for the advantage of dose reduction, the image acquisition time as well as reconstruction time will also be reduced yielding a more optimal technique. The number of image intervals will thus depend on the trade-off between allowable dose to the patient and level of accuracy and image quality required.

Chapter 5

Conclusion

The feasibility of cone-beam CT using an Elekta Precise linac and EPID was investigated in this study. An iViewGT portal imaging device was used for reconstruction of megavoltage cone beam computed tomography image data sets. From the discussions in Chapter 4 the following can be concluded:

[1] In this study planar images obtained with an 8 MV photon beam and an EPID was used to reconstruct cone-beam CT images. The Feldkamp-type algorithm which, through a weighting function, is an approximation of the filtered backprojection algorithm proved to be an optimal reconstruction method for CBCT. Two hundred projection images were acquired (from gantry angle -100° to 100°, one degree intervals) using 1MU/image. Reconstructed images with acceptable image quality (detail) were obtained by applying only the sinc filter function. Due to overall image degradation caused by an additional smoothing filter no smoothing was performed. The number of projection images used will influence several factors in the reconstruction process. These factors include image acquisition and reconstruction time, image quality and dose to the patient. By increasing the angular spacing between projection images the reconstruction time can be reduced to $1/a$, where a is the angular spacing in degrees. The reduction in reconstruction time will however be limited by the visual appearance of the image. Both the SNR and CNR will be reduced as the number of projections is reduced. A trade-off will therefore exist between the number of projections and image quality.

[2] The process of geometric calibration was used to derive a set of posing parameters that fully describes the geometry of the CBCT system. A cylindrical perspex phantom consisting of two rings of BBs equidistant from the center served as a calibration phantom. Correcting for these parameters ensured accurate reconstruction without any artefacts caused by geometrical misalignments of the system. Parameters analyzed in this study included: (a) piercing point (projection of isocenter on the EPID), (b) rotation of the detector around its normal axis, (c) detector tilt angles, and (d) gantry angle variation. Due to the sensitivity of detector tilt angles on the accurate positioning of BBs in the phantom, and results from literature studies illustrating the small influence of tilt angle correction on the reconstructed images, it was decided to restrict misalignment corrections to piercing point, detector rotation and gantry angle variation.

The piercing point can be measured with either the calibration phantom or a single BB. The reproducibility of both of these methods over a 7 day period is good with the standard deviation in projected isocenter ((u,v) location) less than 1 mm. The overall motion from the mean projected isocenter for both methods is less than 2 mm. Thus, either one of these methods will yield accurate results in determination of projected isocenter. Rotation of the detector around its normal axis was determined by using the calibration phantom. The maximum rotation was 0.24° with a standard deviation of 0.21° for the full angular range of 200°. Due to gravitational forces acting on the treatment machine the true gantry angle can be different from the set gantry angle. To ensure backprojection of projection images were done from the true gantry angle the readout from the Elekta desktop was used instead of the set gantry angle. The maximum deviation from the set gantry angle was 0.23° with a standard deviation of 0.10° for the full angular range (200° arc).

[3] Steep dose gradients between tumor and critical organs can be achieved with high-precision radiotherapy techniques. This highlights the need for accurate localization of anatomical information before treatment delivery. Verification of treatment localization is done by using images obtained prior to treatment delivery. Good quality images are therefore a prerequisite. A standard image quality phantom (Catphan®) can be used for quantification of image quality in terms of spatial- and contrast resolution, SNR and uniformity. Cone-beam images of the phantom were acquired using an arc of 200°.

The spatial resolution of the smallest visible bar group is 0.3 lp/mm which is sufficient for visualization of bony landmarks and fiducial markers i.e. surgical clips used during image registration. Soft tissue visualization would only be feasible if the number of MUs used is increased (higher dose delivered). The integral non-uniformity is 9.7% and 0.43% in the vertical and horizontal direction respectively. For comparison the integral non-uniformity of the conventional CT scanner is 0.34%. The poor result in the vertical direction can be attributed to the attenuation of the beam. The level of noise is quantified by the SNR and yields a mean value of 11.99 for all five ROIs. This result is poor considering that a value of 23.39 and 7.02 is measured in the top and bottom part of the image respectively. Uniformity and the SNR can be improved by applying an attenuation correction factor during reconstruction or acquiring images using a 360° instead of 200° arc. Parker weighting should also be applied to correct for data redundancy due to the use of the short scan trajectory of 200°. Due to poor contrast resolution of the reconstructed images this parameter was evaluated by visual inspection only. Sensitometric objects with varying electron

densities were used. Objects with large electron density differences such as bone and air could clearly be distinguished but small electron density differences could not be seen clearly. Based on contrast resolution these images can thus be used in areas with objects such as bony landmarks and air cavities (head and neck cases) but not where soft tissue visualization is a pre requisite (pelvis area). The most pronounced artefacts notable on the reconstructed images are ring- and streak artefacts. These artefacts can be corrected for by recalibration of the EPID and additional filtration.

[4] The dose imparted during image acquisition was evaluated using a PTW-30012 ionization chamber, film measurements and the XIO treatment planning system. The ionization chamber provided an accurate absolute dose estimation, film measurements and the TPS provided an overall shape of the dose distribution for the 200° arc. The absolute dose measured in the center of the phantom (position coinciding with the treatment isocenter) were 160.00 cGy, 159.00 cGy and 158.90 cGy with the ion chamber, film and TPS respectively. This value is almost equal to one fraction of a typical radiotherapy treatment and very high compared to results in the literature (5 to 12 cGy), which makes it undoubtedly to high for clinical use.

Before discussing methods for dose reduction it is important to keep in mind that the dose delivered will have a direct influence on the image quality of the reconstructed images. In the literature several options have been explored including limiting the field of view, reducing number of projection images, image post processing techniques to enhance image quality and the development of a more advanced image receptor. In this study the technique

used for dose reduction was a reduction in the number of projection images used. The dose can be reduced from 160 cGy to 15 cGy if the number of projection images is reduced from two hundred to twenty. Although this value is much more in line with recent studies the image quality will be degraded to such an extent that these images could not even be used for registration of bony landmarks. The minimum number of projection images that can be used and still yield acceptable image quality is 40 resulting in a dose of 30 cGy. The capabilities or detection efficiency of the receptor (EPID) also plays a major part in dose delivery. For example, if the system could deliver fractions of MUs and the EPID could be optimized to detect these fractional MUs and still yield acceptable image quality, the dose could be significantly reduced. Using arc therapy mode instead of step-and-shoot would also reduce the number of MUs used but, due to hardware limitations and the fact that an existing system is being evaluated in this study this option was not explored. In retrospect it would have been better to use a 6 MV beam instead of an 8 MV beam for image acquisition. This would yield a reduction in dose as well as an improvement in image quality.

[5] Cone-beam reconstructed images are mainly used for treatment verification purposes i.e. verification of patient set-up. To truly test the feasibility of the system (linac and EPID) in terms of setup verification, positional accuracy was verified through measurements of simulated shifts and rotations. 2 cm shifts in the lateral, longitudinal and anterior-posterior direction and a rotation of 5° were simulated and measured. This was repeated for reconstructed images using various numbers of projection images. Due to poor image quality and considerable reconstruction artefacts the recommendation would be to only use images reconstructed with a minimum of forty projection images. The absolute difference

from known shifts (all directions) and rotation was less than 1 mm and 1° for two hundred projection images and less than 2 mm and 1° for forty projection images. For conventional treatment techniques an accuracy of 2 mm in measurement of setup error would be acceptable, but for high-precision treatment techniques accuracies of at least 1 mm and lower would be desired. This method would therefore be feasible for measurement of setup errors in conventional treatment techniques.

The intra- and inter observer dependency for measurement of positional accuracy was evaluated and results showed that this method is not observer dependant and would yield results within 2mm and one degree for different observers.

[6] The limitations of this method in order to be used for setup verification in a clinical environment are image acquisition time and dose imparted during image acquisition. Using fewer projection images would address this problem to some extent, but not adequately. Other means of reduction in image acquisition time and dose which is beyond the scope of this study (alterations in hardware i.e. EPID detection efficiency and linac output) can thus be used to improve this method to a clinical acceptable and feasible level.

Abstract

In this study the feasibility of patient setup verification through cone-beam computed tomography (CBCT) using an Elekta Precise linear accelerator (linac) and electronic portal imaging device (EPID) was investigated. CBCT images are used for treatment verification i.e. determination of patient set-up errors prior to treatment delivery. An 8 MV photon beam was used to acquire planar images of an anthropomorphic head phantom as the system rotates in a 200° arc around the phantom. The Feldkamp-type algorithm which, through a weighting function, is an approximation of the filtered backprojection algorithm was used to perform reconstruction of 2D transversal CT images from the projection/planar images. Reconstruction was done using tools developed with the Interactive Data Language (IDL) software package. The reconstruction technique was evaluated in terms of image quality, dose imparted during image acquisition and positional accuracy.

Geometric calibration of the imaging system (linac and EPID) was performed to derive a set of parameters that fully describes the geometry of the system. These parameters include piercing point (projection of isocenter on EPID), detector rotation around its normal axis, detector tilt angles and gantry angle variation. A dedicated calibration phantom was manufactured and used to determine and correct for the above-mentioned parameters during the reconstruction process. These corrections ensure accurate reconstruction and avoidance of image artefacts due to geometrical misalignments of the system.

Image quality was evaluated using a standard image quality phantom (Catphan®). Parameters such as signal-to-noise ratio (SNR), spatial resolution, contrast resolution and uniformity were used to quantify image quality. Due to the high energy of the photon beam, reconstructed images yield relatively poor image quality compared to kilovoltage photons. Although soft tissue contrast were very poor, image quality was sufficient for visualization of bony landmarks, air cavities or fiducial markers. Image quality can be enhanced by increasing the number of monitor units (MUs) used but, this will lead to an increase in dose which is not desirable from a clinical point of view.

Dose imparted during image acquisition was measured using an ionization chamber placed at the treatment isocenter. An overall shape of the dose distribution was obtained by film measurements and a simulated plan computed by a treatment planning system (TPS). The dose measured at the centre of the phantom was ±160 cGy which is clinically unacceptable. There exist several dose reduction techniques; in this study a reduction in number of projection images were used. The dose was reduced to ± 30 cGy when 40 projection images instead of 200 were used. Due a trade-off between dose and acceptable image quality the dose could not be reduced any further without degrading the image quality beyond clinically acceptable levels.

Positional accuracy was evaluated by simulation of phantom shifts and rotation. The reconstructed images were then used to determine these shifts and rotation. Shifts and rotation could be determined within 2 mm and one degree respectively for images reconstructed with 40 projection images. Larger angular increments yield poor image

quality and severe reconstruction artefacts which resulted in false positive values (absolute difference from simulated shift and rotation smaller than 2 mm and one degree). Intra- and inter observer dependency were evaluated during positional accuracy determination. Results showed that the method for determination of position and rotation is observer independent.

The clinical feasibility of this method is limited by image acquisition time and dose imparted during image acquisition. Further investigations (which are beyond the scope of this study) should be conducted to explore means of reduction in image acquisition time and dose i.e. improvement of EPID detection efficiency and linac output (fractional MUs).

Key words: Megavoltage cone-beam CT, Electronic portal imaging device, geometric calibration, image quality, positional accuracy

Opsomming

Die moontlikheid van rekenaar tomografie (RT) met konus-vormige bundels (KB) deur gebruik te maak van ‘n Elekta Precise lineêre versneller en ‘n elektroniese portale beeldings apparaat (EPBA) vir verifikasie van pasiënt opstelling word in hierdie studie ondersoek. Beelde verkry vanaf KBRT word hoofsaaklik gebruik vir die verifikasie van behandeling in radioterapie bv. die kwantifisering van opstel foute van pasiënte voor die aanvang van behandeling. Planare transmissie beelde van ‘n antropomorfiese kop fantoom is deur middel van ‘n 8 MV foton bundel opgeneem terwyl die beeldings sisteem (versneller en EPBA) in ‘n 200º boog rondom die fantoom roteer. Die Feldkamp-tipe algoritme, wat deur ‘n geweegde funksie ‘n benadering van die gefiltreerde terugprojeksie algoritme is, is gebruik vir die rekonstruksie van 2D transversale RT beelde vanaf die planare/projeksie beelde. Die ‘Interactive Data Language (IDL)’ sagteware pakket is gebruik om ‘n program te ontwikkel vir die rekonstruksie prosedure. Die rekonstruksie tegniek is geevalueer op gronde van beeld kwaliteit, dosis neergelê tydens beeld opname en posisionele akkuraatheid.

‘n Stel parameters wat ‘n volledige beskrywing van die geometrie van die sisteem lewer kan afgelei word deur geometriese kalibrasie van die beeldings sisteem. Hierdie parameters sluit in die sny punt (projeksie van isosenter op die EPBA), die rotasie van die detektor rondom sy normale as, detektor tilt hoeke en die deviasie van die versneller raamwerk hoek tydens rotasie. Die parameters is bepaal deur ‘n spesiaal vervaardigde kalibrasie fantoom te gebruik. Korreksies vir hierdie parameters is aangebring tydens die rekonstruksie proses. Hierdie korreksies verseker akkurate rekonstruksie en die voorkoming van beeld artefakte as gevolg van afwykings in die geometriese instellings van die sisteem.

‘n Standaard beeld kwaliteit fantoom (Catphan®) is gebruik vir evaluasie van die beeld kwaliteit van gerekonstrueerde beelde. Beeld kwaliteit is gekwantifiseer deur die volgende parameters: sein-tot-geruis verhouding (SGV), ruimtelike resolusie, kontras resolusie en uniformiteit. A.g.v die gebruik van ‘n hoë energie foton bundel is die beeld kwaliteit van die rekonstruksie beelde swakker in vergelyking met beelde opgeneem met laer (kilovolt) energie bundel. Die sagte weefsel kontras was baie swak, maar beeld kwaliteit is nogsteeds voldoende vir die visualisering van benige strukture, lug holtes en geometriese merkers. Deur die aantal monitor eenhede waarmee beelde opgeneem word te verhoog kan die beeld kwaliteit tot ‘n groot mate verbeter word , maar dit sal lei na ‘n toename in dosis wat ongewens is uit ‘n kliniese oogmerk.

‘n Ionisasie kamer geposisioneer by isosenter is gebruik om dosis neergelê tydens beeld opname van die fantoom te bepaal. Film metings en ‘n gesimuleerde behandelingsplan bereken deur die beplannings stelsel is gebruik om ‘n dosis distribusie te verkry. Die dosis in die middel van die fantoom was ongeveer 160 cGy. Uit ‘n kliniese oogpunt is dit onaanvaarbaar hoog. Verskeie tegnieke om dosis te verminder kan gebruik word; in hierdie studie is die vermindering in aantal projeksie beelde as dosis verminderings tegniek gebruik. Die dosis is verlaag na 30 cGy wanneer 40 projeksie beelde i.pv 200 gebruik word. A.g.v die verwantskap tussen dosis en beeld kwaliteit kan die dosis nie nog meer verlaag word sonder om die beeld kwaliteit so te verswak dat dit onprakties vir kliniese gebuik sal wees.

Posisionele akkuraatheid was ondersoek deur gesimuleerde skuiwe en rotasies op ‘n fantoom te doen. Gerekonstrueerde beelde van hierdie ‘nuwe’ posisies is dan geanaliseer om die skuiwe en rotasies te bepaal. Die skuiwe en rotasies kon binne 2 mm en een graad bepaal word vanaf beelde gerekonstrueer met 40 prokesies. Die beeld kwaliteit van rekonstrusie beelde gerekonstrueer met groter hoek intervalle (minder projeksies) is swak met baie rekonstruksie artifakte en lewer vals

positiewe waardes (skuiwe en rotasies van minder as 2 mm en een graad). Die intra- en inter waarnemer afhanklikheid van die metode is ook getoets. Die resultate het bewys dat die metode vir bepaling van posisie en rotasie waarnemer onafhanklik is.

Die moontlikheid om hierdie metode klinies te implementeer word beperk deur die beeld opname tyd en dosis neergelê tydens beeld opname. Verdere studies (wat buite die bestek van hierdie studie val) moet onderneem word om ander metodes van vermindering in beeld opname tyd en dosis te ondersoek bv. deur verbetering van EPBA se deteksie effektiwiteit en lineêre versneller uitset (moontlikheid om fraksionele monitor eenhede te lewer).

Sleutelwoorde: Megavolt konus-vormige rekenaar tomografie, elektroniese beeldings apparaat, beeld kwaliteit, posisionele akkuraatheid, geometriese kalibrasie

References

1. AAPM. Specification and acceptance testing of computed tomography scanners. American Institute of Physics: New York. 1993 May. Report No.: 39

2. Antonuk LE. Electronic portal imaging devices: A review and historical perspective of contemporary technologies and research. International Journal of Physics in Medicine and Biology. 2002;47:R31-R65.

3. Barrett J, Keat F. Artifacts in CT: Recognition and Avoidance. 2004; 24:1679-1691.doi:10.1148/rg.246045065.

4. Boyer AL, Antonuk LE, Fenster A, Herck MV, Meertens H, Munro P, et al. A review of electronic portal imaging devices (EPIDs). International Journal of Medical Physics. 1992;19(1):1-16.

5. Broderick M, Menezes G, Leech M, Coffey M, Appleyard R. A comparison of kilovoltage and megavoltage cone-beam CT in radiotherapy. Journal of Radiotherapy in practice. 2009;6:173-8.

6. Bushberg JT, Seibert JA, E M Leidholdt J, Boone JM. The essential Physics of Medical Imaging. III WMP, editor. Baltimore, Maryland: Williams & Wilkens; 1994.

7. Buzug TM. Computed Tomography: From photon statistics to modern cone-beam CT. Berlin, Heidelberg: Springer-Verlag; 2008.

8. CAPCA. Standards for Quality control at Canadian Radiation Treatment Centers - Medical Linear Accelerators; 2005 July.

9. Chen J, Morin O, Aubin M, Bucci M, Chuang C, Pouliot J. Dose-guided radiation therapy with megavoltage cone-beam CT. Brithish Journal of Radiology. 2006;79(Spec No.1):S87-S98.

10. Cho Y, Moseley DJ, Siewerdsen JH, Jaffray DA. Accurate technique for complete geometric calibraiton of cone-beam computed tomography systems. International Journal of Medical Physics. 2005;32(4):968-83.

11. Curry TS, Dowdey JE, Murry RC. Christensens's Physics of Diagnostic Radiology. Fourth ed. Malvern, Pennsylvania: Lea & Febiger; 1990.

12. Elekta. iViewGT^{TM} Electronic Portal Imaging Device - Product Data & Technical Specifications. [Internet] [updated 2011; cited September 2009]; Available from: http://www.medwow.com/med/portal-imaging-system/elekta/iview-gt/172.model-spec.

13. Fanning D. IDL Programming techniques. Fanning software consulting, USA; 1999.

14. Fayed L. Methods for treatment of cancer. 2009 [cited October 2010]; Available from: http://www.cancer.about.com/od/treatmentoptions/a/options.htm.

15. Feldkamp L, Davis L, Kress J. Practical cone-beam algorithm. Journal of Opt Soc Amer. 1984;1(6):612-9.

16. Gayou O, Miften M. Commissioning and clinical implementation of a megavoltage cone-beam CT system for treatment localization. International Journal of Medical Physics. 2007;34(8):3183-92.

17. Gayou O, Parda DS, Johnson M, Miften M. Patient dose and image quality from mega-voltage cone-beam computed tomography imaging. International Journal of Medical Physics. 2006;34(2):499-506.

18. Groh B, Siewerdsen D, Wong J, Jaffray D. A performance comparison of flat-panel imager-based MV and kV cone-beam CT. International Journal of Medical Physics. 2002;29(6):967-75.

19. Hurkmans CW, Remeijer P, Levsque JV, Mijnheer B. Set-up verification using portal imaging; review of current clinical practice. International Journal of Radiotherapy and Oncology. 2001;58:105-20.

20. ICRU. Prescribing, recording and reporting photon beam therapy. 1993. Report No.: 50

21. Jaffray DA, Siewerdsen JH, Wong JW, Martinez AA. Flat panel cone-beam computed tomography for image-guided radiation therapy. International Journal of Oncology, Biology and Physics. 2002;53(5):1337-49.

22. Johns HE, Cunningham JR. The Physics of Radiology. Fourth ed. Springfield, Illinois: CC Thomas; 1983.

23. Kak A, Roberts B. Image reconstruction from projections. In: Young T, Funds K, editors. Handbook of Pattern Recognition and Image Processing. New York: Academic Press; 1986.

24. Kak CA, Slaney M. Principles of Computerized Tomographic Imaging. New York: IEEE Press; 1999.

25. Karolczak M, Taubenreuther U, engelke K, Lutz A, Schaller S, Kalender W. Practical approach to misalignment correction in single-circle orbit cone-beam tomography. 2001 [cited March 2010]; Available from: http://cfi.lbl.gov/3D-2001/abstracts/03-13.pdf.

26. Khan FM. The Physics of Radiation Therapy. Baltimore: Williams & Wilkens; 1984.

27. Kirby MC, Glendinning AG. Developments in electronic portal imaging systems. The British Journal of Radiology. 2006;79:S50-S65.

28. Langmack KA. Review article: Portal imaging. The British Journal of Radiology. 2001;74:789-804.

29. Leechi M, Fossati P, Elisei F, Orecchia R, Lucignani G. Current concepts on imaging in Radiotherapy. European Journal of Nuclear Medicine and Molecular Imaging. 2007;35:821-37.

30. Ma C, Paskalev K. In-room CT techniques for Image Guided Radiation Therapy Medical Dosimetry. 2006;31(1):30-9.

31. Meeks S, Harmin JJ, Langen K, Willoughby T, Wagner T, Kupelian P. Performance characterization of megavoltage computed tomography imaging on a helical tomotherapy unit. International Journal of Medical Physics. 2005;32(8):2673-81.

32. Midgley S, Millar RM, Dudson J. A feasibility study for megavoltage cone-beam CT using a commercial EPID. International Journal of Physics in Medicine and Biology. 1997;48 155-69.

33. Morin O, Gillis A, Chen J, Aubin M, Bucci M, Roach M, et al. Megavoltage cone-beam CT: System description and clinical applications. Medical Dosimetry. 2006;31(1):51-61.

34. Mueller K, Chang J, Almos H, Ling C. Cone-beam Computed tomography (CT) for a Megavoltage Linear Accelerator (LINAC) using an Electronic Portal Imaging Device (EPID) and the Algebraic Reconstructin Technique (ART). 2000 [cited January 2010]; Available from: http://www.cs.sunysb.edu/~mueller/papers/embs2000.

35. Mueller K, Yagel R, Wheller JJ. Accurate low-contrast 3D cone-beam reconstruction with algebraic methods. 1999 [cited January 2010]; Available from: ftp://ftp.cis.ohio-state.edu/pub/yagel/cone/ps/gz.

36. Noo F, Clackdoyle R, Mennessier C, White TA, Roney TJ. Analytic method based on identification of ellipse parameters for scanner calibration in cone-beam tomography. International Journal of Physics in Medicine and Biology. 2000;45:3489-508.

37. Oelfke U, Tücking T, Nill S, Seeber A, Hesse B, Huber P, et al. Linac-integrated kV cone-beam CT: Technical features and first applications. Medical Dosimetry. 2006;31(1):62-70.

38. Pouloit J, Bani-Hashemi A, Chen J. Low-dose megavoltage cone-beam CT for radiation therapy. International Journal of Oncology, Biology and Physics. 2005;61(2):552-60.

39. Renstrom J. Evaluation of the Elekta Synergy concept for patient positioning in image-guided radiotherapy. Lund: Lund University; 2005.

40. Ruchala K, Olivera G, Schloesser E, Maackie T. Megavoltage CT on a Tomotherapy system. Journal of Physics in Medicine and Biology. 1999;44(10):2597-621.

41. Scarfe WC, Farman AG. What is cone-beam CT and how does it work? The dental Clinics of North America. 2008;52:707-30.

42. Schlegel W. New Technologies in 3D Conformal Radiation Therapy: Introduction and Overview. In: Brady LW, Heilmann HP, Molls M, editors. New technologies in Radiation Oncology. Heidelberg: Springer; 2006. p. 1-6.

43. Sillanpaa J, Chang J, Mageras G, Riem H, Ford E, Ttodor D, et al. Developments in megavoltage cone-beam CT with an amorphous silicon EPID: Reduction of exposure and synchronization with respiratory gating. International Journal of Medical Physics. 2005;32(3):809-29.

44. Sun Y, Hou Y, Zhao F, Hu J. A calibration method for misaligned scanner geometry in cone-beam computed tomography. NDT & E International. 2006;39(6):499-513.

45. Thomas THM, Devakumar D, Purnima S, Ravindra BP. The adaption of megavoltage cone-beam CT for use in standard radiotherapy treatment planning. International Journal of Physics in Medicine and Biology. 2009;54:2067-77.

46. Valton S, Peyrin F, Sappey-Marinier D. Analysis of cone-beam artifacts in off-centered circular CT for four recosntruction methods. international Journal of Biomedical Imaging. 2006:1-8.

47. Varian. One revolution is all it takes. 2011 [cited April 2011]; Available from: http://www.varian.com/media/oncology/solutions/pdf/Rapidarc_brochure.pdf.

48. Wang G, Vannier MW. Computerized Tomography. Wiley Encyclopedia of electrical and electronics engineering; 1998.

49. Webb S. VMAT: its role in Radiotherapy. 2009 [cited April 2011]; Available from: http://www.medicalphysicsweb.org./blog/MPWwinter09_digitalpdf.pdf.

Acknowledgements

The author would like to thank the following people:

My promoter Dr. F.C.P. du Plessis and co-promotor Prof. C.A. Willemse for all the time they devoted in numerous discussions and solutions to make the realization of this work possible.

My colleagues Dr. W.I.D. Rae, Prof C.P. Herbst and Mr. W Shaw for their contribution in various aspects of this study.

The chief of the radiation oncology department Dr. A Bester for giving her approval for using the apparatus in the department.

My husband Tielman and son John-Robert.

Everyone else that made a contribution, big or small, for making this possible.

Appendix A: IDL source code, image reconstruction

```
      pro mywidget_exit, event

      widget_control, event.top, /destroy
      print, '- Exiting mywidget'
5
      end
      pro mywidget_slider, event

      widget_control, event.top, get_uvalue = state
10    widget_control, state.xslider, get_value = xx                    ; lower level
      widget_control, state.zslider, get_value = z                     ; upper level

      state.data = state.finaal

15    state.data = state.data * 255/max(state.data)

      state.data = (state.data - xx) * 255/(z-xx)

      for aa = 0,799 do begin
20    for bb = 0,799 do begin

      if (state.data(aa,bb) lt 0.0) then state.data(aa,bb) = 0.0
      if (state.data(aa,bb) gt 255.0) then state.data(aa,bb) = 255.0

25    endfor
      endfor

      tvscl, state.data

30    widget_control, event.top, set_uvalue = state

      end

      pro cbct2a
35
      result = uintarr(1024, 1024)
      result1b = uintarr(1024,1024)
      result1c = uintarr(1024,1024)
      result1 = uintarr(256,256)
40    header = bytarr(350)
      result1a = bytarr(256,256)
      ry = fltarr(256)
      finaal = fltarr(256,256)
      w3 = fltarr(256)
45    ww3 = fltarr(256)
      yoorx = fltarr(256,256)
      q3 = fltarr(256,256)
      qq3 = fltarr(256,256)
      hh = fltarr(256,256)
50    bpj = fltarr(256,256)
      ;volume = fltarr(512,512,100)

      U3 = fltarr(256,256)
      Pa = fltarr(256,256)
55    P3 = fltarr(256,256)
      zz = fltarr(256,256)

      sino = fltarr(256,1)
      sino2 = fltarr(256,360)
60
      beeld1 = uintarr(360,256,256)
      res = fltarr(256,256)

      ;_____________________________________________________________________
65
      ;              Skep 'n koordinaat stelsel en definieer parameters

      ;_____________________________________________________________________

70    D = 100.0                                ; Afstand van bron na oorsprong/verwysings asse stelsel
      dp = 100.0/(26.0/256.0)                  ; Afstand van bron na oorsprong/verwysings asse stelsel
      de = 60.0/(26.0/256.0)                   ; Afstand van oorsprong/verwysings asse stelsel na detek

      a = (26.0/256)                           ; sampling interval cm/pixel
```

```
75
      for a3 = 0,255 do begin

      w3(a3) = (a3-128)                          ; x-waardes (pixel)
      ww3(a3) = (a3-128)                         ; y-waardes (pixel)
80
      endfor


      for t3 = 0,255 do begin
85
      x3 = w3(t3)

      for tt3 = 0,255 do begin

90    y3 = ww3(tt3)

      r3 = sqrt(x3 ^2 + y3 ^2)                   ;r waarde (pixel)

      phi = atan(y3,x3)+!pi                      ;hoek phi (radiale)
95
      h = (y3*dp)/(dp+de)                        ;hoogte van 'snit' bo rotasie vlak

      q3(t3,tt3) = r3
      qq3(t3,tt3) = phi
100   hh(t3,tt3) = h

      endfor

      endfor
105

      ;_____________________________________________________________________

      ;                        Sinc filter funksie - Spatial Domain
110   ;_____________________________________________________________________

      s = fltarr(51)


115   s(0 + 25) = (1.0)/(8.0*a*a)

      for m = 1,25 do begin

      if (m mod 2 eq 0) then  q = 0.0
120
      if (m mod 2 ne 0 ) then  q = (-1)/((2*!pi^2)*a*a*m*m)

      s(m+25) = q
      s(25-m) = q
125
      endfor

      ;plot, s
      ;stop
130
      ;_____________________________________________________________________

      ;_____________________________________________________________

135   ;  Low Pass Cosine Filter - Spatial Domain

      ;_____________________________________________________________

      LP = 0.0
140
      LPC = fltarr(50)

      SI = 50.0 / 256.0

145   for a = 0,24 do begin

      LP1 = 2/(!pi^2*SI)
      LP2 = (!pi/2)
```

```
      LP3 = (1.0+4.0*a^2)/(1.0-4.0*a^2)
150   LP4 = 1.0/(1.0-4.0*a^2)

      if (a mod 2 eq 0) then LP = 5*(LP1*(LP2-LP3)*LP4)
      if (a mod 2 ne 0) then LP = 5*(LP1*(-1*(LP2)-LP3)*LP4)

155   LPC(a+25) = LP
      LPC(25-a) = LP

      endfor

160   kombfilter = LPC*s

      ;window, 1
      ;plot, kombfilter, color = 255
      ;stop
165
      ;_____________________________________________________________

      ;  Low Pass Cosine Filter - Frequency Domain

170   ;_____________________________________________________________

      fr = 0.0

      fx = fltarr(255)
175
      fx(127) = 0

      ft = 41 / 1024.0

180   for fa = 0,127 do begin

      fr =  (fa) * cos((0.0985*!pi)*fa*ft)

      fx(fa+127) = abs(fr)
185   fx(127-fa) = abs(fr)

      endfor

      ;plot,fx
190   ;stop

      ;_____________________________________________________________

      ;          Shepp Logan Filter - Spatial Domain
195
      ;_____________________________________________________________


      sly =  0.0
200
      slp = fltarr(50)

      slt = 41.0/1024.0

205   for slw = 0,24 do begin

      sly = 50 / (!pi^2 * slt * (1 - 4* slw^2))

      ;p(w) = y
210
      slp(slw+25) = sly
      slp(25-slw) = sly

      endfor
215
      ;plot, slp, color = 255
      ;stop

      ;_____________________________________________________________
220
      ;lookup table for image shift - AB direction
```

```
      shifta  = fltarr(9)
      angles  = fltarr(9)
225
      shifta(0) = 0.69
      shifta(1) = 1.42
      shifta(2) = 0.43
      shifta(3) = -0.57
230   shifta(4) = -1.53
      shifta(5) = -1.33
      shifta(6) = -0.73
      shifta(7) = 0.72
      shifta(8) = 0.69
235
      angles(0) = 0
      angles(1) = 40
      angles(2) = 90
      angles(3) = 140
240   angles(4) = 180
      angles(5) = 220
      angles(6) = 270
      angles(7) = 320
      angles(8) = 360
245
      ;lookup table for image shift - GT direction

      shiftg  = fltarr(9)

250   shiftg(0) = -0.33
      shiftg(1) = 0.30
      shiftg(2) = 0.74
      shiftg(3) = 0.22
      shiftg(4) = 0.48
255   shiftg(5) = 0.42
      shiftg(6) = 0.81
      shiftg(7) = 0.10
      shiftg(8) = -0.33

260   ;_____________________________________________________________

      ;                    Lookup table - gantry angles

      ga = fltarr(360)
265
      ga(0) = 0.06
      ga(1) = 1.04
      ga(2) = 2.06
      ga(3) = 3.07
270   ga(4) = 4.05
      ga(5) = 5.05
      ga(6) = 6.03
      ga(7) = 7.06
      ga(8) = 8.06
275   ga(9) = 9.00
      ga(10) = 10.06
      ga(11) = 11.05
      ga(12) = 12.07
      ga(13) = 13.01
280   ga(14) = 14.03
      ga(15) = 15.05
      ga(16) = 16.08
      ga(17) = 17.02
      ga(18) = 18.06
285   ga(19) = 19.06
      ga(20) = 20.03
      ga(21) = 21.05
      ga(22) = 22.01
      ga(23) = 23.05
290   ga(24) = 24.04
      ga(25) = 25.02
      ga(26) = 26.02
      ga(27) = 27.04
      ga(28) = 28.03
295   ga(29) = 28.99
      ga(30) = 29.99
```

```
      ga(31) = 31.01
      ga(32) = 32.02
      ga(33) = 33.02
300   ga(34) = 33.98
      ga(35) = 35.02
      ga(36) = 36.02
      ga(37) = 36.99
      ga(38) = 38.01
305   ga(39) = 38.99
      ga(40) = 40.03
      ga(41) = 41.00
      ga(42) = 42.00
      ga(43) = 43.00
310   ga(44) = 44.00
      ga(45) = 44.99
      ga(46) = 45.99
      ga(47) = 46.95
      ga(48) = 47.93
315   ga(49) = 48.98
      ga(50) = 49.96
      ga(51) = 51.00
      ga(52) = 51.98
      ga(53) = 52.95
320   ga(54) = 53.99
      ga(55) = 54.95
      ga(56) = 55.95
      ga(57) = 56.96
      ga(58) = 57.98
325   ga(59) = 58.96
      ga(60) = 59.96
      ga(61) = 60.96
      ga(62) = 61.93
      ga(63) = 62.93
330   ga(64) = 63.91
      ga(65) = 64.95
      ga(66) = 65.92
      ga(67) = 66.94
      ga(68) = 67.92
335   ga(69) = 68.96
      ga(70) = 69.97
      ga(71) = 70.93
      ga(72) = 71.95
      ga(73) = 72.93
340   ga(74) = 73.92
      ga(75) = 74.94
      ga(76) =75.90
      ga(77) =76.94
      ga(78) =77.89
345   ga(79) =78.89
      ga(80) =79.89
      ga(81) =80.91
      ga(82) =81.88
      ga(83) =82.90
350   ga(84) =83.88
      ga(85) =84.88
      ga(86) =85.89
      ga(87) =86.89
      ga(88) =87.87
355   ga(89) =88.89
      ga(90) =89.89
      ga(91) =90.90
      ga(92) =91.88
      ga(93) =92.88
360   ga(94) =93.88
      ga(95) =94.89
      ga(96) =95.87
      ga(97) =96.87
      ga(98) =97.87
365   ga(99) =98.88
      ga(100) =99.88
      ga(101) =100.90
      ga(102) =101.90
      ga(103) =102.87
370   ga(104) =103.87
```

```
      ga(105) =104.83
      ga(106) =105.85
      ga(107) =106.89
      ga(108) =107.90
375   ga(109) =108.84
      ga(110) =109.86
      ga(111) =110.90
      ga(112) =111.87
      ga(113) =112.85
380   ga(114) =113.85
      ga(115) =114.85
      ga(116) =115.82
      ga(117) =116.84
      ga(118) =117.82
385   ga(119) =118.86
      ga(120) =119.83
      ga(121) =120.83
      ga(122) =121.85
      ga(123) =122.81
390   ga(124) =123.84
      ga(125) =124.82
      ga(126) =125.80
      ga(127) =126.82
      ga(128) =127.83
395   ga(129) =128.83
      ga(130) =129.79
      ga(131) =130.81
      ga(132) =131.81
      ga(133) =132.84
400   ga(134) =133.86
      ga(135) =134.80
      ga(136) =135.82
      ga(137) =136.81
      ga(138) =137.81
405   ga(139) =138.79
      ga(140) =139.81
      ga(141) =140.82
      ga(142) =141.80
      ga(143) =142.82
410   ga(144) =143.86
      ga(145) =144.79
      ga(146) =145.81
      ga(147) =146.83
      ga(148) =147.79
415   ga(149) =148.81
      ga(150) =149.82
      ga(151) =150.82
      ga(152) =151.82
      ga(153) =152.80
420   ga(154) =153.79
      ga(155) =154.81
      ga(156) =155.81
      ga(157) =156.83
      ga(158) =157.82
425   ga(159) =158.86
      ga(160) =159.80
      ga(161) =160.82
      ga(162) =161.85
      ga(163) =162.85
430   ga(164) =163.81
      ga(165) =164.77
      ga(166) =165.80
      ga(167) =166.80
      ga(168) =167.80
435   ga(169) =168.82
      ga(170) =169.80
      ga(171) =170.81
      ga(172) =171.79
      ga(173) =172.79
440   ga(174) =173.81
      ga(175) =174.82
      ga(176) =175.82
      ga(177) =176.84
      ga(178) =177.80
```

```
      ga(179) =178.81
      ga(180) =179.81
      ga(181) =180.96
      ga(182) =181.86
      ga(183) =182.83
      ga(184) =183.83
      ga(185) =184.83
      ga(186) =185.83
      ga(187) =186.81
      ga(188) =187.82
      ga(189) =188.82
      ga(190) =189.84
      ga(191) =190.82
      ga(192) =191.94
      ga(193) =192.81
      ga(194) =193.85
      ga(195) =194.81
      ga(196) =195.86
      ga(197) =196.82
      ga(198) =197.86
      ga(199) =198.80
      ga(200) =199.85
      ga(201) =200.81
      ga(202) =201.91
      ga(203) =202.87
      ga(204) =203.87
      ga(205) =204.90
      ga(206) =205.90
      ga(207) =206.88
      ga(208) =207.79
      ga(209) =208.89
      ga(210) =209.85
      ga(211) =210.81
      ga(212) =211.85
      ga(213) =212.88
      ga(214) =213.88
      ga(215) =214.88
      ga(216) =215.86
      ga(217) =216.85
      ga(218) =217.91
      ga(219) =218.87
      ga(220) =219.89
      ga(221) =220.89
      ga(222) =221.88
      ga(223) =222.90
      ga(224) =223.88
      ga(225) =224.88
      ga(226) =225.91
      ga(227) =226.89
      ga(228) =227.91
      ga(229) =228.89
      ga(230) =229.90
      ga(231) =230.92
      ga(232) =231.90
      ga(233) =232.90
      ga(234) =233.88
      ga(235) =234.91
      ga(236) =235.89
      ga(237) =236.91
      ga(238) =237.91
      ga(239) =238.94
      ga(240) =239.96
      ga(241) =240.94
      ga(242) =241.92
      ga(243) =242.91
      ga(244) =243.91
      ga(245) =244.91
      ga(246) =245.93
      ga(247) =249.97
      ga(248) =247.96
      ga(249) =248.94
      ga(250) =249.96
      ga(251) =250.94
      ga(252) =251.97
```

```
      ga(253) =252.95
520   ga(254) =253.95
      ga(255) =254.95
      ga(256) =255.97
      ga(257) =256.94
      ga(258) =257.98
525   ga(259) =258.94
      ga(260) =259.96
      ga(261) =260.95
      ga(262) =261.95
      ga(263) =262.97
530   ga(264) =263.97
      ga(265) =264.96
      ga(266) =265.96
      ga(267) =266.98
      ga(268) =267.94
535   ga(269) =268.95
      ga(270) =270.01
      ga(271) =270.99
      ga(272) =271.99
      ga(273) =272.98
540   ga(274) =273.98
      ga(275) =275.00
      ga(276) =275.98
      ga(277) =276.95
      ga(278) =278.05
545   ga(279) =279.03
      ga(280) =280.03
      ga(281) =281.01
      ga(282) =282.00
      ga(283) =282.98
550   ga(284) =283.98
      ga(285) =285.00
      ga(286) =286.02
      ga(287) =286.99
      ga(288) =288.01
555   ga(289) =289.03
      ga(290) =290.01
      ga(291) =291.02
      ga(292) =292.04
      ga(293) =293.04
560   ga(294) =294.04
      ga(295) =295.01
      ga(296) =296.03
      ga(297) =297.05
      ga(298) =298.05
565   ga(299) =299.04
      ga(300) =300.02
      ga(301) =301.04
      ga(302) =302.04
      ga(303) =303.03
570   ga(304) =304.07
      ga(305) =305.07
      ga(306) =306.07
      ga(307) =307.05
      ga(308) =308.08
575   ga(309) =309.10
      ga(310) =310.08
      ga(311) =311.06
      ga(312) =312.09
      ga(313) =313.05
580   ga(314) =314.07
      ga(315) =315.07
      ga(316) =316.07
      ga(317) =317.06
      ga(318) =318.06
585   ga(319) =319.08
      ga(320) =320.08
      ga(321) =321.07
      ga(322) =322.09
      ga(323) =323.05
590   ga(324) =324.05
      ga(325) =325.06
      ga(326) =326.08
```

```
      ga(327) =327.08
      ga(328) =328.06
595   ga(329) =329.05
      ga(330) =330.09
      ga(331) =331.07
      ga(332) =332.09
      ga(333) =333.07
600   ga(334) =334.10
      ga(335) =335.10
      ga(336) =336.08
      ga(337) =337.10
      ga(338) =338.11
605   ga(339) =339.05
      ga(340) =340.09
      ga(341) =341.05
      ga(342) =342.10
      ga(343) =343.12
610   ga(344) =344.08
      ga(345) =345.10
      ga(346) =346.09
      ga(347) =347.09
      ga(348) =348.05
615   ga(349) =349.05
      ga(350) =350.11
      ga(351) =351.10
      ga(352) =352.10
      ga(353) =353.06
620   ga(354) =354.10
      ga(355) =355.09
      ga(356) =356.05
      ga(357) =357.03
      ga(358) =358.07
625   ga(359) =359.04
      ;_____________________________________________________________

      ;            Lookup table - detector offset

630
      ; AB direction

      doff = fltarr(82)

635   ;      0 tot 120 grade

      doff(0) = 1
      doff(1) = 1
      doff(2) = 0
640   doff(3) = -1
      doff(4) = 1
      doff(5) = 1
      doff(6) = 2
      doff(7) = 2
645   doff(8) = 3
      doff(9) = 2
      doff(10) = 2
      doff(11) = 1
      doff(12) = 1
650   doff(13) = 0
      doff(14) = 0
      doff(15) = 1
      doff(16) = 1
      doff(17) = 3
655   doff(18) = 2
      doff(19) = 1
      doff(20) = 0
      doff(21) = 1
      doff(22) = 0
660   doff(23) = 0
      doff(24) = 0
      doff(25) = 0
      doff(26) = 1
      doff(27) = 2
665   doff(28) = 2
      doff(29) = 1
```

```
      doff(30) = 1
      doff(31) = 0
      doff(32) = -1
670   doff(33) = -1
      doff(34) = 0
      doff(35) = 0
      doff(36) = 1
      doff(37) = 1
675   doff(38) = 1
      doff(39) = -1
      doff(40) = 0


680   ; -120 tot 0 grade

      doff(41) = 0
      doff(42) = 0
      doff(43) = 0
685   doff(44) = 0
      doff(45) = 0
      doff(46) = 1
      doff(47) = 1
      doff(48) = 2
690   doff(49) = 2
      doff(50) = 2
      doff(51) = 1
      doff(52) = 1
      doff(53) = 1
695   doff(54) = 1
      doff(55) = 2
      doff(56) = 2
      doff(57) = 3
      doff(58) = 4
700   doff(59) = 4
      doff(60) = 2
      doff(61) = 3
      doff(62) = 2
      doff(63) = 2
705   doff(64) = 2
      doff(65) = 3
      doff(66) = 2
      doff(67) = 3
      doff(68) = 4
710   doff(69) = 4
      doff(70) = 3
      doff(71) = 4
      doff(72) = 3
      doff(73) = 2
715   doff(74) = 2
      doff(75) = 2
      doff(76) = 3
      doff(77) = 3
      doff(78) = 4
720   doff(79) = 4
      doff(80) = 3
      doff(81) = 2


725   ; GT direction

      doffv = fltarr(82)

      ; 0 tot 120 grade
730
      doffv(0) = 0
      doffv(1) = 0
      doffv(2) = 0
      doffv(3) = 0
735   doffv(4) = -1
      doffv(5) = 0
      doffv(6) = 0
      doffv(7) = 0
      doffv(8) = 0
740   doffv(9) = 0
```

```
      doffv(10) = 0
      doffv(11) = 0
      doffv(12) = 1
      doffv(13) = 0
745   doffv(14) = 0
      doffv(15) = 0
      doffv(16) = 1
      doffv(17) = 1
      doffv(18) = 1
750   doffv(19) = 0
      doffv(20) = 1
      doffv(21) = 0
      doffv(22) = 1
      doffv(23) = 1
755   doffv(24) = 1
      doffv(25) = 1
      doffv(26) = 1
      doffv(27) = 1
      doffv(28) = 1
760   doffv(29) = 2
      doffv(30) = 2
      doffv(31) = 2
      doffv(32) = 2
      doffv(33) = 2
765   doffv(34) = 2
      doffv(35) = 3
      doffv(36) = 2
      doffv(37) = 2
      doffv(38) = 2
770   doffv(39) = 2
      doffv(40) = 3

      ;     -120 tot 0 grade

775   doffv(41) = 5
      doffv(42) = 4
      doffv(43) = 4
      doffv(44) = 4
      doffv(45) = 5
780   doffv(46) = 4
      doffv(47) = 4
      doffv(48) = 3
      doffv(49) = 4
      doffv(50) = 3
785   doffv(51) = 4
      doffv(52) = 3
      doffv(53) = 3
      doffv(54) = 2
      doffv(55) = 3
790   doffv(56) = 3
      doffv(57) = 3
      doffv(58) = 3
      doffv(59) = 2
      doffv(60) = 2
795   doffv(61) = 2
      doffv(62) = 2
      doffv(63) = 2
      doffv(64) = 2
      doffv(65) = 1
800   doffv(66) = 1
      doffv(67) = 1
      doffv(68) = 1
      doffv(69) = 1
      doffv(70) = 1
805   doffv(71) = 0
      doffv(72) = 0
      doffv(73) = 0
      doffv(74) = -1
      doffv(75) = 0
810   doffv(76) = 0
      doffv(77) = 0
      doffv(78) = 0
      doffv(79) = -1
      doffv(80) = 0
```

```
815   doffv(81) = 0

      ;  detector rotation correction

      drot = fltarr(82)
820
      drot(0) = -0.02
      drot(1) = -0.14
      drot(2) = -0.07
      drot(3) = -0.04
825   drot(4) = 0.00
      drot(5) = 0.02
      drot(6) = 0.03
      drot(7) = -0.07
      drot(8) = -0.1
830   drot(9) = -0.12
      drot(10) = -0.16
      drot(11) = -0.14
      drot(12) = -0.25
      drot(13) = -0.05
835   drot(14) = 0.02
      drot(15) = -0.06
      drot(16) = -0.07
      drot(17) = -0.11
      drot(18) = -0.15
840   drot(19) = -0.12
      drot(20) = -0.21
      drot(21) = -0.08
      drot(22) = -0.13
      drot(23) = -0.01
845   drot(24) = -0.30
      drot(25) = -0.15
      drot(26) = -0.21
      drot(27) = -0.19
      drot(28) = -0.22
850   drot(29) = -0.10
      drot(30) = -0.12
      drot(31) = -0.17
      drot(32) = -0.22
      drot(33) = -0.20
855   drot(34) = -0.19
      drot(35) = -0.12
      drot(36) = -0.07
      drot(37) = -0.14
      drot(38) = -0.18
860   drot(39) = -0.24
      drot(40) = -0.17


      ; -120 tot 0 grade
865
      drot(41) = -0.15
      drot(42) = -0.12
      drot(43) = -0.07
      drot(44) = -0.02
870   drot(45) = -0.05
      drot(46) = -0.04
      drot(47) = -0.11
      drot(48) = -0.02
      drot(49) = -0.11
875   drot(50) = -0.05
      drot(51) = 0.12
      drot(52) = 0.06
      drot(53) = -0.07
      drot(54) = 0.00
880   drot(55) = 0.05
      drot(56) = 0.20
      drot(57) = 0.06
      drot(58) = 0.02
      drot(59) = 0.06
885   drot(60) = 0.03
      drot(61) = 0.12
      drot(62) = 0.03
      drot(63) = 0.21
```

```
      drot(64) = 0.12
890   drot(65) = 0.24
      drot(66) = 0.16
      drot(67) = 0.00
      drot(68) = -0.01
      drot(69) = -0.13
895   drot(70) = 0.09
      drot(71) = -0.07
      drot(72) = 0.10
      drot(73) = 0.03
      drot(74) = -0.08
900   drot(75) = 0.14
      drot(76) = 0.01
      drot(77) = 0.02
      drot(78) = 0.16
      drot(79) = 0.10
905   drot(80) = 0.01
      drot(81) = -0.06


910   ; gantry angles

      gadoff = fltarr(82)

      gadoff(0) = 0
915   gadoff(1) = 3
      gadoff(2) = 6
      gadoff(3) = 9
      gadoff(4) = 12
      gadoff(5) = 15
920   gadoff(6) = 18
      gadoff(7) = 21
      gadoff(8) = 24
      gadoff(9) = 27
      gadoff(10) = 30
925   gadoff(11) = 33
      gadoff(12) = 36
      gadoff(13) = 39
      gadoff(14) = 42
      gadoff(15) = 45
930   gadoff(16) = 48
      gadoff(17) = 51
      gadoff(18) = 54
      gadoff(19) = 57
      gadoff(20) = 60
935   gadoff(21) = 63
      gadoff(22) = 66
      gadoff(23) = 69
      gadoff(24) = 72
      gadoff(25) = 75
940   gadoff(26) = 78
      gadoff(27) = 81
      gadoff(28) = 84
      gadoff(29) = 87
      gadoff(30) = 90
945   gadoff(31) = 94
      gadoff(32) = 97
      gadoff(33) = 100
      gadoff(34) = 103
      gadoff(35) = 106
950   gadoff(36) = 109
      gadoff(37) = 112
      gadoff(38) = 115
      gadoff(39) = 118
      gadoff(40) = 120
955   gadoff(41) = 240
      gadoff(42) = 243
      gadoff(43) = 246
      gadoff(44) = 249
      gadoff(45) = 252
960   gadoff(46) = 255
      gadoff(47) = 258
      gadoff(48) = 261
```

```
      gadoff(49) = 264
      gadoff(50) = 267
965   gadoff(51) = 270
      gadoff(52) = 273
      gadoff(53) = 276
      gadoff(54) = 279
      gadoff(55) = 282
970   gadoff(56) = 285
      gadoff(57) = 288
      gadoff(58) = 291
      gadoff(59) = 294
      gadoff(60) = 297
975   gadoff(61) = 300
      gadoff(62) = 303
      gadoff(63) = 306
      gadoff(64) = 309
      gadoff(65) = 312
980   gadoff(66) = 315
      gadoff(67) = 318
      gadoff(68) = 321
      gadoff(69) = 324
      gadoff(70) = 327
985   gadoff(71) = 330
      gadoff(72) = 333
      gadoff(73) = 336
      gadoff(74) = 339
      gadoff(75) = 342
990   gadoff(76) = 345
      gadoff(77) = 348
      gadoff(78) = 351
      gadoff(79) = 354
      gadoff(80) = 357
995   gadoff(81) = 360



1000  ;_____________________________________________________________


      hh1 = fltarr(512)

1005  for hoogte = 128,128 do begin

      for j = 0,194 do begin


1010  if j le 97 then filename = 'jim'+strcompress(j+263)+'.tif'
      if j gt 97 then filename = 'jim'+strcompress(j-97)+'.tif'


      if j lt 97 then gantryangle = ga(j+263)
1015  if j ge 97 then gantryangle = ga(j-97)

      ;print, gantryangle


1020  filename1 = strcompress(filename)

      ;print, filename1

      filename2 =strmid(filename1, 0, 3)
1025
      ;print, filename2

      filename3 = strmid(filename, 4)

1030  ;print, filename3


      filename4 = filename2 + filename3

1035  ;print, filename4
      ;stop
```

```
      ;print,gantryangle,filename4

      beeld = filepath(filename4, subdirectory = ['examples','jimmy'])
1040  openr, unit, beeld, /get_lun
      readu, unit, header
      readu, unit, result
      free_lun, unit

1045

      result = rot(result,3)

      ;window, xsize = 1024, ysize = 1024
      ;tvscl, result
1050  ;stop

      ;_____________________________________________________________________
      ;                  Korreksie vir isosenter - Winston Lutz
      ;_____________________________________________________________________
1055

      ;iindex = 0

      ;for dd = 0,7 do begin
1060
      ;if (gantryangle gt angles(dd)) and (gantryangle le angles(dd+1)) then iindex = dd

      ;endfor

1065  ;dd = iindex

      ;slope = (shifta(dd+1) - shifta(dd)) / (angles(dd+1) - angles(dd))
      ;interc = shifta(dd) - (slope*angles(dd))
      ;shf = (slope*gantryangle) + interc
1070  ;shf = -1*shf
      ;shf = round(shf/(410.0/1024.0))

      ;for d1 = 0,980 do begin
      ;for e1 = 0,1023 do begin
1075
      ;result1b(d1+30,e1) = result(d1+shf+30,e1)

      ;endfor
      ;endfor
1080
      ;print, shf
      ;_____________________________GT_____________________________

      ;slope = (shiftg(dd+1) - shiftg(dd)) / (angles(dd+1) - angles(dd))
1085  ;interc = shiftg(dd) - (slope*angles(dd))
      ;shfg = (slope*gantryangle) + interc
      ;shfg = -1*shfg
      ;shfg = round(shf/(410.0/1024.0))

1090  ;for d1 = 0,1023 do begin

      ;for e1 = 0,960 do begin

      ;result1c(d1,e1+30) = result1b(d1,e1+30+shfg)
1095
      ;endfor
      ;endfor

      ;print, shfg
1100  ;_____________________________________________________________________

      ;result = result1c

      ;result2 = rotate(result, 2)
1105
      ;_____________________________________________________________________

      ;                  Detector offset corrections - Piercing point

1110
```

```
;_____ AB _____

iindex = 0
for dd = 0,80 do begin
if gantryangle gt 120 and gantryangle lt 240 then gantryangle = 240
if (gantryangle ge gadoff(dd)) and (gantryangle le gadoff(dd+1)) then iindex = dd
endfor

;print, gantryangle, iindex

slope = (doff(iindex+1) - doff(iindex)) / (gadoff(iindex+1) - gadoff(iindex))
interc = doff(iindex) - (slope*gadoff(iindex))
shf = ((slope*gantryangle) + interc)
;shf = round(shf)

for d1 = 0,980 do begin
for e1 = 0,1023 do begin
result1b(d1+30,e1) = result(d1+shf+30,e1)
endfor
endfor

;_____GT_____

slope = (doffv(iindex+1) - doffv(iindex)) / (gadoff(iindex+1) - gadoff(iindex))
interc = doffv(iindex) - (slope*gadoff(iindex))
shfg = ((slope*gantryangle) + interc)
;shfg = -1*shfg
;shfg = round(shf)

for d1 = 0,1023 do begin
for e1 = 0,960 do begin
result1c(d1,e1+30) = result1b(d1,e1+30+shfg)
endfor
endfor

result = result1c

;_____Correction for detector rotation_____

;slope = (drot(iindex+1) - drot(iindex)) / (gadoff(iindex+1) - gadoff(iindex))
;interc = drot(iindex) - (slope*gadoff(iindex))
;rotation = ((slope*gantryangle) + interc)

;result1ww = rotate(result, rotation)
result1ww = result1c
;_____

result2 = rotate(result1ww, 2)
```

```
;window, 1, xsize = 1024, ysize = 1024
;tvscl, result2
;stop
;_____________________________________________________________________

;                    4 rye bymekaar = 1.6mm snitte

;_____________________________________________________________________

result3 = fltarr(1024)
result33 = fltarr(256)
result3a = fltarr(1024,256)
result3aa= fltarr(256,256)


for rr = 0,1023,4 do begin

result3 = total(result2(*,rr:rr+3),2)

result3a(*,rr/4) = result3


endfor


for rr2 = 0,1023,4 do begin

result33 = total(result3a(rr2:rr2+3,*),1)

result3aa(rr2/4,*) = result33


endfor

;window, 1, xsize = 256, ysize = 256
;tvscl, result3aa
;stop


;_____________________________________________________________________

result1 = result3aa


;_____________________________________
;          Bepaling van U,p,p'

;_____________________________________

j2 = (gantryangle) * !dtor

for m3  = 0,255 do begin
for n3 = 0,255 do begin

UU = (DP + (q3(m3,n3) * (sin ((j2) - qq3(m3,n3))))) / DP

pa1 = q3(m3,n3) * cos ((j2 - qq3(m3,n3)) )
pa2 =  DP + (q3(m3,n3) * sin ((j2 - qq3(m3,n3))))
pa3 = DP * (pa1 / pa2)

p = (pa3*DP)/(DP+DE)

U3(m3,n3) = UU                                          ; U waarde
Pa(m3,n3) = pa3 + 128                                   ; p' waarde
P3(m3,n3) = p                                           ; p waarde

endfor
endfor

;_____________________________________

;            Modified projection
;_____________________________________
```

```
1260  modry = fltarr(256)

      Pa1 = P3(*,hoogte)
      result1a = result1(*,hoogte)
      hh1 = hh(*,hoogte)
1265
      ;sino2(*,j) = result1a(*)                                          ;sinogram

      for f = 0,255 do begin

1270  mr = dp / sqrt((dp*dp) + (Pa1(f))^2 + (hh1(f))^2)                  ;modification factor

      modry(f) = mr

      endfor
1275
      conepr = fltarr(256)

      for r = 0,255 do begin

1280  conepr(r) = result1a(r) * modry(r)

      endfor

      ;print, conepr
1285  ;stop

      ;_____________________________________________________________________

      ;                          Convolution with filter
1290
      ;_____________________________________________________________________


1295  filtered = fltarr(256)

      ;FDI = fft(conepr,-1)


1300
      filtered = convol(conepr,s)

      ;filtered = convol(s, LPC)

1305

      ;filtered = fft(FDI*fx,1)


1310  ;plot,filtered
      ;stop


      ;_____________________________________________
1315  ;
      ;            Interpolasie
      ;
      ;_____________________________________________

1320  resultaat = fltarr(256,256)


      for jc = 0,255 do begin
      for i = 0,255 do begin
1325
      pixel1 = Pa(i,jc)

      resultaat(i,jc) = interpolate(filtered ,pixel1)

1330  bpj(i,jc) = resultaat(i,jc)  *  (1/(U3(i,jc))^2)

      endfor
```

```
      endfor
1335  finaal = finaal + bpj


      endfor
1340


      ;finaal = congrid(finaal, 800,800)

1345
      endfor

      window,1

1350  tvscl, finaal

      write_tiff, 'C:\RSI\IDL52\examples\reconbeelddegrot3.tiff',tvrd()

      stop
1355


      tlb = widget_base(title = 'Reconstruction',/column)
      base1 = widget_base(tlb, /row)
1360  draw = widget_draw(tlb, xsize = 800, ysize = 800)
      xslider = widget_slider(tlb, min = 0 , max = 255, value = 125, title = 'Lower Level', event_pro =
      zslider = widget_slider(tlb, min = 0 , max = 255, value = 125, title = 'Upper Level', event_pro =
      button = widget_button(tlb, value = 'Exit', event_pro = 'mywidget_exit')

1365  widget_control, tlb, /realize
      widget_control, draw, get_value = draw_index
      wset, draw_index
      data = finaal
      tvscl ,finaal
1370
      state = {xslider:xslider,zslider:zslider, data:data,finaal: finaal}
      widget_control, tlb, set_uvalue = state

      xmanager, 'cbct2a', tlb
1375
      ;openw, unit, 'c:\RSI\IDL52\examples\cbbpj',/get_lun
      ;writeu,unit,volume
      ;free_lun,unit

1380
     end
```

Appendix B: IDL source code, geometric calibration

```
pro geomfannuut17

header = uintarr(180)
result = uintarr(1024,1024)
gemax = fltarr(24)
gembx = fltarr(24)

gemax(*) = 0.0
gembx(*) = 0.0

beeldnr = 1

filename1 = 'geom' + strcompress(beeldnr) +'.tif'

filename2 = strmid(filename1,0,4)

filename3 =strmid(filename1, 5,6)                                    ; onder 100

;filename3 =strmid(filename1, 5,7)                                    ; bo 100

filename = filename2+filename3



beeld = filepath(filename, subdirectory = ['examples','geometrie fantoom','2'])                    ;
;beeld = filepath(filename, subdirectory = ['examples','geometrie fantoom','3'])
openr, unit, beeld, /get_lun
readu, unit, header
readu, unit, result
free_lun, unit


;result = congrid(result, 800,800)

window, xsize = 1024 ,ysize = 1024
tvscl, result


text = dialog_message('Do you want to define new ellips coordinates?',/question)

if text eq 'Yes' then begin
goto, nuwekoord
endif

if text eq 'No' then begin
goto, ellipskoordinate
endif

nuwekoord:

w = fltarr(25)
r = fltarr(25)
count = 0

cursor,x,y,1, /device, /down

while(!mouse.button ne 4) do begin

cursor,x1,y1,1,/device, /down


xp15 = x1+20
xm15 = x1-20
yp15 = y1+20
ym15 = y1-20

PLOTS, [xm15,xp15], [ym15,ym15], COLOR=12, /DEVICE
PLOTS, [xm15,xp15], [yp15,yp15], COLOR=12, /DEVICE
PLOTS, [xm15,xm15], [yp15,ym15], COLOR=12, /DEVICE
PLOTS, [xp15,xp15], [ym15,yp15], COLOR=12, /DEVICE

w(count) = x1
r(count) = y1
count = count+1
```

```
75
      endwhile

      ;_____________________________________________________________________

80
      profiel = fltarr(31)
      agtergrond = fltarr(31)
      verskil = fltarr(31,31)

85    for bb = 0,23 do begin

      xa = w[bb]                                    ; BB
      ya = r[bb]

90    result1a = result(xa - 7:xa +7, ya - 7:ya + 7)


      maksi = 0.00

95    for ry1 = 0,14 do begin
      for kolom1  = 0,14 do begin

      if result1a(ry1,kolom1) ge maksi then begin

100   maksi = result1a(ry1,kolom1)
      xindex = ry1
      yindex = kolom1

      endif
105
      endfor
      endfor

      print, xindex, yindex
110

      xori =  (xa-7) + xindex
      yori =  (ya - 7) + yindex

115   ;print, xori,yori

      gemax(bb) = xori
      gembx(bb) = yori

120   PLOTS, [xori,xori], [yori-30,yori+30], COLOR=255, /DEVICE
      PLOTS, [xori+30,xori-30], [yori,yori], COLOR=255, /DEVICE


      endfor
125


      openw, lun, 'c:/RSI/IDL52/examples/ellipskoordm0.dat',/GET_LUN
      writeu, lun, gemax
130   writeu, lun, gembx
      free_lun, lun


      ellipskoordinate:
135
      openr, lun, 'c:/RSI/IDL52/examples/ellipskoordm0.dat',/GET_LUN
      readu, lun, gemax
      readu, lun, gembx
      free_lun, lun
140
      print, gemax
      print, gembx

      ;gemax = [126.629,162.449,305.303,516.288,724.077,861.136,894.780,829.562,691.776,515.538,337.178,
145   ;gembx = [832.816,848.545,859.690,862.037,854.621,840.400,824.290,810.701,802.438,800.820,806.072,


      ;gemax = [236.972,270.784,407.678,613.840,821.535,961.175,995.923,929.251,789.661,613.951,439.314,
```

```
;gembx = [724.188,740.233,753.728,759.896,756.254,744.292,728.436,713.490,702.920,698.583,701.109,
;for pp = 0,23 do begin

;nuwex = float(randomu(seed)) - 6
;nuwey = float(randomu(seed)) - 6

;gemax(pp) = gemax(pp) + nuwex
;gembx(pp) = gembx(pp) + nuwey

;endfor


;print, gemax
;print, gembx

;_____________________________________________________________________

;              Lyne vir piercing point

;PLOTS, [gemax[0],gemax[18]], [gembx[0],gembx[18]], COLOR=12, /DEVICE
;PLOTS, [gemax[1],gemax[19]], [gembx[1],gembx[19]], COLOR=12, /DEVICE
;PLOTS, [gemax[2],gemax[20]], [gembx[2],gembx[20]], COLOR=12, /DEVICE
;PLOTS, [gemax[3],gemax[21]], [gembx[3],gembx[21]],COLOR=12, /DEVICE
;PLOTS, [gemax[4],gemax[22]], [gembx[4],gembx[22]], COLOR=12, /DEVICE
;PLOTS, [gemax[5],gemax[23]], [gembx[5],gembx[23]], COLOR=12, /DEVICE

;PLOTS, [gemax[6],gemax[12]], [gembx[6],gembx[12]], COLOR=12, /DEVICE
;PLOTS, [gemax[7],gemax[13]], [gembx[7],gembx[13]], COLOR=12, /DEVICE
;PLOTS, [gemax[8],gemax[14]], [gembx[8],gembx[14]], COLOR=12, /DEVICE
;PLOTS, [gemax[9],gemax[15]], [gembx[9],gembx[15]], COLOR=12, /DEVICE
;PLOTS, [gemax[10],gemax[16]], [gembx[10],gembx[16]], COLOR=12, /DEVICE
;PLOTS, [gemax[11],gemax[17]], [gembx[11],gembx[17]], COLOR=12, /DEVICE

;stop
;_____________________________________________________________________

;              Berekening van ellips parameters

;_____________________________________________________________________


;    a(u-u0)^2 +b(v-v0)^2 +2c(u-u0)(v-v0) = 1       ellips vergelyking

;   Oplossing Appendix A

;   p0(u)^2 - 2p1(u)-2p2(v)+2p3(uv) + p4 = -v^2


A1a = [[(gemax[0])^2,-2*(gemax[0]), -2*(gembx[0]), 2*(gemax[0]*gembx[0]), 1.0], $
       [(gemax[2])^2,-2*(gemax[2]), -2*(gembx[2]), 2*(gemax[2]*gembx[2]), 1.0], $
       [(gemax[4])^2,-2*(gemax[4]), -2*(gembx[4]), 2*(gemax[4]*gembx[4]), 1.0], $
       [(gemax[6])^2,-2*(gemax[6]), -2*(gembx[6]), 2*(gemax[6]*gembx[6]), 1.0], $
       [(gemax[9])^2,-2*(gemax[9]), -2*(gembx[9]), 2*(gemax[9]*gembx[9]), 1.0]]

A1b =[[(gemax[11])^2,-2*(gemax[11]), -2*(gembx[11]), 2*(gemax[11]*gembx[11]), 1.0], $
       [(gemax[9])^2,-2*(gemax[9]), -2*(gembx[9]), 2*(gemax[9]*gembx[9]), 1.0], $
       [(gemax[7])^2,-2*(gemax[7]), -2*(gembx[7]), 2*(gemax[7]*gembx[7]), 1.0], $
       [(gemax[4])^2,-2*(gemax[4]), -2*(gembx[4]), 2*(gemax[4]*gembx[4]), 1.0], $
       [(gemax[2])^2,-2*(gemax[2]), -2*(gembx[2]), 2*(gemax[2]*gembx[2]), 1.0]]


B1a = [-(gembx[0])^2, -(gembx[2])^2, -(gembx[4])^2, -(gembx[6])^2, -(gembx[9])^2]

B1b = [-(gembx[11])^2, -(gembx[9])^2, -(gembx[7])^2, -(gembx[4])^2, -(gembx[2])^2]



A2a = [[(gemax[12])^2,-2*(gemax[12]), -2*(gembx[12]), 2*(gemax[12]*gembx[12]), 1.0], $
       [(gemax[14])^2,-2*(gemax[14]), -2*(gembx[14]), 2*(gemax[14]*gembx[14]), 1.0], $
       [(gemax[16])^2,-2*(gemax[16]), -2*(gembx[16]), 2*(gemax[16]*gembx[16]), 1.0], $
```

```
          [(gemax[18])^2,-2*(gemax[18]), -2*(gembx[18]), 2*(gemax[18]*gembx[18]), 1.0], $
          [(gemax[21])^2,-2*(gemax[21]), -2*(gembx[21]), 2*(gemax[21]*gembx[21]), 1.0]]
225
    A2b = [[(gemax[23])^2,-2*(gemax[23]), -2*(gembx[23]), 2*(gemax[23]*gembx[23]), 1.0], $
          [(gemax[21])^2,-2*(gemax[21]), -2*(gembx[21]), 2*(gemax[21]*gembx[21]), 1.0], $
          [(gemax[19])^2,-2*(gemax[19]), -2*(gembx[19]), 2*(gemax[19]*gembx[19]), 1.0], $
          [(gemax[16])^2,-2*(gemax[16]), -2*(gembx[16]), 2*(gemax[16]*gembx[16]), 1.0], $
230       [(gemax[14])^2,-2*(gemax[14]), -2*(gembx[14]), 2*(gemax[14]*gembx[14]), 1.0]]


    B2a = [-(gembx[12])^2, -(gembx[14])^2, -(gembx[16])^2, -(gembx[18])^2, -(gembx[21])^2]

235 B2b = [-(gembx[23])^2, -(gembx[21])^2, -(gembx[19])^2, -(gembx[16])^2, -(gembx[14])^2]


    LUDC, A1a , INDEX1a

240 oplossing1a = Lusol(A1a, INDEX1a, B1a)

    ;print, 'Matriks oplossing 1a:'
    ;print, oplossing1a

245 LUDC, A1b , INDEX1b

    oplossing1b = Lusol(A1b, INDEX1b, B1b)

    ;print, 'Matriks oplossing 1b:'
250 ;print, oplossing1b


    LUDC, A2a , INDEX2a

255 oplossing2a = Lusol(A2a, INDEX2a, B2a)

    ;print, 'Matriks oplossing 2a:'
    ;print, oplossing2a

260 LUDC, A2b , INDEX2b

    oplossing2b = Lusol(A2b, INDEX2b, B2b)

    ;print, 'Matriks oplossing 2b:'
265 ;print, oplossing2b


    p0_1a = oplossing1a(0)
    p1_1a = oplossing1a(1)
270 p2_1a = oplossing1a(2)
    p3_1a = oplossing1a(3)
    p4_1a = oplossing1a(4)

    u0_1a = (p1_1a-(p2_1a*p3_1a))/(p0_1a-((p3_1a)^2))
275 v0_1a = ((p0_1a*p2_1a) -(p1_1a*p3_1a))/(p0_1a-(p3_1a)^2)
    aelp_1a = p0_1a/((p0_1a*((u0_1a)^2))+((v0_1a)^2)+(2*p3_1a*u0_1a*v0_1a)-p4_1a)
    belp_1a = aelp_1a/p0_1a
    celp_1a = p3_1a*belp_1a

280 p0_1b = oplossing1b(0)
    p1_1b = oplossing1b(1)
    p2_1b = oplossing1b(2)
    p3_1b = oplossing1b(3)
    p4_1b = oplossing1b(4)
285
    u0_1b = (p1_1b-(p2_1b*p3_1b))/(p0_1b-((p3_1b)^2))
    v0_1b = ((p0_1b*p2_1b) -(p1_1b*p3_1b))/(p0_1b-(p3_1b)^2)
    aelp_1b = p0_1b/((p0_1b*((u0_1b)^2))+((v0_1b)^2)+(2*p3_1b*u0_1b*v0_1b)-p4_1b)
    belp_1b = aelp_1b/p0_1b
290 celp_1b = p3_1b*belp_1b

    u0_1 = (u0_1a+u0_1b)/2
    v0_1 = (v0_1a+v0_1b)/2
    aelp_1 = (aelp_1a+aelp_1b)/2
295 belp_1 = (belp_1a+belp_1b)/2
    celp_1 = (celp_1a+celp_1b)/2
```

```
      p0_2a = oplossing2a(0)
      p1_2a = oplossing2a(1)
300   p2_2a = oplossing2a(2)
      p3_2a = oplossing2a(3)
      p4_2a = oplossing2a(4)

      u0_2a = (p1_2a-(p2_2a*p3_2a))/(p0_2a-((p3_2a)^2))
305   v0_2a= ((p0_2a*p2_2a) - (p1_2a*p3_2a))/(p0_2a-(p3_2a)^2)
      aelp_2a = p0_2a/((p0_2a*((u0_2a)^2))+((v0_2a)^2)+(2*p3_2a*u0_2a*v0_2a)-p4_2a)
      belp_2a = aelp_2a/p0_2a
      celp_2a = p3_2a*belp_2a

310   p0_2b = oplossing2b(0)
      p1_2b = oplossing2b(1)
      p2_2b = oplossing2b(2)
      p3_2b = oplossing2b(3)
      p4_2b = oplossing2b(4)
315
      u0_2b = (p1_2b-(p2_2b*p3_2b))/(p0_2b-((p3_2b)^2))
      v0_2b= ((p0_2b*p2_2b) - (p1_2b*p3_2b))/(p0_2b-(p3_2b)^2)
      aelp_2b = p0_2b/((p0_2b*((u0_2b)^2))+((v0_2b)^2)+(2*p3_2b*u0_2b*v0_2b)-p4_2b)
      belp_2b = aelp_2b/p0_2b
320   celp_2b = p3_2b*belp_2b

      u0_2 = (u0_2a+u0_2b)/2
      v0_2 = (v0_2a+v0_2b)/2
      aelp_2 = (aelp_2a+aelp_2b)/2
325   belp_2 = (belp_2a+belp_2b)/2
      celp_2 = (celp_2a+celp_2b)/2


      ;print, 'Ellips parameters 1a'
330   ;print,'Center x:', u0_1a
      ;print,'Center y:', v0_1a
      ;print,'a1:', aelp_1a
      ;print,'b1:', belp_1a
      ;print,'c1:', celp_1a
335
      ;print, 'Ellips parameters 1b'
      ;print,'Center x:', u0_1b
      ;print,'Center y:', v0_1b
      ;print,'a1:', aelp_1b
340   ;print,'b1:', belp_1b
      ;print,'c1:', celp_1b

      print, 'Ellips parameters 1'
      print,'Center x:', u0_1
345   print,'Center y:', v0_1
      print,'a1:', aelp_1
      print,'b1:', belp_1
      print,'c1:', celp_1

350   ;print, 'Ellips parameters 2a'
      ;print,'Center x:', u0_2a
      ;print,'Center y:', v0_2a
      ;print,'a2:', aelp_2a
      ;print,'b2:', belp_2a
355   ;print,'c2:', celp_2a

      ;print, 'Ellips parameters 2b'
      ;print,'Center x:', u0_2b
      ;print,'Center y:', v0_2b
360   ;print,'a2:', aelp_2b
      ;print,'b2:', belp_2b
      ;print,'c2:', celp_2b

      print, 'Ellips parameters 2'
365   print,'Center x:', u0_2
      print,'Center y:', v0_2
      print,'a2:', aelp_2
      print,'b2:', belp_2
      print,'c2:', celp_2
370
```

```
;_____________________________________________________________________

;                        Berekening van D/ZIS

;_____________________________________________________________________

m_0= (v0_2 - v0_1)*sqrt(belp_2 - ((celp_2)^2/aelp_2))

m_1 = sqrt(belp_2 - ((celp_2)^2/aelp_2))/sqrt(belp_1 - ((celp_1)^2/aelp_1))

n_0 = (1 - m_0^2 - m_1^2)/(2*m_0*m_1)

n_1 = (aelp_2 - (aelp_1*(m_1^2)))/(2*m_0*m_1)

ZISkwadraat1 = aelp_1 - (2*n_0*n_1)
ZISkwadraat2 = sqrt((aelp_1)^2 + (4 * (n_1)^2) - (4*n_0*n_1*aelp_1))
ZISkwadraat3 = 2*(n_1)^2
ZISkwadraat = (ZISkwadraat1 - ZISkwadraat2)/ZISkwadraat3

ZIS = sqrt(ZISkwadraat)

ZIScm = ZIS*0.04

print,'ZIS:' ,  ZIS, ZIScm

;_____________________________________________________________________

;                    Detector angle, phi

;_____________________________________________________________________


interpar1a = ZIS * aelp_1 * sqrt(aelp_1)
interpar1b = sqrt((aelp_1*belp_1)+((aelp_1)^2*belp_1*(ZIS^2)) - (celp_1)^2)
interpar1 = interpar1a/interpar1b

interpar2a = ZIS * aelp_2 * sqrt(aelp_2)
interpar2b = sqrt((aelp_2*belp_2)+((aelp_2)^2*belp_2*(ZIS^2)) - (celp_2)^2)
interpar2 = interpar2a/interpar2b

sinphi = ((-1*celp_1*interpar1)/ (2*aelp_1)) - ((celp_2*interpar2)/ (2*aelp_2))

phideg = asin(sinphi) * !radeg
phirad = asin(sinphi)

print,'Phi:', phideg   ,  phirad

;_____________________________________________________________________

;           Bepaal waar lyne mekaar kruis - Piercing point

;_____________________________________________________________________

m1 = 0.0
m2 = 0.0

m1 = (gembx[18] - gembx[0])/ (gemax[18] - gemax[0])          ; gradient van lyn 1
c1 = gembx[0] - (m1*gemax[0])                              ; y afsnit van lyn 1

m2 = (gembx[12] - gembx[6]) / (gemax[12] - gemax[6])         ; gradient van lyn 2
c2 = gembx[6] - (m2*gemax[6])                              ; y afsnit van lyn 2

kruisx = (c2-c1)/(m1-m2)

kruisy = (m1*kruisx) + c1



m1a = 0.0
m2a = 0.0

m1a = (gembx[19] - gembx[1])/ (gemax[19] - gemax[1])          ; gradient van lyn 1
c1a = gembx[1] - (m1a*gemax[1])                              ; y afsnit van lyn 1
```

```
445
      m2a = (gembx[23] - gembx[5])/ (gemax[23] - gemax[5])          ; gradient van lyn 2
      c2a = gembx[23] - (m2a*gemax[23])                           ; y afsnit van lyn 2

      kruisxa = (c2a-c1a)/(m1a-m2a)
450

      kruisya = (m1a*kruisxa) + c1a


455   m1b = 0.0
      m2b = 0.0

      m1b = (gembx[20] - gembx[2])/ (gemax[20] - gemax[2])           ; gradient van lyn 1
      c1b = gembx[20] - (m1b*gemax[20])                           ; y afsnit van lyn 1
460
      m2b = (gembx[22] - gembx[4])/ (gemax[22] - gemax[4])          ; gradient van lyn 2
      c2b = gembx[22] - (m2b*gemax[22])                         ; y afsnit van lyn 2

      kruisxb = (c2b-c1b)/(m1b-m2b)
465
      kruisyb = (m1b*kruisxb) + c1b

      m1c = 0.0
      m2c = 0.0
470
      m1c = (gembx[17] - gembx[11])/ (gemax[17] - gemax[11])           ; gradient van lyn 1
      c1c = gembx[17] - (m1c*gemax[17])                           ; y afsnit van lyn 1

      m2c = (gembx[13] - gembx[7])/ (gemax[13] - gemax[7])          ; gradient van lyn 2
475   c2c = gembx[13] - (m2c*gemax[13])                           ; y afsnit van lyn 2

      kruisxc = (c2c-c1c)/(m1c-m2c)

      kruisyc = (m1c*kruisxc) + c1c
480

      m1d = 0.0
      m2d = 0.0

485   m1d = (gembx[16] - gembx[10])/ (gemax[16] - gemax[10])          ; gradient van lyn 1
      c1d = gembx[16] - (m1d*gemax[16])                           ; y afsnit van lyn 1

      m2d = (gembx[14] - gembx[8])/ (gemax[14] - gemax[8])        ; gradient van lyn 2
      c2d = gembx[14] - (m2d*gemax[14])                           ; y afsnit van lyn 2
490
      kruisxd = (c2d-c1d)/(m1d-m2d)

      kruisyd = (m1d*kruisxd) + c1d

495
      piercx = [kruisx, kruisxa, kruisxb, kruisxc, kruisxd]
      piercy = [kruisy, kruisya, kruisyb, kruisyc, kruisyd]

      print, piercx
500   print, piercy

      piercxkoordinaat = mean(piercx)
      piercykoordinaat = mean(piercy)

505   print,'Piercing Point:'
      print, 'X koordinaat:', piercxkoordinaat
      print, 'Y koordinaat:', piercykoordinaat


510
      ;_____________________________________________________________

      ;              Calculation of detector angle, n

515   ;_____________________________________________________________

      ; Determination of converging point from lines L1 and L2
```

```
L1UP = sqrt((belp_1/((aelp_1*belp_1)-(celp_1^2))))
L1UN = -1*sqrt((belp_1/((aelp_1*belp_1)-(celp_1^2))))
L1V1 = -1*(celp_1/belp_1)*L1UP
L1V2 = -1*(celp_1/belp_1)*L1UN

; Koordinate vir lyn L1

L1xkoord1 = u0_1 + L1UP
L1ykoord1 = v0_1 + L1V2

L1xkoord2 = u0_1 + L1UN
L1ykoord2 = v0_1 + L1V1


L2UP = sqrt((belp_2/((aelp_2*belp_2)-(celp_2^2))))
L2UN = -1*sqrt((belp_2/((aelp_2*belp_2)-(celp_2^2))))
L2V1 =  -1*(celp_2/belp_2)*L2UP
L2V2 =  -1*(celp_2/belp_2)*L2UN

; Koordinate vir lyn L2

L2xkoord1 = u0_2 + L2UP
L2ykoord1 = v0_2 + L2V2

L2xkoord2 = u0_2 + L2UN
L2ykoord2 = v0_2 + L2V1

print, 'Lyne vir converging point'

print, L1xkoord1, L1ykoord1, L1xkoord2, L1ykoord2
print, L2xkoord1, L2ykoord1, L2xkoord2, L2ykoord2

;PLOTS, [L1xkoord1,L1xkoord2], [L1ykoord1, L1ykoord2], COLOR=12, /DEVICE
;PLOTS, [L2xkoord1, L2xkoord2], [L2ykoord1, L2ykoord2], COLOR=12, /DEVICE


p0a = 0.0
puntpa = 0.0

celp = piercykoordinaat - v0_1            ; Afstand tussen piercing point en middel van ellips 1,
ce2p = piercykoordinaat - v0_2            ; Afstand tussen piercing point en middel van ellips 2,

;print, celp
;print, ce2p

p0a = ((celp*sqrt(aelp_1/belp_1)) + (ce2p*sqrt(aelp_2/belp_2)))/ (sqrt(aelp_1/belp_1) + sqrt(aelp_

print, 'P0a:', p0a               ; Afstand vanaf piercing point na punt Pa, pixels

punt_pa = piercykoordinaat - p0a

print, 'Punt Pa:' , punt_pa

;PLOTS, [L1xkoord1,L1xkoord2], [punt_pa, punt_pa], COLOR=12, /DEVICE


;  Bepaling van hoek tussen L1 en L2 en alfa


hoekL1 = atan((L1ykoord1 - L1ykoord2)/(L1xkoord1 - L1xkoord2))

hoekL2 = atan((L2ykoord1 - L2ykoord2)/(L2xkoord1 - L2xkoord2))

detang = (((v0_1-punt_pa)*hoekL1) + ((punt_pa - v0_2)*hoekL2)) / (v0_1-v0_2)

detangrad = detang * !radeg

Print, ' Detector angle:'

print,  detang, detangrad
```

```
;_____________________________________________________________________________

;       Berekening van detector tilt en hoek, phi en theta

;_____________________________________________________________________________

PLOTS, [gemax[0],gemax[12]], [gembx[0],gembx[12]], COLOR=12, /DEVICE
PLOTS, [gemax[1],gemax[13]], [gembx[1],gembx[13]], COLOR=12, /DEVICE
PLOTS, [gemax[2],gemax[14]], [gembx[2],gembx[14]], COLOR=12, /DEVICE
PLOTS, [gemax[3],gemax[15]], [gembx[3],gembx[15]], COLOR=12, /DEVICE
PLOTS, [gemax[4],gemax[16]], [gembx[4],gembx[16]], COLOR=12, /DEVICE
PLOTS, [gemax[5],gemax[17]], [gembx[5],gembx[17]], COLOR=12, /DEVICE

PLOTS, [gemax[6],gemax[18]], [gembx[6],gembx[18]], COLOR=12, /DEVICE
PLOTS, [gemax[7],gemax[19]], [gembx[7],gembx[19]], COLOR=12, /DEVICE
PLOTS, [gemax[8],gemax[20]], [gembx[8],gembx[20]], COLOR=12, /DEVICE
PLOTS, [gemax[9],gemax[21]], [gembx[9],gembx[21]], COLOR=12, /DEVICE
PLOTS, [gemax[10],gemax[22]], [gembx[10],gembx[22]], COLOR=12, /DEVICE
PLOTS, [gemax[11],gemax[23]], [gembx[11],gembx[23]], COLOR=12, /DEVICE

stop
;_____________________________________________________________________________

;         Bepaal waar lyne mekaar sny, INDIEN WEL...:-)

;_____________________________________________________________________________
print, 'Converging point theta'

kruisarrx = fltarr(5)
kruisarry = fltarr(5)
tel = 0.0
xpunt = 0.0
ypunt = 0.0


;*****************************************************************************************

mconth1 = 0.00
cconth1 = 0.00

mconth2 = 0.00
cconth2 = 0.00

conthkruisx1 = 0.00
conthkruisy1 = 0.00

if gemax[0] eq gemax[12] then gemax[0] = gemax[0] + 0.0001
if gembx[0] eq gembx[12] then gembx[0] = gembx[0] + 0.0001
if gemax[6] eq gemax[18] then gemax[6] = gemax[6] + 0.0001
if gembx[6] eq gembx[18] then gembx[6] = gembx[6] + 0.0001

mconth1 = (gembx[0] - gembx[12])/ (gemax[0] - gemax[12])                    ; gradient
cconth1 = gembx[0] -  (mconth1*gemax[0])                                   ; y afsnit v

mconth2 = (gembx[6] - gembx[18])/ (gemax[6] - gemax[18])                    ; gradient
cconth2 = gembx[6] -  (mconth2*gemax[6])                                   ; y afsnit v

conthkruisx1 = (cconth2-cconth1)/(mconth1-mconth2)

conthkruisy1 = (mconth1*conthkruisx1) + cconth1

print, mconth1, cconth1, mconth2, cconth2

print, conthkruisx1, conthkruisy1

kruisarrx[0] = conthkruisx1
kruisarry[0] = conthkruisy1

teken1 = conthkruisx1/abs(conthkruisx1)
teken2 = conthkruisy1/abs(conthkruisy1)

xpunt = conthkruisx1
```

```
      ypunt = conthkruisy1

      tekena = teken1
670   tekenb = teken2

      tel = tel+1

      print, xpunt, ypunt ,tel
675
      ;*****************************************************************************************************

      mconth3 = 0.00
      cconth3 = 0.00
680
      mconth4 = 0.00
      cconth4 = 0.00

      conthkruisx2 = 0.00
685   conthkruisy2 = 0.00

      if gemax[10] eq gemax[22] then gemax[10] = gemax[10] + 0.0001
      if gembx[10] eq gembx[22] then gembx[10] = gembx[10] + 0.0001
      if gemax[8] eq gemax[20] then gemax[8] = gemax[8] + 0.0001
690   if gembx[8] eq gembx[20] then gembx[8] = gembx[8] + 0.0001

      mconth3 = (gembx[10] - gembx[22])/ (gemax[10] - gemax[22])              ; gradient van lyn 1
      cconth3 = gembx[10] -  (mconth3*gemax[10])

695   mconth4 = (gembx[8] - gembx[20])/ (gemax[8] - gemax[20])              ; gradient van lyn 1
      cconth4 = gembx[8] -  (mconth4*gemax[8])


      conthkruisx2 = (cconth4-cconth3)/(mconth3-mconth4)
700
      conthkruisy2 = (mconth3*conthkruisx2) + cconth3

      print, mconth3, cconth3, mconth4, cconth4

705   print, conthkruisx2, conthkruisy2

      kruisarrx[1] = conthkruisx2
      kruisarry[1] = conthkruisy2

710   teken3 = conthkruisx2/abs(conthkruisx2)
      teken4 = conthkruisy2/abs(conthkruisy2)

      if (teken3 eq tekena) and (teken4 eq tekenb) then xpunt = xpunt+conthkruisx2
      if (teken3 eq tekena) and (teken4 eq tekenb) then ypunt = ypunt+conthkruisy2
715
      if (teken3 eq tekena) and (teken4 eq tekenb) then tel = tel + 1

      print, xpunt, ypunt ,tel

720   ;*****************************************************************************************************

      mconth5 = 0.00
      cconth5 = 0.00

725   mconth6 = 0.00
      cconth6 = 0.00

      conthkruisx3 = 0.00
      conthkruisy3 = 0.00
730
      if gemax[2] eq gemax[14] then gemax[2] = gemax[2] + 0.0001
      if gembx[2] eq gembx[14] then gembx[2] = gembx[2] + 0.0001
      if gemax[4] eq gemax[16] then gemax[4] = gemax[4] + 0.0001
      if gembx[4] eq gembx[16] then gembx[4] = gembx[4] + 0.0001
735
      mconth5 = (gembx[2] - gembx[14])/ (gemax[2] - gemax[14])              ; gradient van lyn 1
      cconth5 = gembx[2] -  (mconth5*gemax[2])

      mconth6 = (gembx[4] - gembx[16])/ (gemax[4] - gemax[16])              ; gradient van lyn 1
740   cconth6 = gembx[4] -  (mconth6*gemax[4])
```

```
      conthkruisx3 = (cconth6-cconth5)/(mconth5-mconth6)

      conthkruisy3 = (mconth5*conthkruisx3) + cconth5
745
      print, mconth5, cconth5, mconth6, cconth6

      print, conthkruisx3, conthkruisy3

750   kruisarrx[2] = conthkruisx3
      kruisarry[2] = conthkruisy3

      teken5 = conthkruisx3/abs(conthkruisx3)
      teken6 = conthkruisy3/abs(conthkruisy3)
755
      if (teken5 eq tekena) and (teken6 eq tekenb) then xpunt = xpunt+conthkruisx3
      if (teken5 eq tekena) and (teken6 eq tekenb) then ypunt = ypunt+conthkruisy3

      if (teken5 eq tekena) and (teken6 eq tekenb) then tel = tel + 1
760
      print, xpunt, ypunt ,tel

      ;*************************************************************************************************

765   mconth7 = 0.00
      cconth7 = 0.00

      mconth8 = 0.00
      cconth8 = 0.00
770
      conthkruisx4 = 0.00
      conthkruisy4 = 0.00

      if gemax[1] eq gemax[13] then gemax[1] = gemax[1] + 0.0001
775   if gembx[1] eq gembx[13] then gembx[1] = gembx[1] + 0.0001
      if gemax[5] eq gemax[17] then gemax[5] = gemax[5] + 0.0001
      if gembx[5] eq gembx[17] then gembx[5] = gembx[5] + 0.0001

      mconth7 = (gembx[1] - gembx[13])/ (gemax[1] - gemax[13])              ; gradient van lyn 1
780   cconth7 = gembx[1] -  (mconth7*gemax[1])

      mconth8 = (gembx[5] - gembx[17])/ (gemax[5] - gemax[17])              ; gradient van lyn 1
      cconth8 = gembx[5] -  (mconth8*gemax[5])

785
      conthkruisx4 = (cconth8-cconth7)/(mconth7-mconth8)

      conthkruisy4 = (mconth7*conthkruisx4) + cconth7

790   print, mconth7, cconth7, mconth8, cconth8

      print, conthkruisx4, conthkruisy4

      kruisarrx[3] = conthkruisx4
795   kruisarry[3] = conthkruisy4

      teken7 = conthkruisx4/abs(conthkruisx4)
      teken8 = conthkruisy4/abs(conthkruisy4)

800   if (teken7 eq tekena) and(teken8 eq tekenb) then xpunt = xpunt+conthkruisx4
      if (teken7 eq tekena) and(teken8 eq tekenb) then ypunt = ypunt+conthkruisy4

      if (teken7 eq tekena) and (teken8 eq tekenb) then tel = tel + 1

805   print, xpunt, ypunt ,tel
      ;*************************************************************************************************

      mconth9 = 0.00
      cconth9 = 0.00
810
      mconth10 = 0.00
      cconth10 = 0.00

      conthkruisx5 = 0.00
```

```
815   conthkruisy5 = 0.00

      if gemax[11] eq gemax[23] then gemax[11] = gemax[11] + 0.0001
      if gembx[11] eq gembx[23] then gembx[11] = gembx[11] + 0.0001
      if gemax[7] eq gemax[19] then gemax[7] = gemax[7] + 0.0001
820   if gembx[7] eq gembx[19] then gembx[7] = gembx[7] + 0.0001

      mconth9 = (gembx[11] - gembx[23])/ (gemax[11] - gemax[23])              ; gradient van lyn 1
      cconth9 = gembx[11] -  (mconth9*gemax[11])

825   mconth10 = (gembx[7] - gembx[19])/ (gemax[7] - gemax[19])              ; gradient van lyn 1
      cconth10 = gembx[7] -  (mconth10*gemax[7])


      conthkruisx5 = (cconth10-cconth9)/(mconth9-mconth10)
830
      conthkruisy5 = (mconth9*conthkruisx5) + cconth9

      print, mconth9, cconth9, mconth10, cconth10

835   print, conthkruisx5, conthkruisy5

      kruisarrx[4] = conthkruisx5
      kruisarry[4] = conthkruisy5

840   teken9 = conthkruisx5/abs(conthkruisx5)
      teken10 = conthkruisy5/abs(conthkruisy5)

      if (teken9 eq tekena) and (teken10 eq tekenb) then xpunt = xpunt+conthkruisx5
      if (teken9 eq tekena) and (teken10 eq tekenb) then ypunt = ypunt+conthkruisy5
845
      if (teken9 eq tekena) and (teken10 eq tekenb) then tel = tel + 1

      print, xpunt, ypunt ,tel

850   ;*************************************************************************************************

      print, 'Array'

      print, kruisarrx, kruisarry
855
      print, xpunt, ypunt ,tel

      print, xpunt/tel, ypunt/tel

860   ;print , xpunt, ypunt, tel

      conthkruisx = xpunt/tel
      conthkruisy = ypunt/tel

865   ;conthkruisx = mean(kruisarrx)
      ;conthkruisy = mean(kruisarry)

      print, 'converging point theta', conthkruisx, conthkruisy

870
      thetafinaal = asin((conthkruisx/conthkruisy)/tan(phirad))

      print, 'theta finaal', thetafinaal, thetafinaal*!radeg
      print, 'phi1',phideg
875

      ZISgrafiek = 0.00
      intergrafiek1 = 0.00
      intergrafiek2 = 0.00
880   sinphigrafiek1 = 0.00
      sinphigrafiek2 = 0.00
      countgraf = 0.0
      verskilphigrafiek1 = 0.0
      verskilgrafiek = 10000000.00
885
      plotpg1 = fltarr(1499)
      plotpg2 = fltarr(1499)
      xas = fltarr(1499)
```

```
      countplot = 0
890
      for gg = 0.001,0.78,0.001 do begin


      phigrafiek1 = atan((conthkruisx/conthkruisy)/sin(gg))          ; tan()sin()
895
      ;thetagrafiek = asin((conthkruisx/conthkruisy)/tan(phigrafiek1))

      xas(countplot) = gg

900   plotpg1(countplot) = phigrafiek1


      ZISgrafiek = (sin(gg)*cos(gg))*(abs(conthkruisy) + p0a)

905   intergrafiek1a = ZISgrafiek*aelp_1*sqrt(aelp_1)
      intergrafiek1b = sqrt((aelp_1*belp_1)+((aelp_1)^2*(belp_1)*(ZISgrafiek)^2)-(celp_1)^2)
      intergrafiek1 = intergrafiek1a/intergrafiek1b

      intergrafiek2a = ZISgrafiek*aelp_2*sqrt(aelp_2)
910   intergrafiek2b = sqrt((aelp_2*belp_2)+((aelp_2)^2*(belp_2)*(ZISgrafiek)^2)-(celp_2)^2)
      intergrafiek2 = intergrafiek2a/intergrafiek2b

      sinphigrafiek1 = (-1*(celp_1)* intergrafiek1)/(2*aelp_1)
      sinphigrafiek2 = (celp_2*intergrafiek2) / (2*aelp_2)
915
      sinphigrafiek = sinphigrafiek1-sinphigrafiek2

      phigrafiek2 = asin(sinphigrafiek)                              ; Ellips model

920   plotpg2(countplot) = phigrafiek2


      verskilphigrafiek1 = abs(phigrafiek1-phigrafiek2)

925
      if verskilphigrafiek1 le verskilgrafiek then begin

      verskilgrafiek = verskilphigrafiek1

930   iindex = gg
      jindex = phigrafiek2


      endif
935
      countplot = countplot+1

      endfor

940   ;iindex = 0.00001745329252

      ;window, 1
      ;plot, xas,plotpg1, yrange = [-1.5,0.1]

945   ;window, 2
      ;plot, xas,plotpg2, yrange = [-1.5,0.1],color=255

      ;print, iindex

950


      thetagrad = iindex * !radeg

      print, thetagrad
955
      print, 'Theta radiale:' ,iindex
      print, 'Theta grade:' ,thetagrad

      finalephi = jindex
960
      phigrad = finalephi * !radeg
```

```
      print, 'Phi in radiale:', finalephi
      print, 'Phi in grade:', phigrad
965
      print, 'Ander phi', phirad, phideg

      stop

970   ;_____________________________________________________________________________

                          ; Determination of source position (virtual)

      ;_____________________________________________________________________________
975

      print, "Source position in virtual detector coordinate system:"

      ;iindex = 0.001
980
      ;Poa = Yis/cos(iindex)

      YIS = p0a*cos(iindex)

985   ZISregte = ((abs(conthkruisy))*sin(iindex))/(cos(finalephi))

      print, 'YIS:' ,YIS*0.04


990   L1afstand = gembx[9] - gembx[21]
      L2afstand = gembx[3] - gembx[15]

      rad = 9.75 / 0.04
      fanlengte = 16.2/ 0.04
995
      ;ZISregte = (2*rad*L1afstand*L2afstand)/(fanlengte*(L2afstand-L1afstand))


      print, 'ZIS:', ZISregte * 0.04
1000

      ; Real detector position


1005  rotmatr = [ [((cos(finalephi)*cos(detang))-(sin(iindex)*sin(finalephi)*sin(detang))),(cos(iindex)*
                  [((-cos(finalephi)*sin(detang))-(sin(iindex)*sin(finalephi)*cos(detang))),(cos(iindex)
                  [(cos(iindex)*sin(finalephi)),sin(iindex),(cos(iindex)*cos(finalephi))]]

      posvec = [0,YIS,ZISregte]
1010
      posreal = posvec##rotmatr

      xpossource = posreal[0]*0.04
      ypossource = posreal[1]*0.04
1015  zpossource = posreal[2]*0.04

      print, 'Position of source in real detector coordinate system:'

      print, 'X:', xpossource
1020  print, 'Y:', ypossource
      print, 'Z:', zpossource


      ;_____________________________________________________________________________
1025
      ;                              Detector position

      ;_____________________________________________________________________________

1030
      print, 'Detector position in virtual coordinate system:'

      ZID = ZISregte*(L1afstand-fanlengte)/L1afstand + rad
      ZIDcm = ZId*0.04
1035
      print, 'ZID:',  ZIDcm
```

```
      YID = YIS / ZISregte*ZID
1040
      YIDcm = YID * 0.04

      print, 'YID:' ,  YIDcm

1045  posvec2 = [0,YID,ZID]

      detposreal = posvec2##rotmatr

      print, "Detectror position in real detector space:"
1050
      print, 'X:', detposreal[0]*0.04
      print, 'Y:', detposreal[1]*0.04
      print, 'Z:', detposreal[2]*0.04

1055
      openw, lun, 'c:/RSI/IDL52/examples/aposingparametersm0.dat',/GET_LUN
      printf, lun, detangrad,thetagrad,phigrad,piercxkoordinaat, piercykoordinaat,xpossource, ypossource
      free_lun, lun

1060
      end
```